

NANOSCALE PATTERNING AND 3D ASSEMBLY FOR BIOMEDICAL APPLICATIONS

by

Teena James

A dissertation submitted to Johns Hopkins University in conformity with the requirements for the
degree of Doctor of Philosophy

Baltimore, Maryland

June, 2014

© 2014 Teena James
All Rights Reserved

Abstract

Due to the inherent planarity of nanoscale patterning, there is a pressing need to develop novel approaches for parallel and cost-effective three dimensional (3D) patterning and assembly at the nanoscale. The 3D devices formed by such approaches are important for chem-bio sensing, nanoelectronics and photonics, nanorobotics, and nanobiotechnology. The body of work presented in this thesis is focused on developing scalable and manufacturable processes to create curved and foldable 3D nanostructures with precise surface patterns, in a highly parallel and cost-efficient method. Specifically, two new approaches were developed which include the spontaneous curving of nanostructures using grain reflow and creation of nanopatterned channels, wells, and semiconducting conical nanopores using metal assisted plasma etching process.

During plasma etching of silicon with carbon tetrafluoride and oxygen, it was discovered that certain metals present during the process undergo characteristic changes. In the grain reflow process, tin grains were found to undergo grain coalescence, resulting in the spontaneous curving of structures with tight radii of curvature of the order of a few nanometers. Another approach presented in the thesis for the large scale parallel patterning in the nanoscale involves using catalytic etching of silicon, assisted by lithographically patterned noble metal geometries. Using this method, three dimensional structures such as nanopore arrays and gold (Au) nanoparticles (NPs) coated micro or nano wells and channels can be fabricated in silicon in a highly parallel fashion.

I also investigated the applications of the 3D nanostructures formed by the aforementioned processes. Conical nanopore arrays were used for voltage gated

biomolecular sensing and separations. Ionic transport through these pores was investigated and it was found that the rectification ratios could be enhanced by a factor of 100 by voltage gating on the semiconducting substrate alone, and that these pores could function as ionic switches with high on-off ratios. Further, multifunctional 3D nanostructures were also combined with bacteria to create a nanoscale bionic system that can be remotely controlled using a laser.

Overall, these results present important advancements in the development of nanoscale patterning and 3D assembly of curved and porous nanostructures with applications in biomedical sciences and microorganism robotics.

Advisor: David H. Gracias, Ph.D.

Readers: Sharon Gerecht, Ph.D., Rebecca Schulman, Ph.D., Nina Markovic, Ph.D.,
Denis Wirtz Ph.D., Margarita Herrera-Alonso, Ph.D., Ishan Barman, Ph.D., and
David H. Gracias, Ph.D.

Acknowledgements

My graduate life at Hopkins would not have been a success if it was not for the help and support of a number of generous people and I would like to take this opportunity to express my sincere gratitude to them.

First and foremost, I would like to thank my advisor Dr. David Gracias, for all the help he has given me over these years. I do not have words to adequately express my genuine gratitude and appreciation to him. He is a true teacher and an amazing mentor with a great passion towards his research and science. He challenged me to come up with novel ideas, taught me how to ask the right questions and when I got stuck he guided me in the right direction and encouraged to try new things with an open mind. His guidance, encouragement and support helped me to build up my confidence as a graduate researcher. There are several instances where his confidence in me and his support of my scientific endeavors lead to the finding of new phenomenon and results in the lab, and it is from him that I understood how an open and inquisitive mind leads to research success. There are also numerous occasions where I learned small but important things from our casual small talks- from ideas developing from watching the squirrels work in his back yard, or how buds that curl up in small space opens when they bloom to simple suggestions like reading molecular biology of the cell as a leisure read-all helped me to understand how a true researcher looks at the nature, take inspirations from it and at the end take efforts to learn new things. His hard work and commitment has always been an inspiration for me. I would also like to thank Dr. Gracias for providing me the support to use lab facilities at Princeton and for the financial freedom he provided to test out new ideas. In addition, I would also like to thank him for making my graduate life a great

experience for me, he was supportive and provided valuable advice to me especially during rough times and also while I had my first child while in graduate school. As a good teacher, he guided me, and I'm utmost thankful for all the support, advice and help he has given me all throughout these years.

I would also like to express my sincere gratitude to Professor Barrie Royce, Professor Emeritus in MAE department at Princeton for all the valuable discussions and Professor Howard Stone of Princeton for the discussions and collaboration in the bacterial nanobionics project. I also would like to thank Dr. Michael McAlpine of MAE for collaborations. I also would like to thank those who served as academic and research mentors all throughout my graduate career. I would like to express my gratitude to Dr. Sharon Gerecht, Dr. Michael Bevan, and Dr. Joelle Frechette for my first year courses and their guidance, support and help with the preparation for general exam. I benefitted immensely from the course in tissue engineering taught by Dr. Gerecht. I also want express my sincere appreciation and gratitude to my GBO and thesis committee, Dr. Sharon Gerecht, Dr. Rebecca Schulman, Dr. Nina Markovic, Dr. Denis Wirtz and Dr. Ishan Barman for finding time to help me. In a special way, I would also like to thank Dr. Margarita Herrera-Alonso for also agreeing to be on the committee and her support and help over the years.

Next, I would like to thank the past and current members of the Gracias lab, for their help and support. I would like to especially thank Dr. Jeong-Hyun Cho, Dr. Rohan Fernades, Dr. Pawan Tyagi, Dr. Yevgeniy Kalinin, Dr. Jaehyun Park, Dr. Si-Young Park, Dr. Sachin Kadam, Dr. Joyce Berger, Dr. Evin Gultepe, Dr. Tim Leong, Dr. Christina Randall, Dr. Noy Bassik, Dr. Jatinder Randawa, Dr. Mustapha Jamal, Dr. Kate Lafflin,

Changkyu Yoon, Hye Rin Kwag, Qianru Jin, Pedro Anacleto, Tao Deng and all the undergraduate researchers over the years especially Jack Chan, John Coia and Harrison Schwartz for their help in the lab. I would also like to thank in a very special way, Shivendra Pandey my good friend inside and outside the lab for his company and “coffee breaks” and willingness to help always. Also, my thanks go to Bryan Benson who was an undergraduate student at Gracias lab when I joined and is now a graduate student at Princeton, and his wife Cheryl for their wonderful friendship and support.

I would also like to thank NIH and NSF for funding and PRISM MFNL and IAC staff at Princeton especially, Joe Palmer, Dr. Pat Watson, Dr. Mikhail Gaevski, Dr. Nan Yao and Jerry Poirier for all the help and assistance. Also, thanks very much to Caroline Qualls of CBE at JHU for all the help and assistance with administrative matters. My deepest gratitude also goes to Saint John’s soup kitchen, Newark, NJ and our friends and family for their constant prayers, generous support all throughout.

Finally, I would like to thank my husband Manu and our son John. It was really God’s gift to give me such a supportive, loving husband by my side throughout all these years. Manu’s prayers and his confidence in me were the driving force that took me to pursue my dreams. When we started this journey from India, I never realized how God would make our dreams happen, but now at the end of it, I see how God’s hand worked in everything. As he finishes his dissertation at Princeton, I realize how lucky it was that we both were in closely related fields for our PhDs – he understood my frustrations over my failed experiments, he encouraged me to think deeply and plan experiments thoroughly, while I was at the point of giving up. A devoted husband and father, he undertook so much trouble for me and John and was a strong shoulder to lean on during

the most difficult and trying times. It was not until the birth of baby John, that I realized how truly blessed this life is- his cute smile and babbling voice makes life so joyful for us!

I would also like to thank my parents for their continued prayer and support and their faith in me. My father for showing the beauty of education, my mother for her continued prayers, my brother and sisters for being there for me. I also thank Manu's family for their prayers and support.

Finally, I thank Lord, for being my faithful friend, for guiding me every moment of my life, for listening to my complaints, for the love and blessings of my life, for answering my prayers and fulfilling my dreams.

Dedication

To my loving husband, my parents and my dear Jesus

Table of Contents

Abstract	ii
Acknowledgements	iv
Table of Contents	ix
List of Figures	xiii
List of Tables	xvi
1. Introduction	1
1.1 Nanoscale Patterning and 3D Assembly: Motivation and Challenges	1
1.2 Biological nanostructures: Self-assembled 3D structures with nanoscale patterns	2
1.3 Mimicking Nature: Artificial Self-assembly	5
1.3.1 Assembly of 3D nanostructures using biomolecular interactions	6
1.3.1.1 Nanoscale 3D assembly via Protein-Protein or Polypeptide Interactions	7
1.3.1.2 Nanoscale 3D assembly via Nucleic Acid hybridization	8
1.3.2 Nanoscale 3D assembly using Physical Forces	11
1.3.2.1 Templating methods	11
1.3.2.2 Van der Waals forces	12
1.3.2.3 Assembly by Curving and Bending Nanostructures	14
1.4 Our Approach for 3D Assembly of Nanostructured components	17
1.4.1 Approaches for Nanoscale Patterning	18
1.5 Top down Nanolithographic Techniques	19
1.5.1 Electron-beam lithography	20
1.5.2 Nanoimprint Lithography	10
1.6 Thesis Overview	21
2. Surface Patterned 3D nanostructures via self assembly	23
2.1 Patterning & Folding at the nanoscale	23
2.2 Tin Reflow Process	24
2.3 Formation of nanostructures by curling and bending	29
2.3.1 Fabrication details	31
2.3.2 Materials Selection Process	32
2.3.3 Role of Plasma Forming Chemistry	33
2.3.4 Understanding the role of geometry optimization in folding	34

2.3.5 Incorporation of Lithographic Patterns in Folded Structures	35
2.4 3D Assembly of patterned hinged nanopanels.....	43
2.4.1 Fabrication Process	44
2.5 Material Characterization Processes	47
2.5.1 EDX Elemental Color Mapping.....	47
2.5.2 EBSD Analysis of folded structures	48
2.5.3 HRTEM Analysis.....	51
2.6 Mass Production of 3D Nanostructures	53
2.6.1 Utilization of nanoimprint lithography to pattern geometries that self- assemble	53
2.6.2 Fabrication of nanostructures by Nanoimprinting Process	54
2.6.3 Examples of 3D folded nanostructures via nanoimprint lithography	56
2.7 Conclusions & Outlook.....	58
3. Nanopatterning of Silicon by Catalytic etching.....	59
3.1 Metal assisted Chemical Etching (MaCE) of Si	60
3.1.1 Fabrication of arrays of nanoholes using MaCE.....	61
3.2 Metal Assisted Plasma Etching (MaPE) of Si	64
3.2.1 Fabrication of Arrays of nanopatterned features in Si using MaPE	68
3.3 Creation of Silicon nanostructures with AuNP Coating using MaPE	69
3.3.1 Fabrication Process	70
3.3.2 Au NP size characterization.....	71
3.3.4 Antibody assembly within the microwells.....	71
3.4 Results and Discussion	72
3.4.1 Au NP coated Si microwells	72
3.4.2 Proposed mechanism	73
3.4.3 Influence of etch time	74
3.4.3 Influence of pattern geometry	76
3.4.5 Au NP coated microchannels.....	78
3.4.6 Antibody assembly within the microwells.....	79
3.5 Conclusions.....	80
4. Semiconducting Conical Nanopores by Metal Assisted Plasma Etching (MaPE)	82

4.1 Introduction.....	83
4.1.1 Dependence of Si etching on CF ₄ /O ₂ ratio	86
4.1.2 Effect of the power variation on conical nanopore geometry.....	87
4.2 Material Characterization.....	89
4.2.1 FTIR Analysis.....	89
4.2.2 X-ray photoelectron spectroscopy (XPS) Analysis	90
4.2.3 Contact Angle analysis	91
4.3 Electrical Characterization.....	92
4.3.1 Ion-current Rectification.....	92
4.3.2 Switching Characteristics.....	94
4.3.3 Kelvin Probe Measurements	97
4.4 Biomolecular Transport through pores	100
4.5 Details of experimental methods	101
4.5.1 Nanopore Membrane Fabrication Process.....	101
4.5.2 Ionic Rectification Studies.....	103
4.5.3 Biomolecular permeation studies.....	105
4.5.4 Theoretical etch model.....	106
4.5.5 Numerical Simulations of Protein Diffusion through Nanopores.....	110
4.6 Summary	112
5. Bacterial NanoHybrid devices	113
5.1 Introduction.....	113
5.2 Interfacing of Multifunctional Nanostructure with Motile Bacteria.....	115
5.2.1 Creation of Bacterial-Nanostructure Interfaces	118
5.3 Motion Analysis of Bacterial-Nano hybrids	119
5.4 Plasmonic control of bacterial motion	120
5.5 Materials & Methods	127
5.5.1 Fabrication of Multifunctional Nanostructures.....	127
5.5.1 Mass Fabrication of structures using nanoimprinting technique	128
5.5.3 Formation of nanobiohybrid devices	129
5.5.3.1 Bacterial Culture	129
5.5.3.2 Attachment of structures to bacteria	130

5.5.3.3 Motility tracking	131
5.6 Summary	132
6. Conclusions and Future Outlook	133
6.1 Summary of Main Conclusions	133
6.2 Outlook	136
6.2.1 Actuation of nanostructures	136
6.2.2 Application of semiconducting conical nanopores	137
6.2.2.1 Ionic Logic Gates	137
6.2.2.2 Energy harvesting	138
8. References	142
8. Curriculum vitae	158

List of Figures

Figure 1.1: Smart biological solutions in nature through nanopatterning.....	3
Figure 1.2: Schematic illustration of biological self-assembly seen in a phage particle.	4
Figure 1.3: Covalent attachment of nanogold to subunits through protein assembly.....	7
Figure 1.4: TEM image of end to end linkage of gold nanorods.....	8
Figure 1.5: DNA 3D structures.....	10
Figure 1.6: TEM images of mesostructures formed by templating.	12
Figure 1.7: SEM images of Ag nanocube assembly.	13
Figure 1.8: General methods to create a nanotube by heteroepitaxial method.....	15
Figure 1.9: Formation stages of monolayer tubes by heteroepitaxial method.....	16
Figure 1.10: Using stress generated from grain coalescence to drive 3D assembly.....	18
Figure 1.11: Thesis Overview.....	21
Figure 2.1: Fabrication of 3D nanostructures using hinged and hinge-less structures.....	24
Figure 2.2: SEM images showing tin-reflow process.....	25
Figure 2.3: SEM of nanolines with Sn alone.....	26
Figure 2.4: Schematic illustrating the mechanism of the folding process.....	27
Figure 2.5: Schematic and SEM of bilayer structure curving spontaneously.....	29
Figure 2.6: Schematic and SEM illustrating grain reflow to form nanostructures.....	30
Figure 2.7: Formation of long tubular structures.....	33
Figure 2.8: Formation of nanotubes.....	34
Figure 2.9: Engineering folds by engineering lithographic patterns.....	35
Figure 2.10: Nanomesh tube formation.....	36
Figure 2.11: Variation of radii of curvature with the cantilever geometry.....	37
Figure 2.12: Variation of grain size the cantilever geometry.....	39
Figure 2.13: Formations of Venus fly trap like fringed Nanoparticles.....	40
Figure 2.14: Nanoflower pattern.....	41
Figure 2.15: Nanogripper fabrication.....	41
Figure 2.16: Nano-slap bracelets and claws.....	42
Figure 2.17: Self-assembly process of hinged nanopannels.....	43
Figure 2.18: SEM Images of a 2D nets before plasma etching.....	44
Figure 2.19: SEM Image of hinged particle folding process.....	45

Figure 2.20: SEM images showing that the 2D nets assemble into box structure	46
Figure 2.21: EDX elemental color heat mapping of rolled up nanotubes.....	47
Figure 2.22: Monte-Carlo Simulation for penetration depth	49
Figure 2.23: Phase map of nanoimprint lines	50
Figure 2.24: Pole figure of Sn obtained from phase map	51
Figure 2.25: High resolution TEM image and diffraction pattern of structures	52
Figure 2.26: Nanoscale origami of nanoimprinted patterns	53
Figure 2.27: Commercial Nanoimprint Stamps.....	55
Figure 2.28: Lab fabricated nanoimprint stamps	56
Figure 2.29: 3D folded nanostructures patterned using nanoimprint lithography	57
Figure 3.1: Fabrication of nanohole arrays in Si via MaCE using Ag.....	62
Figure 3.2: MaCE performed for various duration of time.....	63
Figure 3.3: Effect of HF concentration in the MaCE etchant.	64
Figure 3.4: Plasma based dry etching process of Si.....	65
Figure 3.5: MaPE based creation of nanopores in silicon.....	68
Figure 3.6: Variation of Power in MaPE process	69
Figure 3.7: Spontaneous formation of Au NP coated Si microwells	73
Figure 3.8: SEM images of Si microwells formed at different etch times.....	75
Figure 3.9: Microwell size can be varied by using Au patterns of different sizes.....	76
Figure 3.10: SEM images of Si microwells formed by plasma etching of Au patterns with varying shapes.....	77
Figure 3.11: SEM image of a Au NP coated microchannel after etching	78
Figure 3.12: Sonication of the microchannel structure	79
Figure 3.13: Spatial assembly of antibodies within the Au NP decorated Si microwells.	80
Figure 4.1: Schematic illustration and SEM images of formation of conical nanopore ...	84
Figure 4.2: Versatility of conical nanopore formation in different Si substrates.	85
Figure 4.3: AFM analysis of conical nanopores	88
Figure 4.4: Model and experimental control of nanopore cone angle and size.	89
Figure 4.5: FTIR spectrum of plasma etched Si surface.....	90
Figure 4.6: XPS of the plasma etched Si surface.....	91
Figure 4.7: Contact angle of a pH 7 water drop on the plasma etched Si surface	92

Figure 4.8: Ion-current rectification observed in an individual conical nanopore.....	94
Figure 4.9: Voltage-gated switching of ionic current in conical nanopore.....	95
Figure 4.10: Kelvin Probe measurements	99
Figure 4.11: Voltage control of protein transport	101
Figure 4.12: Schematic diagram of nanopore fabrication in Si membranes.....	102
Figure 4.13: Plot of the cone half angle.	109
Figure 4.14: Geometry used in numerical simulation.....	111
Figure 5.1: Bacterial nanohybrid devices	117
Figure 5.2: Nanostructure fabrication and bacterial assembly.....	118
Figure 5.3: Enabling propulsion to nanostructures by motile bacteria	119
Figure 5.4: Characterization of plasmonic control.....	122
Figure 5.5: Remote control of bacterial motility via plasmonic nanoantenna	124
Figure 5.6: Formation of various configuration of nanogripper	128
Figure 6.1: Actuation of nanostructures with electron beam.....	137
Figure 6.2: Potential applications of Si conical nanopores in Ionic logic circuits.....	138
Figure 6.3: Schematic illustration of energy harvesting application of nanopore	139

List of Tables

Table 4.1: Variation of Si etching with varying O ₂ concentration and RF power	86
--	----

CHAPTER 1

Introduction

1.1 Nanoscale Patterning and 3D Assembly: Motivation and Challenges

Creating functional three dimensional (3D) nanostructures and devices with desired surface patterning could enable tremendous advancements across various disciplines in science and engineering including, nano-photonics and –electronics, sensing, nanorobotics and nanobiotechnology. In the famous lecture¹ by Richard Feynman, “There is plenty of room at the bottom” he illustrated his vision for the field of miniaturization by saying “Consider any machine – for example, an automobile – and ask about the problems of making an infinitesimal machine like it.”

Engineering in the macroscale is typically performed in three dimensions where the engineered structures are assembled from machined components consisting of a variety of materials precisely patterned in to the desired geometries. Therefore, considering closely the example of the building of an automobile, various materials are machined and shaped in to specific patterns and assembled in three dimensions to create the final functional device. However, in the contrast, the inherent 2D nature of the state of the art micro/nano fabrication techniques still prohibits the creation of 3D nanostructures or devices that are analogous to the infinitesimal machine as envisioned by Richard Feynman, consisting of heterogeneous composition and precise geometrical patterns. Even though, a number of processes have been developed over the past decades to grow nanoscale materials such as nanowires, nanotubes and nanoparticles, these methodologies

can only offer limited geometrical shapes and also very little ability to incorporate any surface patterning².

In addition, almost all of these methods operate in a serial manner and are thus often not economically feasible. For instance, top-down methods such as particle replication in nonwetting templates (PRINT)³ have been shown to have the ability to produce nanoparticles in a mass scale, however, they fail to offer any ability to incorporate surface patterning and are also limited to generate shapes with only single layers. On the other hand, advancements in the development of nanoscale electronic circuits, biomedical devices and photonic structures demand the ability to incorporate multi-layer patterning in nanoengineered structures. Therefore, there is a need to develop novel approaches for parallel and cost-effective three dimensional (3D) patterning and assembly at the nanoscale. Even more compelling, would be approaches that can utilize the power of already existing nanolithographic tools in generating 2D nanopatterned units and further enable assembly of 3D structures of desired geometries.

1.2 Biological nanostructures: Self-assembled 3D structures with nanoscale patterns

In nature, there is a wide variety of superior nanostructured materials that has provided inspiration for the creation of functional 3D nanostructured devices. A few examples of such functional nanostructures found in nature such as the superhydrophobic surface of lotus leaf, color changing surface of brittle star *Ophiocoma wendtii* and the compound eye of drosophila demonstrate how smart biological solutions are obtained from nanostructures in nature (Figure 1.1).

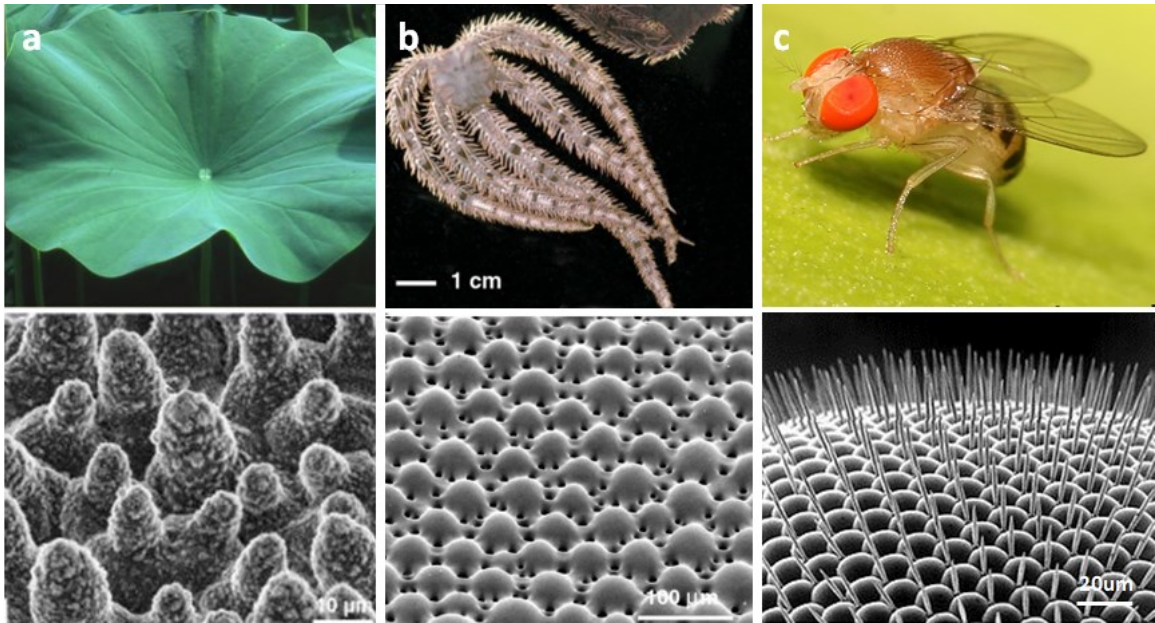


Figure 1.1 Smart biological solutions in nature through nanopatterning (a) Lotus leaf (b) Brittle star *Ophiocoma wendtii* and (c) *Drosophila*. Top panel shows photographic images of the same and bottom panel shows their corresponding nanostructured surface. (Images from Reference ^{4,5} Copyright 2004 Royal Society of Chemistry)

From the organization of proteins and nucleic acids to cells, tissues and organs, assembly process has shown to be nature's most preferred way for the building of 3D structures. A beautiful example of self-assembly in a biological system is a bacteriophage. A T4 phage consists of an icosahedral head (capsid), a cylindrical tail sheath, and six legs which are geometrical assemblies of DNA and a few proteins. These components are manufactured inside a bacterium and then self-assemble to form the final organism (Fig. 1.2). Once broken up in a blender, phages have been shown to have the

ability to reassemble in a test tube in a quasi-mechanical way without the use of any additional templates⁶.

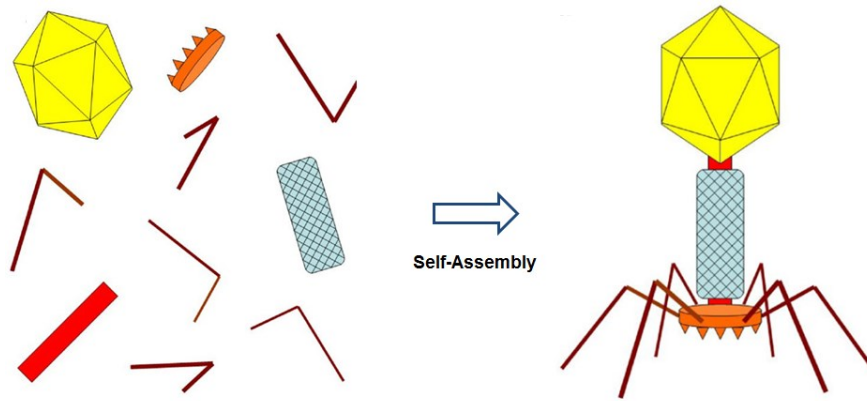


Figure 1.2: Schematic illustration of biological self-assembly seen in a phage particle. Image source Reference⁷ Copyright 2008 Elsevier

In fact, nature uses self-assembly/organization strategies to build all its biotic and abiotic constituent components ranging in size scale from nanoscale structures such as proteins and viruses to galaxies. Molecules are self-assembled from atoms, proteins are self-assembled from a set of 20 amino acids and biogenic tissue is resulted from a self-assembly or biological cells.

Engineering approaches for mimicking nature's multifunctional 3D hierarchical nanostructures thus demands for the development for novel approaches for enabling nanoscale patterns as well as strategies to bring forth their subsequent 3D assembly. Self-assembly could enable to mimic the design and creation of nanoscale structures with the complex, hierarchical arrangement found in biological systems. Therefore self-organization and assembly based strategies can offer a promising approach for economically efficient, mass- scale production of 3D nanostructured architectures for a variety of scientific and technological applications. This thesis presents two novel self-

organization and assembly approaches that we developed to achieve rapid formation of nanostructured patterns in Si and 3D assembly of nanopatterned components.

1.3 Mimicking Nature: Artificial Self-assembly

There have been attempts to mimic the biological self-assembly processes to build engineered structures for a very long time. The development of novel approaches that can mimic biological self-assembly to build complex 3D nanostructured devices from pre-programmed precursor components would be interesting both in terms of fundamental scientific inquiry and numerous potential technological applications. In general, the self-assembly processes found in nature can be either equilibrium or non-equilibrium processes. The abiotic structures such as stones, seashells that are resulted from equilibrium processes do not require additional energy expenditure to retain their structures. However, most of the living creatures such as biological organisms that are a result of non-equilibrium self-assembly processes requires a continuous expenditure of energy to maintain their assembly². Typically, self-assembly approaches bring forth association between components with pre-programmed interactions to form organized structures. These components can be atoms, molecules or engineered synthetic structures or desired geometries and patterns. The pre-programmed interactions can be engineered using a number of chemical reactions including the formation of covalent, ionic or hydrogen bonds and the onset of a pre-programmed catalytic reaction and physical interactions including electrostatic, magnetic, or mechanical stress and surface tension based forces. Through such interactions the engineered components can be self-reorganized in to the final 3D architectures.

The following sections review already existing strategies for mimicking the biological self-assembly to form nanoscale 3D structures. These approaches are mainly categorized into 1) Assembly of 3D nanostructures using biomolecular interactions. 2) Assembly 3D nanostructures using physical forces.

1.3.1 Assembly of 3D nanostructures using biomolecular interactions

Using natural biomolecules itself as agents to bring forth assembly of abiotic materials offers the closest approach in mimicking nature's self-assembly process in the formation of complex 3D nanostructures. The specific interactions exhibited by the naturally occurring biomolecules allows for the creation of hierarchical architectures of 3D nanoscale structures with impressive precision and complexity. In comparison to the use of physical forces as a means to accomplish nanoscale assembly the degree of complexity and specificity that can be accomplished by the molecular interactions can be higher. However, considering the numerous possible interactions between the biomolecular agents, such approaches in general can suffer from limited level of control that can be achieved.

In general these interactions are initiated *via* the functionalization of abiotic nanomaterial components with a ligand-receptor pair and thereby modifying their surface properties. The specific interactions between the ligand functionalized particles and the particles which are functionalized with the complementary receptors to the ligands enables self-assembly of the modified particles in to higher order hierarchical structures⁸. One major advantage of such an approach is that since most of the ligand-receptor pairs are capable of associating and dissociating at specific environmental conditions, this method can be made use of to create reversible assembly of 3D nanostructures. The most

widely used ligand-receptor pair for such applications involves protein and nucleic acid based assembly agents each of which are briefly reviewed in the sections below.

1.3.1.1 Nanoscale 3D assembly via Protein-Protein or Polypeptide Interactions

Protein-protein interactions are highly specific as a consequence of their unique conformational organizations. Further, due to the availability of multiple binding sites on a protein molecule the assembly of three dimensional architectures via such interactions is a natural outcome.

Such interactions solely between protein molecules have been demonstrated in past for the creation of various nanostructures such as nanotubes and nanoboxes^{9,10}. Surface functionalization of abiotic nanoparticles or nanomaterials with protein molecules have been also been explored to achieve complex 3D assembly¹¹ (Fig.1.3). The surface immobilization of protein is usually achieved via either thiol based chemistry in the case of Au surfaces and electrostatic interactions in the case of charged surfaces.

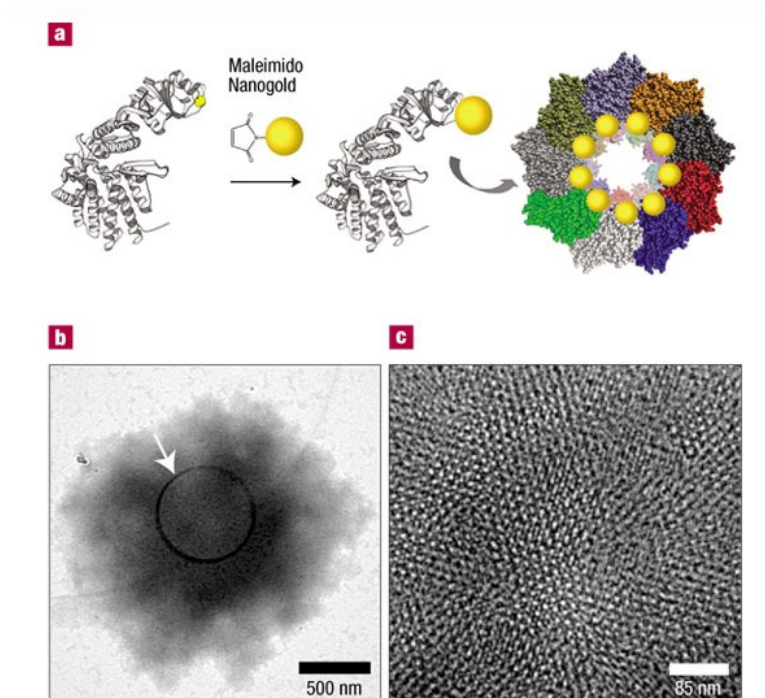


Figure 1.3 Covalent attachment of nanogold to subunits through protein assembly to form self-assembled gold arrays (Image Source Reference¹¹ Copyright 2002 Nature)

One of the most commonly used pair of protein molecules for self-assembly purpose is the biotin-streptavidin complex. The binding constant of the biotin-streptavidin complex can be as high as a covalent bond ($\sim K_a$ of 10^{15} M) and hence can facilitate the formation of stable 3D nanostructures when functionalized on the surface of nanoscale building blocks¹². Further, due to the presence of multiple binding sites, their interaction can also yield complex hierarchical structures with the structure being able to build up on a number of possible directions. Such interactions have been used to demonstrate the programmed assembly of various nanoscale abiotic functional units such as end to end linkage between Au nanorods¹³ (Fig. 1.4).

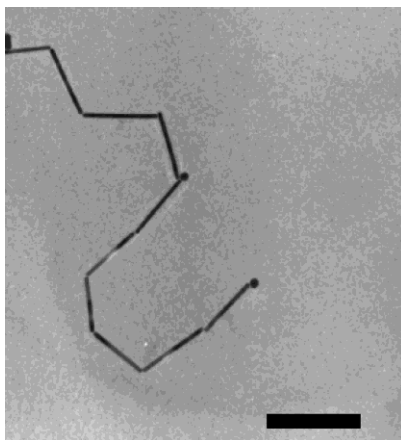


Figure 1.4 TEM image of end to end linkage of gold nanorods through protein Biotin–Streptavidin connectors. Scale bar at 500nm (Image Source Reference¹³ Copyright 2003 American Chemical Society)

1.3.1.2 Nanoscale 3D assembly via Nucleic Acid hybridization

DNA hybridization offers another route for achieving a 3D assembly of nanostructures in a programmable and precise manner¹⁴. In terms of achieving a rational design and

predictability of the final 3D architecture, nucleic acid interactions are advantageous, when compared to the protein-protein interactions due to the simplicity of its base pairing and well known crystallographic structures.

Similar to the assembly induced by protein-protein interactions, nucleic acid hybridizations have also been utilized to create either 3D nanostructures composed entirely of DNA or nanostructures with incorporation of inorganic nanomaterials where DNA was used to functionalize the surfaces. In 1991 Nadrian Seeman showed what believed to be for the first time the creation of a nanoscale cubical structure entirely composed of nucleic acids strands¹⁵. Triangular DNA structures such as trisoligonucleotides and tetrahedrons have been shown to possess high rigidity had thus received much scientific interests in the past¹⁶ (Fig.1.5). Successful creation of DNA tetrahedron geometries have been demonstrated with high yield, by the simple hybridization of four equal oligonucleotides with complimentary sites. Functionalities such as the encapsulation of protein molecules and assembling of higher order using the self-assembly of multiple tetrahedral geometries were also demonstrated using in the past^{17,18}.

Another concept of DNA origami was introduced by Paul Rothemund providing the capability to form easily programmable DNA nanostructures¹⁹ (Fig. 15). The technique involved the use of a long strand of nucleic acid to form a scaffold and a number of shorter nucleic acid “staples” to bind and fold the larger scaffold in to specific geometrical orientations. Using this approach, the creation of a DNA nanobox geometry with controllable lid was successfully demonstrated by assembly templates of six square patterns²⁰.

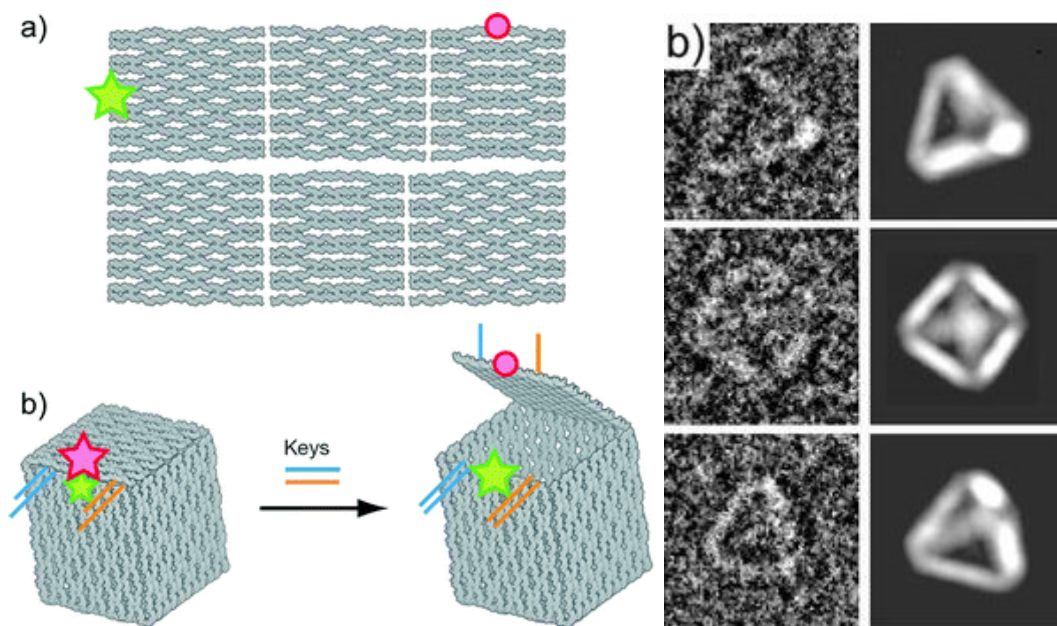


Figure 1.5 DNA 3D structures. Illustration of unlinked faces of the box and the controlled opening of the box lid. Reprinted with permission from Reference²⁰. Copyright 2009 Macmillan Publishers Ltd (Nature Publishing Group). Left panel shows raw cryo-EM images of individual particles and the corresponding projections of the DNA tetrahedron 3D structure reconstructed from the cryo-EM images. Image from Reference²¹ Copyright 2008 Macmillan Publishers Ltd (Nature Publishing Group)

Additionally, the immobilization of nucleic acid ligands on the surface of abiotic functional nanomaterials have been used to demonstrate hybridization induced assembly of higher order nanostructures. Such immobilizations have been successfully achieved *via* mainly Au-thiol chemistry or utilizing electrostatic interactions on to the surface of nanoparticle, nanorods and other inorganic functional nanoobjects to form “satellite” structures composed of a large central particle surrounded by multiples self-assembled smaller structures²². The versatility and simplicity of nucleic acid base pairing makes

DNA self-assembly one of the most promising approaches for the use of bimolecular linkages for achieving nanoscale 3D assembly.

A major disadvantage of the nanoscale 3D assembly relying on the biomolecular interactions is that the linkages established are not stable over a long period of time, making the nanostructures fall apart up on exposure to heat or other unfavorable environmental conditions. One promising alternative to overcome this problem is to utilize physical forces such as magnetic, electrostatic or Van der Waals interaction to enable the assembly.

1.3.2 Nanoscale 3D assembly using Physical Forces

The assembly of metallic or semiconducting nanoobjects in the 3D hierarchical geometries can result in multifunctional complex nanostructures with variety of functionalities including unique electronic, photonic, plasmonic and magnetic properties^{23,24} It has been known that 3D assembly builds upon the current 2D assembly methods. A few of such 2D assembly methods are surface interactions in Langmuir–Blodgett films at the air–liquid interface, evaporating thin liquid films over a solid support, 2D self-assembly of an array of nanoscale particles driven by capillary forces during evaporation,. As this assembly process is taken into 3D, these forces can again be taken into account to generate to 3D nanostructures.

1.3.2.1 Templating methods

Physical templates are one of the main ways used to drive self-assembly as it controls the arrangement and limits the number of particles within them. Various methods are used to create such templates such as electron –beam lithography, nanoimprint lithography, track

etching or anodization. An example of such 3D nanostructures formed by templating is shown in Figure 1.6 where mesostructures formed inside alumina nanochannels with differing confinement dimensions²⁵

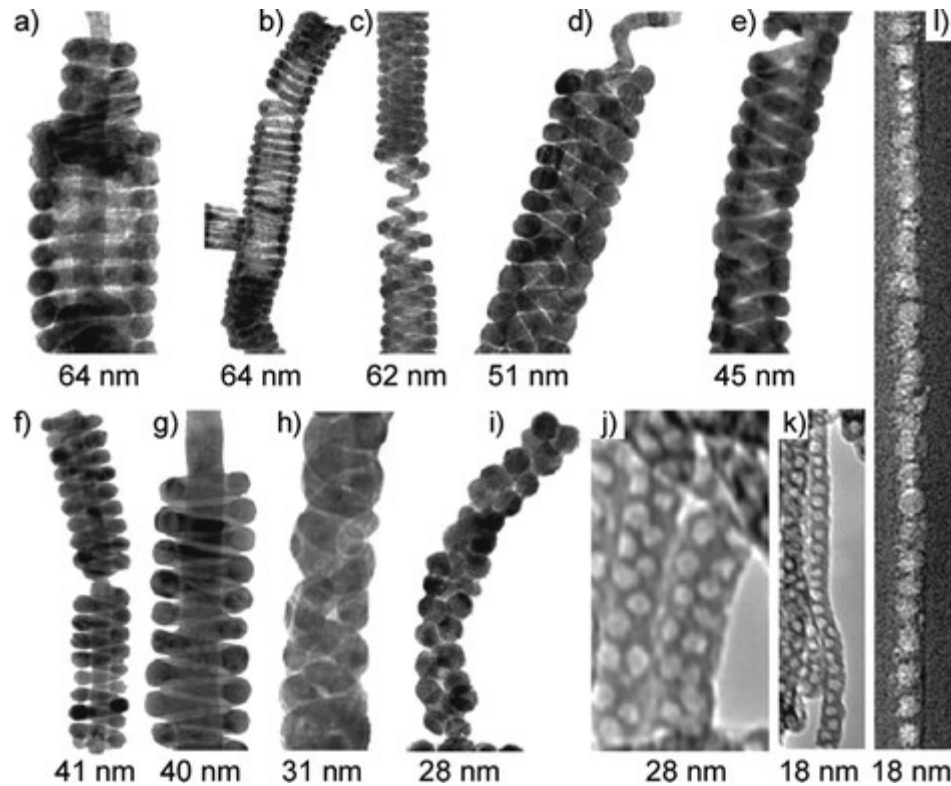


Figure 1.6 TEM images of mesostructures formed inside alumina nanochannels with differing confinement dimensions. The confining nanochannel diameter is indicated underneath each image. Reprinted with permission from Reference²⁵ Copyright 2007 Macmillan Publishers Ltd. (Nature Publishing Group)

1.3.2.2 Van der Waals forces

There are various examples of assemblies are formed though Van der Waals forces as it holds together particles in 3D assembly. An example is shown in Figure 1.7 where

selective hydrophobic functionalization of silver cubes on various faces resulted in the formation of 3D assemblies. However, a disadvantage of such assembly is that the force that holds them together is quite weak and can disrupt with processes such as sonication.

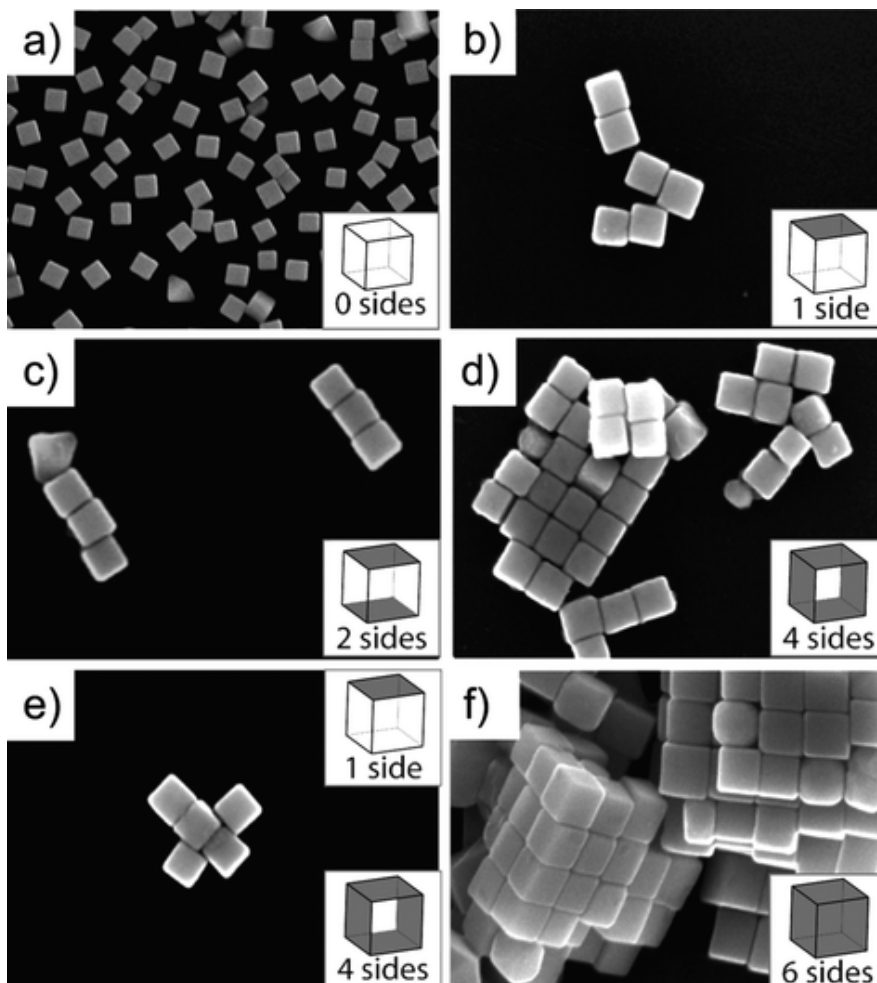


Figure 1.7 SEM images of Ag nanocubes and the assemblies. Unfunctionalized cubes deposited on Si from water are shown in (a) for reference. Nanocubes whose faces have been selectively functionalized with hydrophilic and hydrophobic thiolate SAMs and then allowed to assemble in water are shown in (b–f). The number of faces on each cube that were rendered hydrophobic is indicated in the bottom right corner of each panel, the remaining faces on the cube were rendered

hydrophilic. Reproduced with permission from Reference ²⁶ Copyright 2008 Wiley-VCH Verlag GmbH & Co. KGaA

In order to overcome the weak nature of these assemblies, permanent bonding can be introduced. In this case, the particles can be driven together by surface tension and then held in place with liquid drops that solidify²⁷ or through cross linking reactions²⁸.

1.3.2.3 Assembly by Curving and Bending Nanostructures

Another strategy to build 3D nanostructure is to leverage the existing 2D nanofabrication methods to create components that can rotate/bent in the 3rd dimension. Various forces such as thin film stresses, magnetism, pneumatics, swelling, and surface tension²⁹ can be used to achieve this rotation/bending phenomenon. We focus on the stress based techniques in this section.

In order to obtain a nanoscale radii of curvature, the stress required to curve is very high (~ Giga Pascal range). One example of generating such high stress is through strained heteroepitaxial films. As the films have different lattice constants, they are held at high strain, and they spontaneously curve upon release from the underlying substrate. An example of such curvature is shown in Figure 1.8 where an etchant-sensitive material is deposited on a substrate surface and selective etching of the sacrificial layer results in thin top layer is wrapped up (method 1) and in the second process, a bilayer of two different materials of two lattice constants (a_1 and a_2 for materials 1 and 2) such that $a_1 > a_2$. Once the bilayer is released by selective etching, each material tends to acquire its inherent lattice constant³⁰.

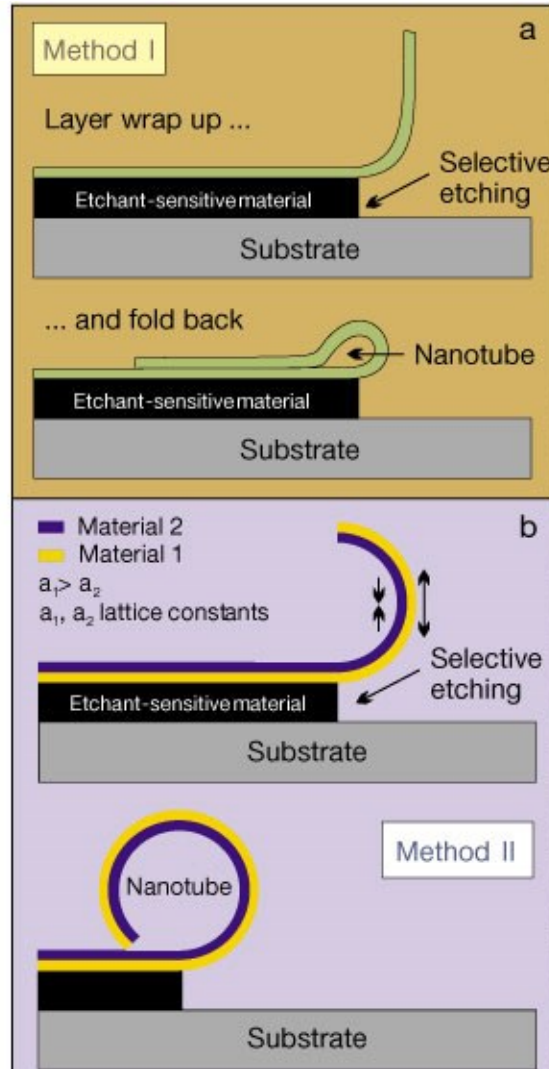


Figure 1.8 General methods to create a nanotube by heteroepitaxial method: Material 1 has a larger lattice constant than material 2, so $a_1 > a_2$. Once the bilayer is released by selective etching, each material tends to acquire its inherent lattice constant. Image from Reference ³⁰ Copyright 2001 Macmillan Publishers Ltd (Nature Publishing Group)

In an example of compound semiconductor bilayer, InAs/GaAs shown below³¹ the lattice parameters of InAs and GaAs are 6.06 and 5.65 Å giving a mismatch ($\Delta a/a$) of approximately 7.2%. Hence at the interfacial boundary of the two materials, the lattice parameter of InAs progressively decreases and that of GaAs increases away from the

interface (Fig 1.9). When the sacrificial layer AlAs is etched and the compressed layer (InAs) is stretched an elastic force F_1 is developed while on the stretched layer (GaAs) an elastic force F_2 is formed. As the directions of F_1 and F_2 are opposite, a non-zero moment (bending moment) of force M is created which is the actual bending moment that transforms 2D patterns into 3D curved structures².

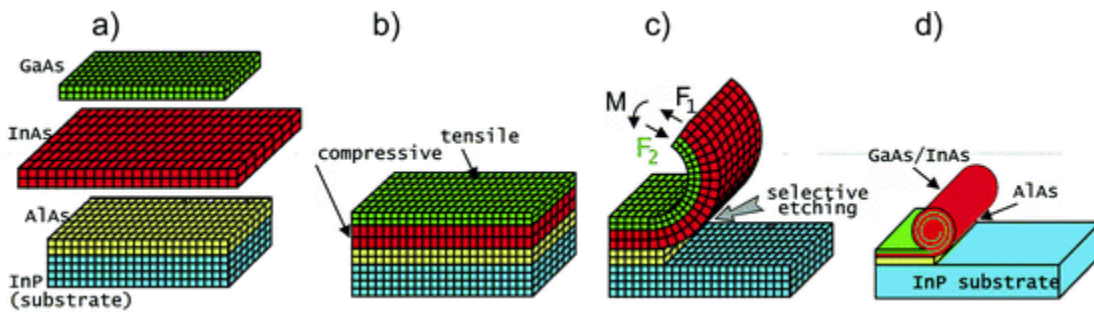


Figure 1.9 Initial formation stages of free-standing, several monolayer (ML) thick nanotubes (schematically): (a) free 2 ML thick InAs and GaAs layers with naturally mismatched lattice constants ($\Delta a/a = 7.2\%$); (b) matching of the layers at the interface between them in an InAs/GaAs bifilm MBE grown on an InP substrate; (c) bending of the GaAs/InAs bifilm after its partial detachment from the substrate during selective etching of the underlying AlAs sacrificial layer; (d) self-rolling of the GaAs/InAs bifilm in a tube scroll during further selective etching. Reproduced with permission from ^{31,32} Copyright 2004 Wiley-VCH Verlag GmbH & Co. KGaA

By varying the film thickness and/or the material composition, it has been demonstrated that the radii of curvature of these structures can be controlled³³. Further, it has also been found that the growth conditions of these films (such as temperature) also affects its material property and hence the radii of curvature³³. The diameters of the tube

were tuned based on the two parameters: film thickness and material type. In order to predict the shape of 3D structures, the bilayered nanotube diameter (D) can be modeled using continuum mechanics^{34,35}

$$D=d [3(1+m)^2+(1+m\cdot n)\cdot[m^2+(m\cdot n)^{-1}]]/3\varepsilon(1+m)^2 \quad (1.1)$$

$$d=d_1+d_2 \quad (1.2)$$

$$m=d_1/d_2 \quad (1.3)$$

$$n=Y_1/Y_2 \quad (1.4)$$

where ε is the in-plane biaxial strain between the two films, d_1 and d_2 are the thicknesses, and Y_1 and Y_2 are Young's moduli of the first and second layers, respectively. The results show that in order to minimize the diameters, the bilayer thickness d needs to be decreased³³. A disadvantage of the heteroepitaxial deposition method is that they require extremely high temperature for growth and generation of high stress which might affect the nanodevice properties. Although this can create 3D curved structures with extremely small diameters, the extreme temperatures that are required to generate high stresses could induce thermal shock on other devices on a substrate and alter device properties.

1.4 Our Approach for 3D Assembly of Nanostructured components

In our lab we have found that the above mentioned limitations can be overcome by using extrinsic stress developed in Sn grains by grain coalescence as shown below (Fig.1.10). This strategy can be made use of to engineer 3D nanostructures *via*: 1) Curving and bending of nanopatterned geometries (Fig.1.10a). 2) 3D assembly of

patterned hinged nanopanels (Fig.1.10b). This will be discussed in detail in the following chapters.

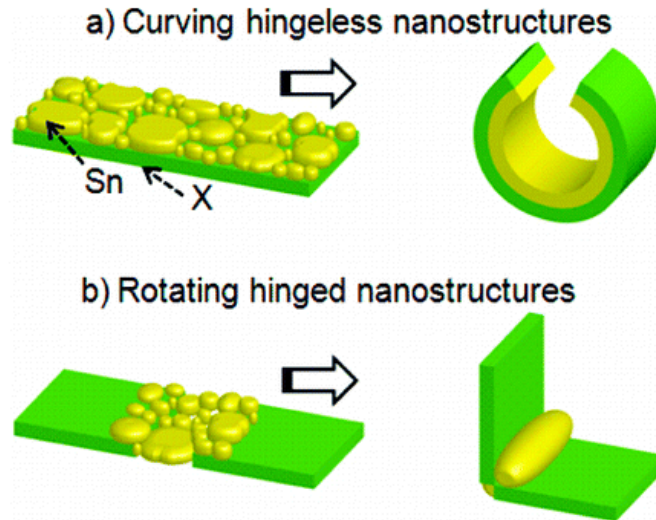


Figure 1.10 Using stress generated from grain coalescence to drive 3D assembly by a) curving b) hinged structures. Image from Reference ³⁶ Copyright 2010 American Chemical Society.

1.4.1 Approaches for Nanoscale Patterning

Cost efficient and parallel approaches for achieving rapid nanopatterns are in general, important for various nanoelectronics, photonics and biomedical applications. Further, abilities to create micro and nanoscale recessed structures with nanoscale patterns are highly important for attempts to mimic nature's multifunctional, complex patterned 3D nanostructures. For example, approaches for the spontaneous creation of nanoscale channels, wells and through pores of various geometries on semiconducting substrates of silicon can create numerous opportunities to develop bio-inspired nanophotonic and ion selective architectures.

Au and Si are two of the mostly commonly used materials for these applications due to the availability of the well-developed biomolecular interfacing chemistries and processing methods. Most of the currently available methods for the creation of nanoscale porous patterns in silicon involve the use of beams of high energy particles produced by an expensive ion beam machine as in the case of ion beam sculpting or a transmission electron microscope as in the case of TEM drilling. Approaches for spontaneous and parallel nanopatterning of silicon surface which can also leverage on the already existing top down lithographic techniques such as e-beam and nanoimprint lithography would thus be very interesting.

We developed a novel approach for large scale surface patterning of Si utilizing catalytic plasma etching of Si assisted by nanolithographically patterned noble metal geometries, dubbed “MaPE” process. The versatility of MaPE process enabled successful creation of three dimensional recessed nanostructures such as nanopore arrays and gold nanoparticle coated micro and nano well and channel geometries.

The main highlight of both these two new approaches that we developed for the creation of nanostructured patterns and achieving 3D nanoscale assembly is that they utilize and take advantage of the power of already existing and well-developed nanolithographic techniques such as e-beam and nanoimprint lithographies (a brief overview of these lithographic techniques is given below).

1.5 Top down Nanolithographic Techniques

Top down approaches for nanofabrication in general utilizes lithographic tools to pattern on nanoscale features on a substrate. Two of the major approaches for lithographic patterning are electron beam lithography (EBL) and nanoimprint based lithography.

1.5.1 Electron–beam lithography

In e-beam lithography a high energy electron beam is focused and scanned on the surface of an electro-sensitive polymer to create a latent pattern directly. The primary advantage of electron-beam lithography it can make patterns with sub-10 nm resolution. However a disadvantage of this process is that it is not suitable for high-volume manufacturing because of its limited throughput as it is a serial process. Here, a focused beam of electron beam of a few nanometers in spot size is scanned across the sample in a raster pattern the polymer resist is exposed in direct write fashion. The pattern generated in a CAD file is used to control a beam blanking system to control the writing. The EBL resists commonly used include poly (methyl methacrylate) (PMMA) based positive resists and SU-8 based negative resists. As the EBL generates pattern by writing in a serial manner, patterning of a large area of sample could result in a long processing time.

1.5.2 Nanoimprint Lithography

In contrast to the EBL process that is serial, nanoimprint lithography (NIL) offers the ability to pattern nanoscale features in a parallel fashion using a hard mold. In general, in NIL the topographic pattern from a hard mold (usually Si) is transferred to a thermoplastic polymer that is heated above its glass forming temperature via a pressure induced process. The Si mold is pressed in contact to the polymer and then viscous liquid flow of the polymer is brought forth by heating to allow it flow into the mold. Further solidification by cooling generates a replica of the mold pattern on the resist.

Both the EBL and NIL techniques are well developed to generate two dimensional (2D) patterns on a substrate at the nanoscale resolutions.

1.6 Thesis Overview

This thesis presents our studies on developing scalable and manufacturable processes to form 3D nanostructures with precise surface patterns, in a highly parallel and cost-efficient manner.

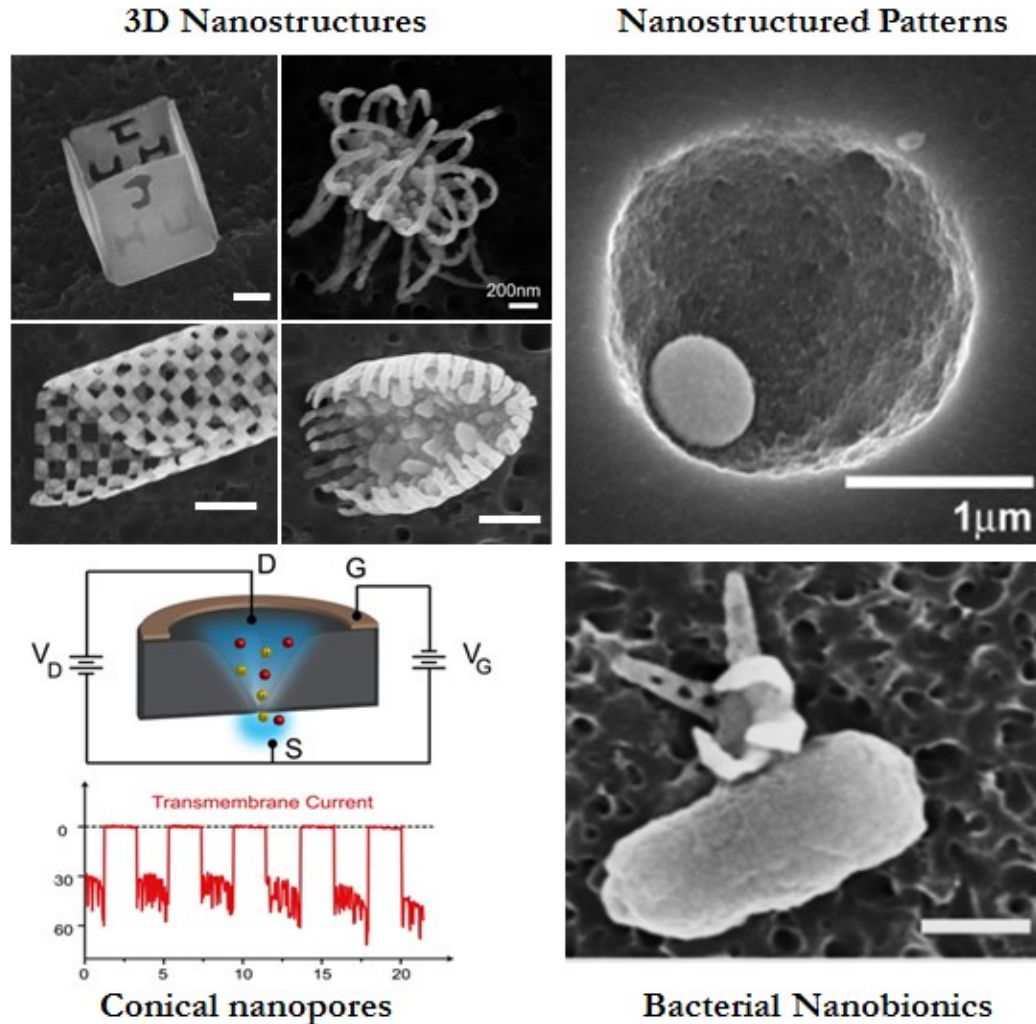


Figure 1.11 Thesis Overview (*Top left*) 3D nanostructures formed by grain coalescence: Chapter 2 (scale bar is 200nm). (*Top right*) Nanostructured Patterns via MaPE: Chapter 3. (*Bottom left*) Formation of conical nanopores and investigations of ionic transport: Chapter 4. (*Bottom right*) Bacterial Nanobionic Systems: Chapter 5.

Importantly, self-organization and self-assembly approaches were developed to transform these patterns into 3D structures such as nanoboxes, nanogrippers and conical nanopores. Specifically, two new approaches were developed which include the spontaneous curving and assembly of nanostructures using grain reflow and creation of nanopatterned channels, wells, and semiconducting conical nanopores using metal assisted plasma etching process (MaPE). The highlight of these approaches is that they leverage already existing nanolithographic techniques such as e-beam and nanoimprint lithographies, which are highly precise and well developed.

The next chapters of this thesis are thus organized as follows: Chapter 2 presents the approach that we developed for three dimensional curving and assembly of nanostructures by inducing grain coalescence in tin (Sn) thin films. Chapter 3 presents a novel strategy for large scale parallel patterning in the nanoscale utilizing catalytic etching of silicon, assisted by lithographically patterned noble metal geometries, a process called MaPE. Chapter 4 discusses the biomedical applications of the catalytic etching based Si nanopatterning approach featuring the creation of conical nanopore geometries in Si as a means to mimic the biological ion channels. Investigations on the ionic transport properties of conical nanopores under the influence voltage gating on the semiconducting substrate is also presented. Chapter 5 presents our work on the utilization multifunctional 3D nanodevices for development of bionic nanohybrids with motile bacteria. Our studies on remotely controlling bacterial motion to exclusive straight runs or tumbles *via* plasmonic control signals to the cell surface interfaced plasmonic nanoantennas are also presented. Finally, the thesis concludes with a summary of the research and discussion on interesting future directions.

CHAPTER 2

Surface Patterned 3D Nanostructures via Self-assembly[§]

2.1 Patterning & Folding at the nanoscale

Numerous strategies such as electron beam, imprint and probe-microscopy based lithography have been developed to pattern structures, materials and devices with nanoscale precision, but these techniques can be implemented only in an inherently two dimensional (2D) manner. Hence, despite the fact that we can easily engineer macroscale structures in 3D, human engineering on the nanoscale is limited. At the present time, nanostructures and nanoparticles such as rods, polyhedra, wires and tubes can be fabricated with only very limited surface patterning e.g. segmented nanowires or patchy particles.³⁷⁻³⁹ Hence, development of methods that enables 3D structures to be patterned in all three dimensions in a cost-effective and parallel manner is necessary.

Folding is a promising approach to build 3D objects at micro/nanoscale; as most of the processing techniques of micro/nano fabrication results in planar structures. Among the techniques that could be used for folding, utilizing surface forces for folding

[§] Portions of this chapter are reprinted with permission from (1) Cho, J. H., James, T., Gracias, D. H. Curving nanostructures using extrinsic stress. *Adv. Mater.* 22, 2320-2324 (2010). Copyright 2010 Wiley-VCH Verlag GmbH & Co. KGaA (2) Cho, J. H., T. James, D. H. Gracias Fabrication of 3D nanostructures with lithographically patterned surfaces by self-folding *SPIE*, Vol 7767, 776704 (2010) Copyright 2010 Society of Photo Optical Instrumentation Engineers. (3) James, T. *et al* Creation & mass production of Surface Patterned 3D Nanostructures via Grain Coalescence assisted Self-Assembly *in preparation*

structures is particularly appealing as the size scale decreases, since the surface forces dominate over bulk forces at small length scales. Control over surface forces at micro/nanoscale is challenging, however, using rational design rules, folding at small length scales can be guided to a good extent. Capillary origami is one such technique that has gained a lot of interest in the recent years, and it has been shown as a way of self-assembling objects^{40,41} as well as the folding of planar mm scale structures to form 3D objects^{42,43}. However, at the nanoscale, such process becomes more complicated as the radii of curvature for folding goes down to 20-100nm. The stress required for such folding process at nm length scale requires about 5 GPa, which cannot be provided by simple liquids. In this chapter, I describe approaches to curve and fold lithographically patterned structures based on stresses in thin films. Our concept involves patterning thin film multilayers using electron beam lithography; however any 2D patterning technique could also be utilized. These methods can broadly be classified into two: (a) assembly of hinged nanopanels (b) curving of 2D nanopatterns (Figure 2.1).

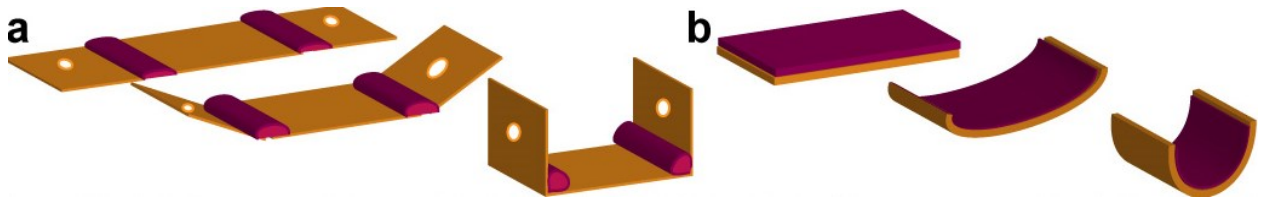


Figure 2.1: Fabrication of 3D nanostructures using hinged (bending) and hinge-less (curving) structures.

2.2 Tin Reflow Process

In our lab, we found that the extrinsic stress caused by tin metal during grain coalescence can be used for the formation of controlled stresses at relatively low temperature⁴⁴. Here,

by inducing grain coalescence within thin film multilayers we can cause spontaneous assembly of structures upon release from the substrate.^{44,45}

We found that Sn reflowed when exposed to CF₄/O₂ (Figure 2.2) with a 3.6 and 12 sccm flow rate of O₂ and CF₄, respectively, for 2 min. and we also found that the extent of grain coalescence increased with increasing plasma etching times. This heating induced grain coalescence is accompanied by an increase in stress in the film. From Figure 2.2 it can be seen that as grain coalescence was induced in Sn films, the edges curled up on release from the underlying Si substrate. This curving of Sn films can be rationalized by noting that a stress gradient develops in the coalescing thin film.

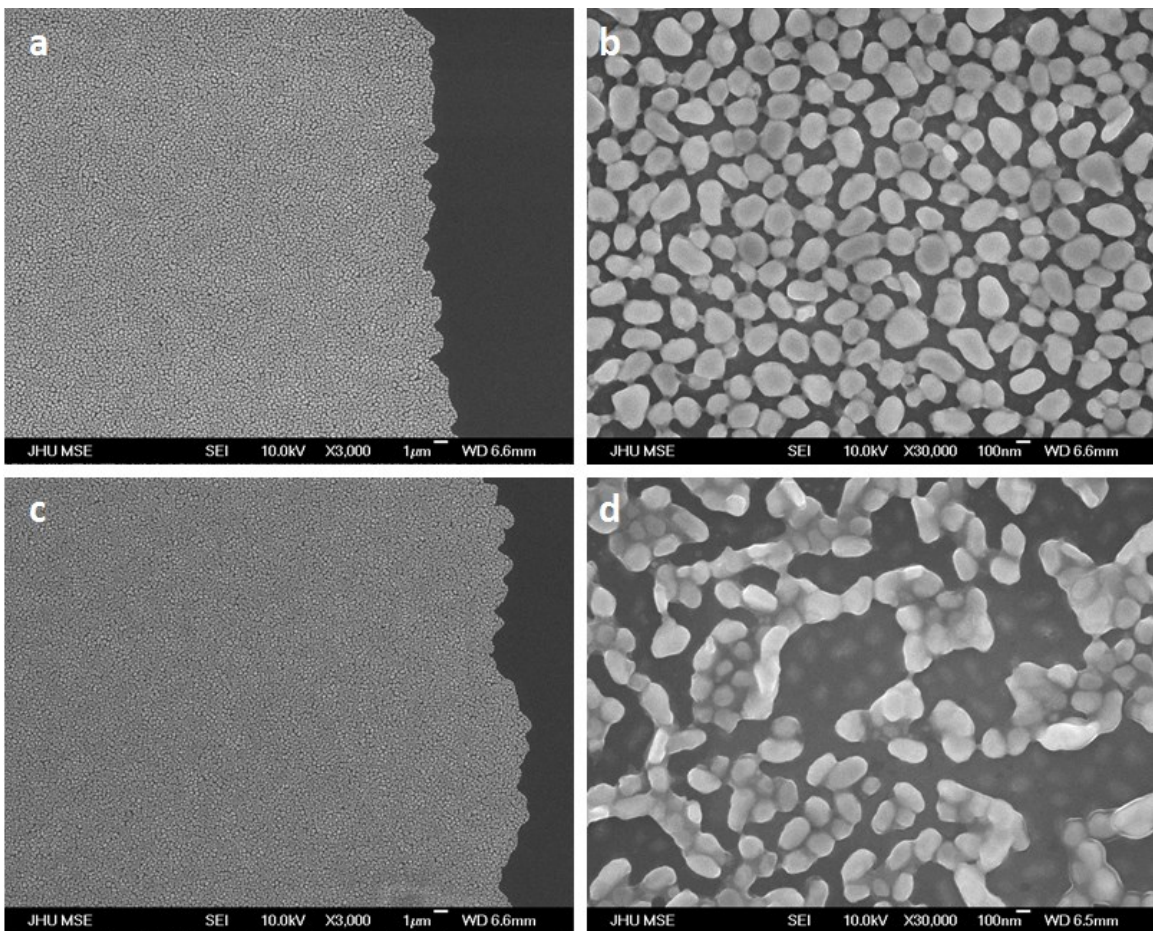


Figure 2.2: Scanning electron microscopy (SEM) images showing results of experiments investigating Sn reflow (a) A 50 nm thick Sn film evaporated on a silicon wafer prior to reflow, magnified image is shown in (b). (c) The Sn film after exposure to O₂/CF₄ plasma when reflow was observed; magnified image is shown in (d).

Since the deposited Sn film was discontinuous as can be seen from the SEM image, the curvature at the rolled-up edges was not uniform and was additionally difficult to control reproducibly. Moreover, it was challenging to pattern and create functional nanostructures with these discontinuous, single-layer Sn films (Figure 2.3)

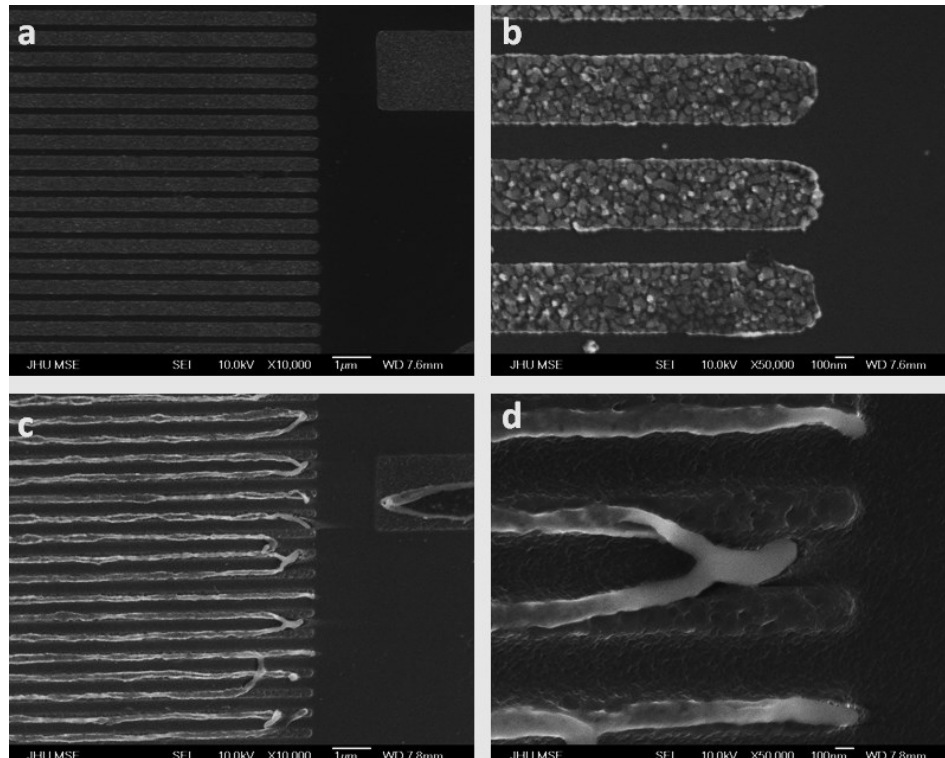


Figure 2.3: SEM of nanolines with Sn alone (a,b) SEM of the nanoimprinted line structure with deposited Sn before plasma etching. The tin can be seen to undergo grain reflow process after plasma etching (c,d).

Hence, in order to utilize this extrinsic stress to reproducibly to curve patterned nanostructures, we investigated the insertion of a continuous film (green layer in Figure 2.4), in between the Si substrate and Sn film. A schematic and SEM images showing our approach of generating curvature by inducing grain coalescence is shown in Fig. 2.4. The SEM image on the left panel shows Sn grains as deposited on a bare silicon substrate. After plasma etching of the underlying substrate, the Sn grains coalesce as a result of the heat generated during the exothermic etching process. The grain coalescence induces considerable stress within the Sn film. When deposited atop a Ni layer, this differential stress produced by Sn causes the Sn/Ni bilayer to curve with nanoscale radii of curvature. In the present case, the heat was generated during Si dry etching process with 12 sccm CF_4 and 3.6 sccm O_2 gas mixture for about 3 minutes. Under etching of the Si substrate in plasma causes the structure to curl up from the edges with tight radii. The grain coalescence occurring at the Sn surface will serve as a driving force for the folding of the structure.

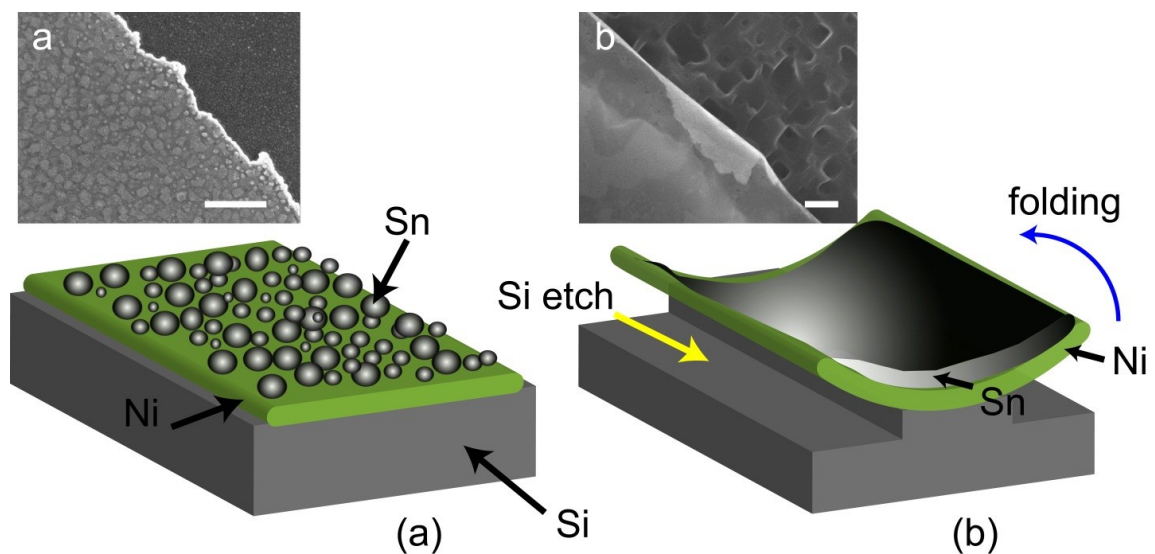


Figure 2.4: Schematic illustrating the mechanism of the folding process (a) SEM and schematic illustration of the structure before etching. The granular nature of the thin film of tin on top of the nickel is evident in the SEM and indicated schematically above the green nickel surface (b) SEM and schematic of the structure after plasma etching. The structure curls up at the edges as the silicon is under-etched in plasma. The tin can be seen to undergo grain coalescence which drives the bilayer structure to fold (Scale bars at 500 nm).

The highlight of this approach is that it leverages the strengths of already existing 2D patterning techniques while at the same time enabling the creation of 3D structures.⁴⁶ In addition, we have utilized nanoimprint lithography, to demonstrate the possibility of creating three dimensional curved nanostructures using nanoimprint lithography by taking the process further to fabricate them en masse and fold them into three dimensional structures. The application of such structures are many, and we envision the ability to create millions of precisely controlled curved nanostructures for application in drug delivery, plasmonics and other similar environments wherein 3D nanostructures could greatly enhance a given functionality. We demonstrate the application of nanoimprinting technology for the creation of such nanoscale three dimensional structures. Depending on the length scale of the nanopatterns, structures with varying degree of curvature can be fabricated. Radius of curvature ranging from nanometers to micrometers can be precisely tailored on nanostructures using this technique. Thus the simple approach of nanoimprinting followed by self-folding can be used to create millions of such 3D nanoparticles with engineered curvature.

The following sections demonstrate the use grain coalescence process to generate 3D nanostructures by 1) curving (hinge-less) method 2) folding (hinged) method and 3) mass production of 3D nanostructures by nanoimprint lithography.

2.3 Formation of nanostructures by curling and bending

It is well known that thin film multilayers with differential stress will curve when they are released from the substrate.⁴⁷⁻⁵⁰ Spontaneous curving of multilayers has been utilized previously in fabrication. In addition, the well-known wafer and cantilever bending methods used to measure thin film stresses are based on the spontaneous curving of multilayers with differential stresses. The main challenge is that the stress needed to achieve small nanoscale radii of curvature is very high and typically inaccessible through conventional thin film deposition methods. Hence, while it is relatively straightforward to get the panels to curve with microscale radii of curvature, it is extremely challenging to achieve nanoscale radii. The differential stress causes e-beam patterned Ni/Cu to bend, but the radii of curvature is relatively large of the order of microns as can be seen in Figure 2.5b.

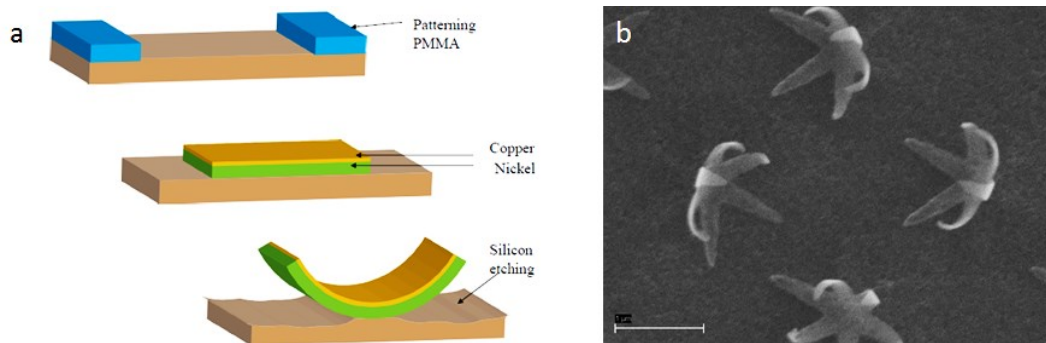


Figure 2.5: Schematic and SEM of bilayer structure curving spontaneously (a) Schematic illustrating the mechanism of the folding with Cu/ Ni bilayers and (b) The structure in the SEM image is composed of a Cr (adhesion) / Ni / Cu trilayer.

In the tin reflow process, we utilize grain coalescence to drive assembly and this approach can be used to create nanoscale folds and curvature. This method is straightforward in that the stress that results when grains of a metal coalesce is used to curve structures. It should be noted that as compared to intrinsic Cr stresses that are developed during deposition, grain coalescence is induced post-deposition, typically by heating during plasma etching of the underlying substrate. The origin of the high extrinsic stress observed within the Sn film that caused Ni/Sn bilayers to curl up with nanoscale radii of curvature is shown in Figure 2.6a .The induction of grain coalescence in Sn films is caused during plasma etching. When deposited atop a Ni film, the stress within the Sn thin film is large enough to cause the Sn/Ni bilayer to curl up. SEM image of Ni/Sn bilayer curving into a nanoscale tubular structure with 20nm radii of curvature is shown Fig 2.6c

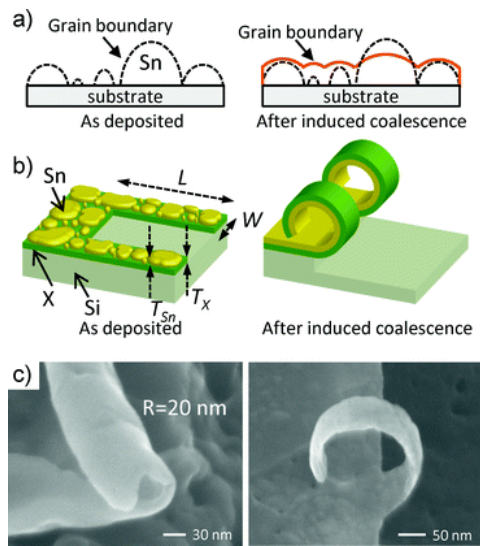


Figure 2.6: Conceptual sketches and scanning electron microscopy (SEM) images showing the utilization of grain reflow to form nanostructures. Reproduced with permission from Reference ⁴⁴Copyright 2010 Wiley-VCH Verlag GmbH & Co. KGaA

2.3.1 Fabrication details

All structures were fabricated on 3 inch diameter, n type <100> silicon wafer substrates. Patterning was done with electron (e)-beam lithography using a 100 nm thick polymethylmethacrylate (PMMA, MW 950K 2A) resist that was spin coated. An e-beam controlled by a RAITH system (v 4.0) was used to pattern the resist and was then developed using a methyl isobutyl ketone (MIBK) developer (1 to 3 parts IPA) for 35 seconds. Then, the desired thickness of the metal films was deposited using either thermal evaporation (Ni, Ag, Cu, Cr, Sn) or by dc magnetron sputtering (solder). A 0.2 nm Cr layer was used for adhesion of the films to silicon substrate. After the metal deposition, the nanopatterned panels were defined by lift-off metallization in acetone. The patterned substrates were then etched in a planar etcher (Technics PEII-A) at a base pressure of 0.15 Torr to induce grain coalescence. Carbon tetrafluoride (CF₄) and oxygen (O₂) were flowed into the etcher at a rate of 12 sccm and 3.6 sccm respectively and 25W RF power was applied for a time period of 3 mins, unless otherwise stated. The sample was then taken out and analyzed using a JEOL JSM-6700F cold cathode field emission SEM. The relevant bulk physical properties for the materials explored are

Nickel: Ni, melting point, m.p. 1455 °C, density, ρ : 8.88 g/cm³ and linear thermal expansion coefficient, α : 13.3 x 10⁻⁶ °C⁻¹

Zinc: Zn, m.p. 419.58 °C, ρ : 7.10 g/cm³ and α : 30.2 x 10⁻⁶ °C⁻¹

Solder- (depends on the metal composition). For Pb-Sn solder (50/50), m.p.-183-216 °C
, ρ : 8.89 g/cm³ and α : 25 x 10⁻⁶ °C⁻¹

Silver: Ag, m.p.961.93°C , ρ : 10.49 g/cm³ and α : 18.9 x 10⁻⁶ °C⁻¹

Tin: Sn, m.p.231.968 °C, ρ : 5.765 g/cm³ and α : 22.0 x 10⁻⁶ °C⁻¹

2.3.2 Materials Selection Process

We explored a number of metals having relatively low melting points in order to induce grain coalescence. Zinc, solder, silver and tin were deposited on a silicon substrate and they were heated in air. After heating (at 500 °C for 10 minutes) zinc samples in air, zinc oxide nanowires were observed instead of metal reflow. Solder films reflowed at 200 °C, however, solder is an alloy and requires sputtering or electroplating for its deposition, which is not ideal for nanoscale patterning by lift-off. Both Ag and Sn showed good reflow. Hence, we explored the use of Ag and Sn to induce curvature and folding.

In both cases, Ni was used as the base metal panel material. The choice of Ni was motivated by our previous studies on microscale folding.⁵¹⁻⁵³ The material compatibility was ideal in the case of Sn-Ni system, where Sn on top of the Ni layer showed intermediate surface wetting whereas Ag on top of Ni layer showed very poor wetting behavior. The Sn reflowed and due to the sufficient adhesion with the underlying Ni structure, was able to generate enough stress to curl long tubular structure even in the millimeters range (Fig.2.7). Moreover, the Sn was observed to be retained on the Ni surface. Additionally, our experiments revealed that alumina and silica also work as good base materials for the Sn reflow induced curvature process.

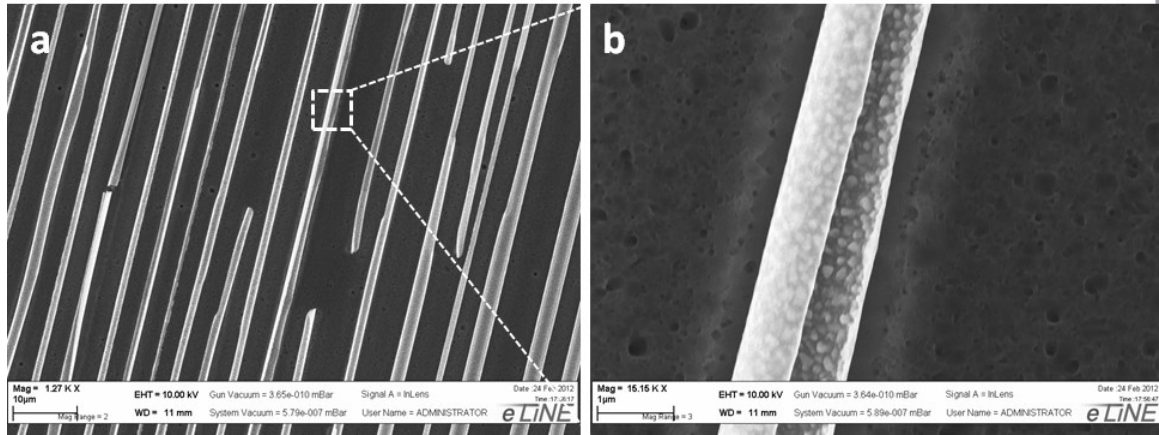


Figure 2.7: Formation of long tubular structures (a,b) SEM images of long tubular structures formed when Sn was deposited atop a Ni film. The stress generated within the Sn thin film due to grain coalescence was large enough to cause the Sn/Ni bilayer to curl up into long tubes.

2.3.3 Role of Plasma Forming Chemistry

It is noteworthy that in all the studies described here, assembly was achieved during plasma etching of the underlying Si substrate. In contrast, earlier work on microscale self-folding was achieved by first releasing the panels from the substrate and subsequently heating them in a high boiling point liquid or in air. As compared to microscale assembly, there are significant challenges on the nanoscale. Oxidation, grain deposition characteristics and intermetallic diffusion can be important and deplete the reflowing hinge material. The right balance of CF_4 and O_2 is also important since low concentrations of O_2 limits the Si etching rate as reactive fluorine radical concentrations are enhanced on addition of oxygen. However, if the O_2 concentration is too high, oxidation of the metals can result. Hence, etching of the underlying Si has to be in

harmony with inducing Sn grain coalescence to result in the optimum curling to result in the nanotubes geometries (Fig 2.8).

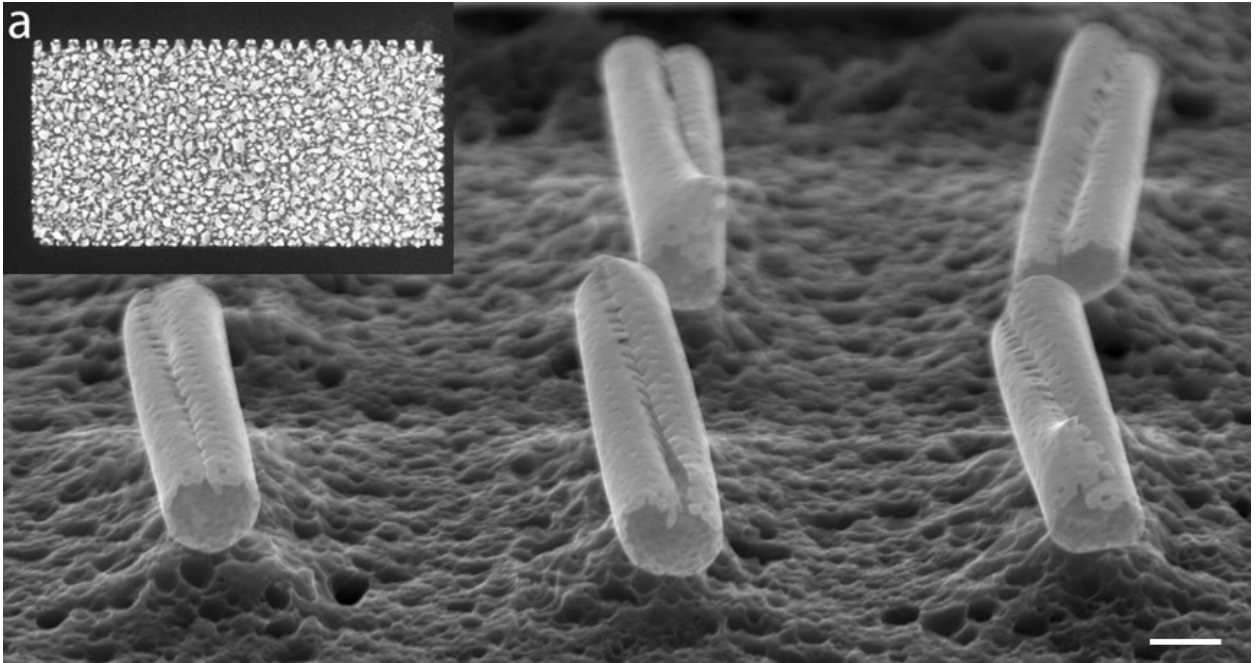


Figure 2.8: Formation of nanotubes (a) SEM images of nanotubes formed by tin reflow process by specifically optimizing the design and etching time. Inset shows structure before folding. Scale bar at 1 micron

2.3.4 Understanding the role of geometry optimization in folding

We wanted to understand the time course of events when rectangular structure curls. Figure 2.9 shows the experimental evolution of the rolling process of two single rectangular Ni-Sn membranes as they are released from the substrate at three different etching times. Although the etching proceeds isotropically from all sides, it can be seen that folding pathways needs to be controlled for the final structure to fold into a tubular form.

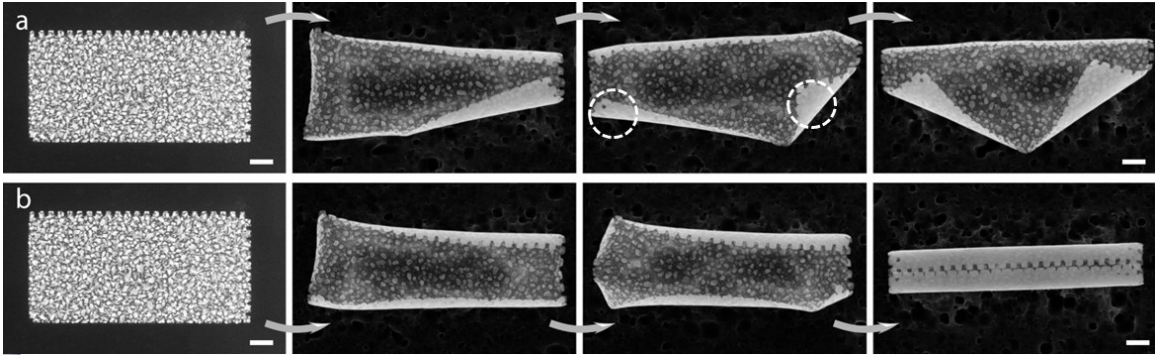


Figure 2.9: Engineering folds by engineering lithographic patterns (a) Image series showing the formation of large folds at the corners with patterned nanoholes (b) Image series showing the formation of a tight tube with interlocking the edges resulting from a uniform etching along the length of the panel (Scale bar 500 nm).

This leads to the conclusion that while it is important that the etching proceeds isotropically from all sides, the folding process has to remain uniform along the length of the membrane for it to form a tubular structure. Once a large fold has occurred, it is highly improbable that the folding will correct itself to enter into the tubular configuration. This gives an opportunity to control the structure formed by engineering the etching geometry of the underlying substrate. For example, the incorporation of asymmetric lithographic patterns on the folding membrane (such as through holes or other geometries) will induce faster etching of the underlying Si in the vicinity of the pattern compared to the unpatterned end, leading to a faster release of the membrane on that edge. Such an approach can be used to induce curling from preferred edges or sides, keeping the other sides as pivotal points (Fig. 2.9).

2.3.5 Incorporation of Lithographic Patterns in Folded Structures

Since our methodology is compatible with nanolithographic patterning techniques such as e-beam lithography or nanoimprinting, it offers the ability to incorporate patterned geometries in the folded structures. We were interested in fabricating mesh-like materials and began with rectangular sheets of (2.5micron by 1micron). Again we observed that the sheets curled into tubes in distinct orientation of the nanopatterns with respect to the axis of the tube (Fig 2.10).

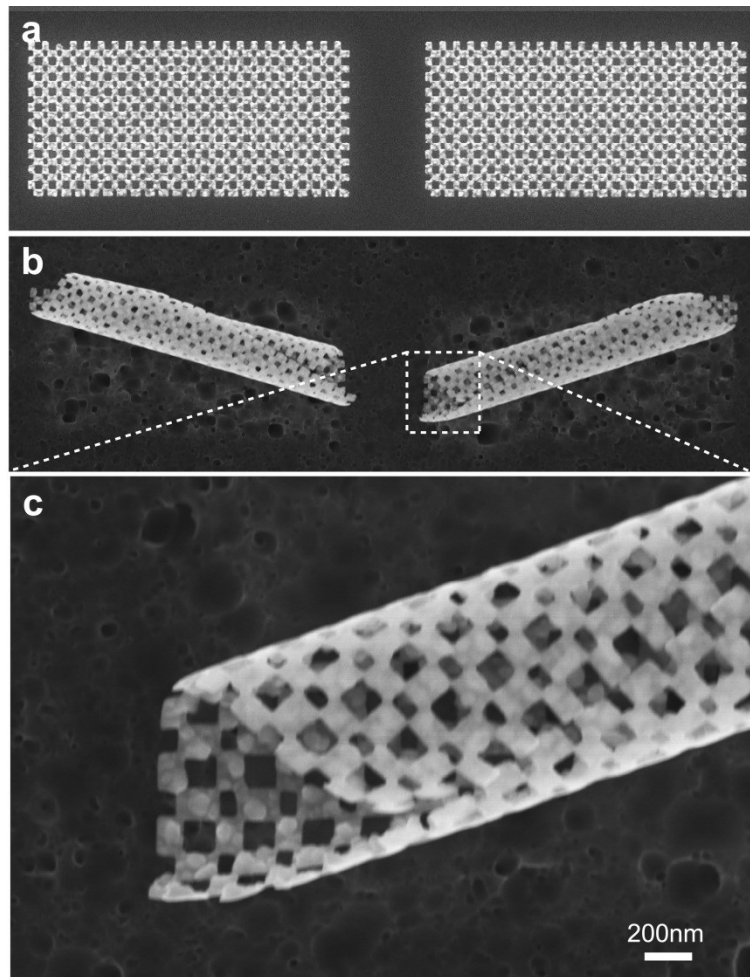
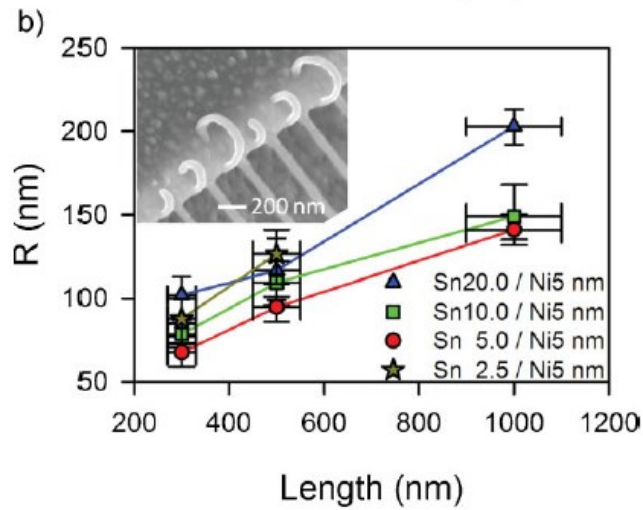
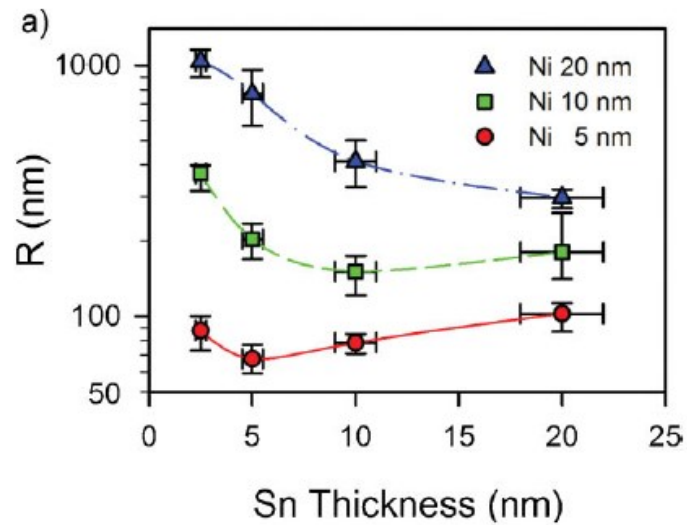


Figure 2.10: Nanomesh tube formation (a) SEM image of the mesh pattern before folding. (b) SEM image of the mesh patterns folded in to tubular geometry. (c) A magnified image of the nanomesh tube with the mesh patterns clearly visible.

Further, in order to study the geometric factors affecting curvature, we designed 2D cantilever shaped Ni/Sn bilayers with varying thickness (T), length (L), and width (W) using e-beam lithography and lift-off metallization. We observed that the radii of curvature (R) varied considerably when T, L and W were varied (Fig. 2.11).



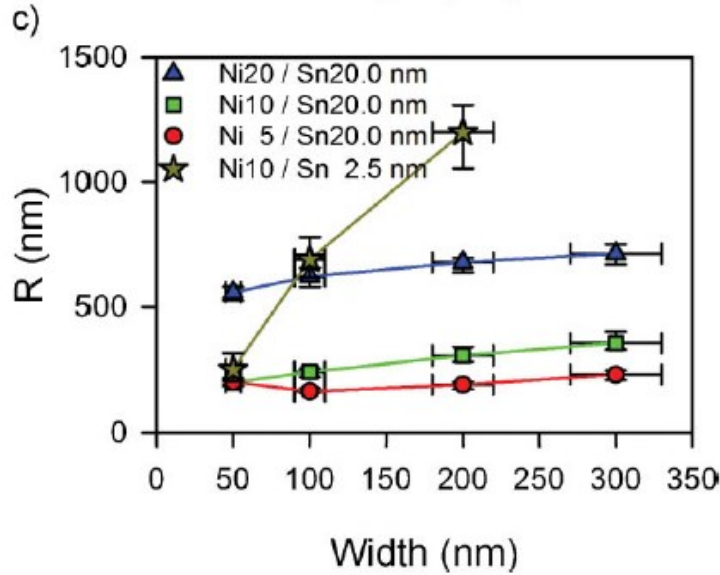


Figure 2.11: Experimental results showing the variation of the radii of curvature with the cantilever geometry. (a) Variation in thickness ($L=300$ and $W=50$ nm). (b) Variation in length ($W=50$ nm). (c) Variation in width ($L=1000$ nm).

Longer and wider cantilevers both curved with larger R values (Fig. 2.11 b,c). This observation is advantageous in predicting the folding dynamics and hence in designing more complex geometries. For the same deposition thickness of Sn, bilayer cantilevers composed of thinner Ni films showed tighter radii of curvature (i.e. smaller R , Fig. 2.11a [$W=50$ nm and $L=300$ nm]). In this cantilever geometry, we observed average R values as low as 70nm (at a 5nm Sn and 5 nm Ni thickness).

In particular we fabricated short arms (Fig 2.12c) and we made longer arms (Fig 2.12d) by varying the exposure rate during e-beam lithography. The arm width varied slightly due to the exposure difference (10nm vs 30nm). This difference in geometry was also seen to influence the size of the tin grains deposited and was in turn found to influence the radii of curvature of the final folded structures (Fig 2.12).

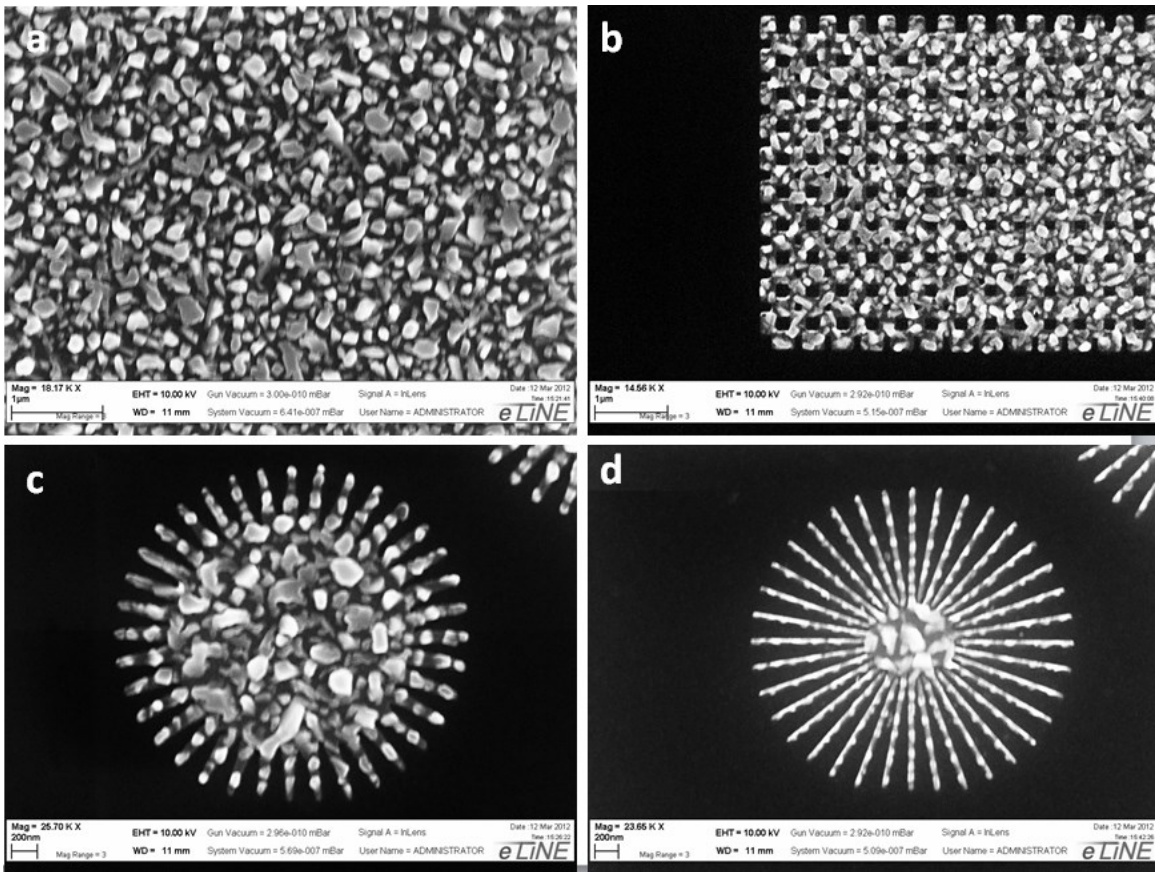


Figure 2.12 SEM images showing the variation of grain size the cantilever geometry
 (a) Grain size on large microscale area (b) Smaller grain sizes can be seen as nanomeshes are designed. (c,d) Short and long arms can be seen to show a vast difference in the grain size.

In order to demonstrate the versatility of the approach, we created structures of various geometries including, “nanovenus flytraps” (Fig 2.12), “nanoflowers” (Fig 2.13), “nanogrippers” (Fig 2.14) and “nanoslap bracelets” (Fig 2.15) as shown below. The geometric influence and effect of grain size in the radius of curvature is apparent by comparing the folded 3D structures.

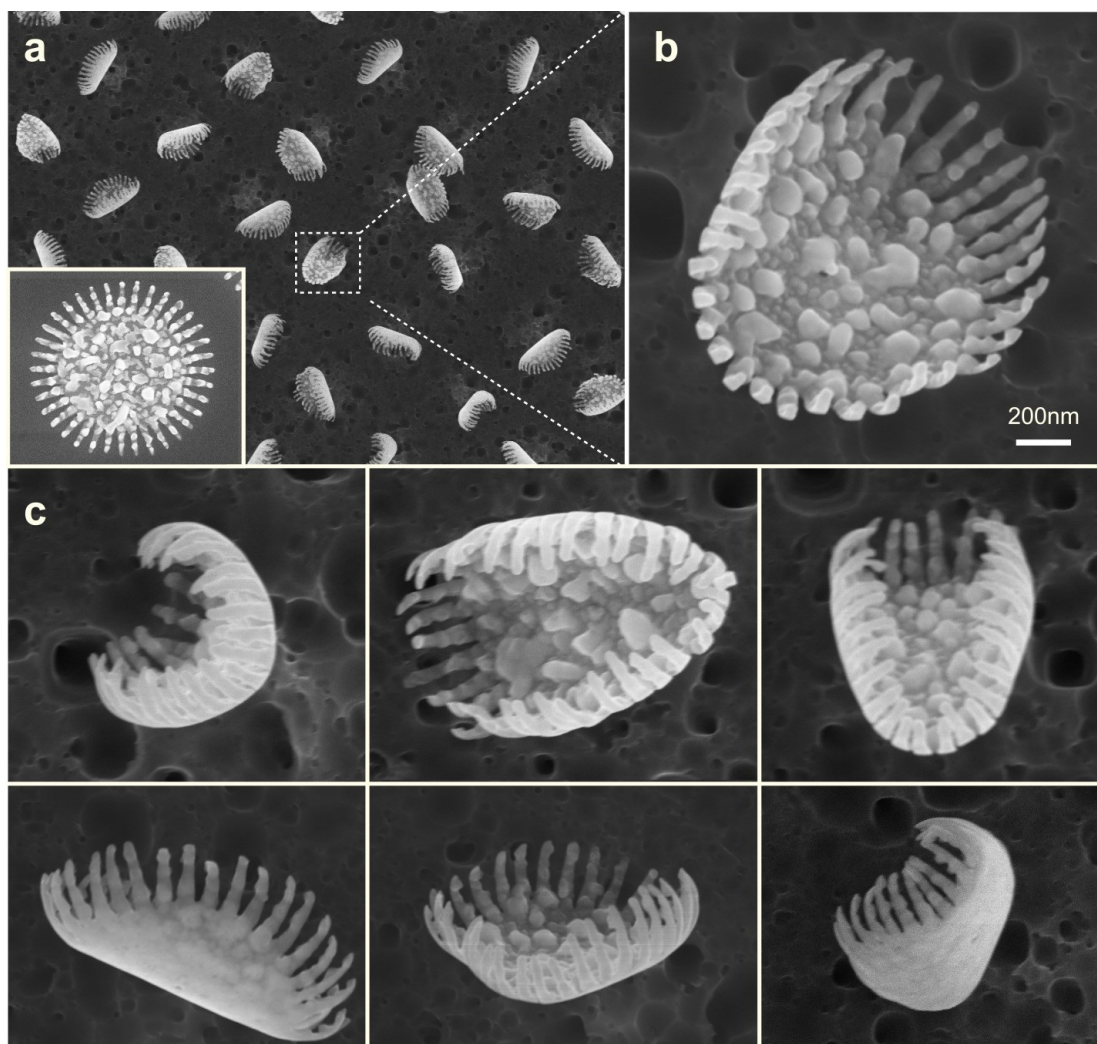


Figure 2.13: Formations of Venus fly trap like fringed Nanoparticles (a) SEM image of an array of Venus fly trap shaped nanoparticles, inset shows the pattern before folding. (b) Magnified image of a fringed nanoparticle. (c) Images of various folded nanoparticles.

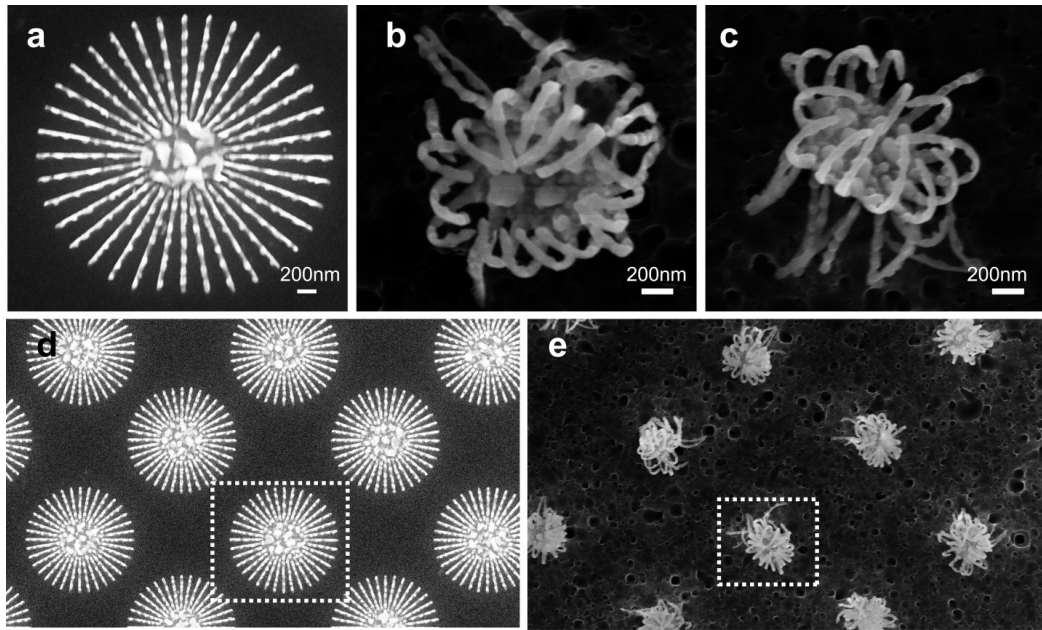


Figure 2.14: Nanoflower pattern (a) Nanoflower pattern formed by radial lines before folding (b-c) Magnified image of the folded nanoflowers showing different angles (d) Array of nanoflowers patterns before folding (d) and after folding (e).

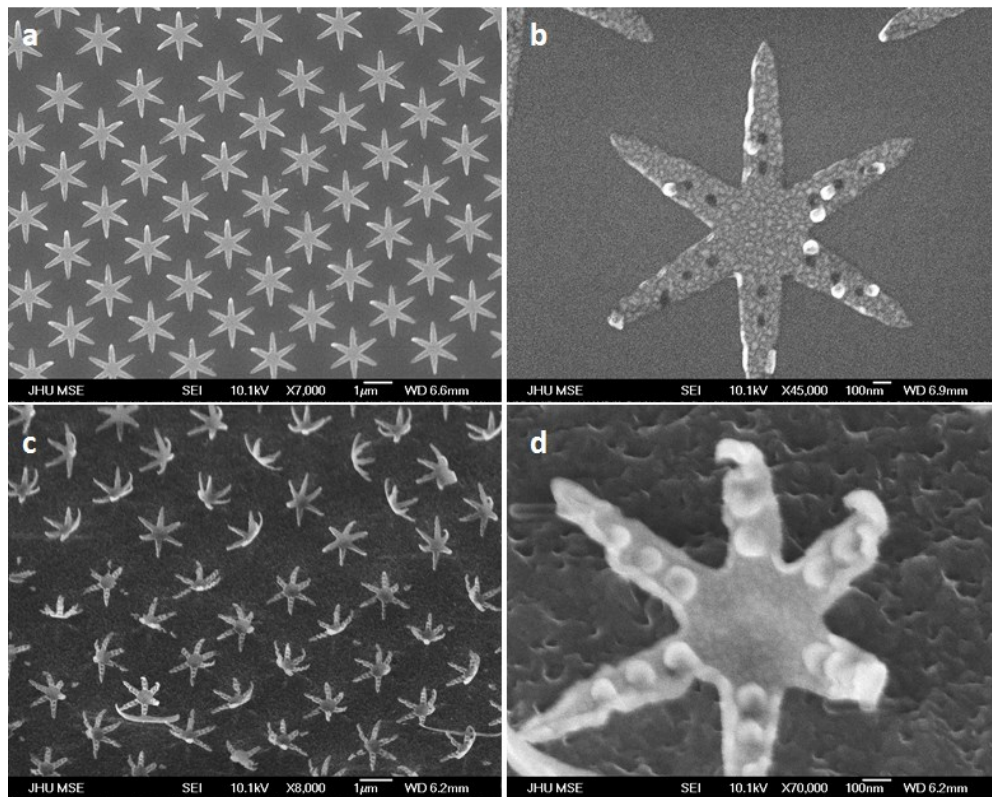


Figure 2.15: Nanogripper fabrication (a, b) Before folding (c, d) After folding

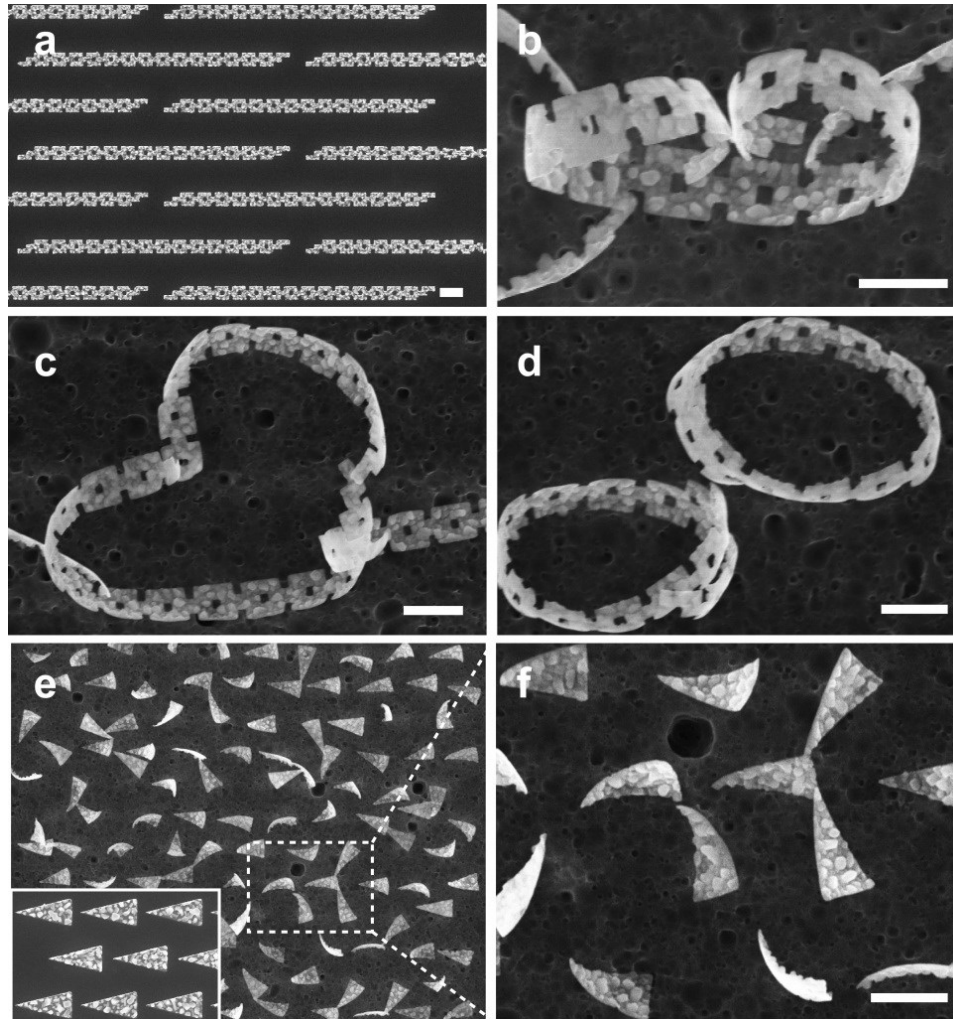


Figure 2.16: Nano-slap bracelets and claws (a) SEM image of linear belt like nanopatterns before folding and (b-d) various 3D shapes formed after etching showing the belts coupled with each other (e) array of triangular nanostructures after folding (inset shows the 2D panels before folding) (f) Magnified image of the folded claw like nanostructures. Scale bars show 1micron.

2.4 3D Assembly of patterned hinged nanopanels

As in the case of biological self-assembly, several paradigms such as steric constraints, hierarchical forces, and lock-and-key interactions can be utilized to direct the assembly for specific outcomes. In a similar manner, for self-assembly of polyhedral nanoparticle we utilized 2D nanoscale panels with binding sites on their edges and thus by joining the nanoscale panels in 2D prior to assembly, the desired outcome can be obtained. In this method, we thus use untethered panel that do not form an organized structure is preorganized with a series of hinges in 2D. These patterned panels were shown to self-assemble by bending Sn hinges into cubic particles. This assembly approach is limited only by the 2D patterning resolution. The details are discussed in the following section.

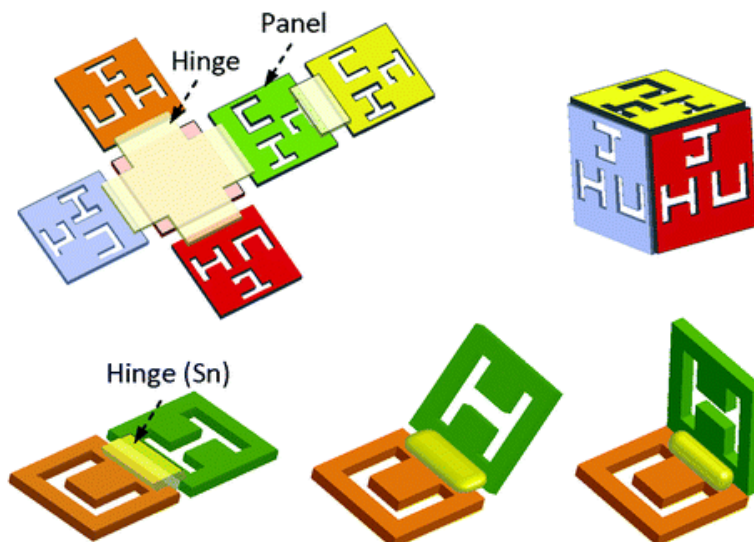


Figure 2.17: Schematic diagram showing the concept behind the self-assembly process of hinged nanopanels Image source from Reference ⁴⁵ Copyright 2009 American Chemical Society.

2.4.1 Fabrication Process

We fabricated 2D nets with five or six square nanoscale panels desired patterns such as that shown in Figure 2.18. This was done using EBL and lift-off metallization. The panel dimensions ranged from 500- 1 μ m in width and 3–30 nm in thickness. The gap between panels was 50–100nm (10% of the panel dimension). We utilized nickel (Ni) to pattern the panels and tin (Sn) to pattern the hinges.

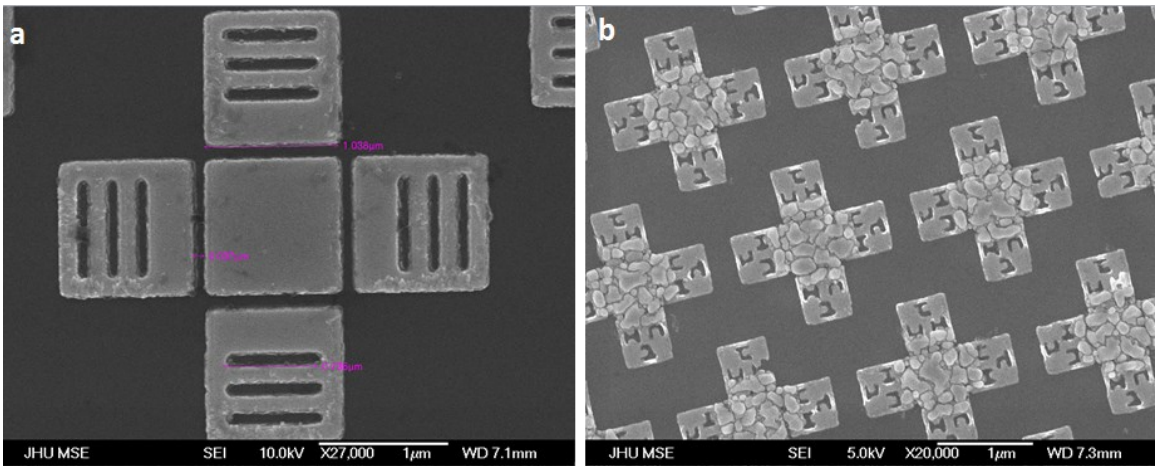


Figure 2.18 SEM Images of a 2D nets before plasma etching (a) Cruciform structure of Nickel before the 2nd lithography to deposit hinges (b) After the deposition of tin metal at the hinges patterned by 2nd layer of lithography.

After the patterning of the faces of the polyhedral particles (Fig. 2.18a) and the hinges between them followed by the deposition of the corresponding materials (Fig. 2.18b) as described above, the samples were plasma etched for an optimized time. Within this time period the panels were found to self-assemble as can be seen in Figure 2.19. By controlling the etching time, it was possible to control whether the particles were completely released or partially released from the substrate Figure 2.20. The important

parameter was that the panels needed to be released from the substrate while simultaneously during reflow in order to allow them to orient and assemble into the desired 3D particle. We found that both these process happened simultaneously in approximately 1–2 min for a 500nm particle.

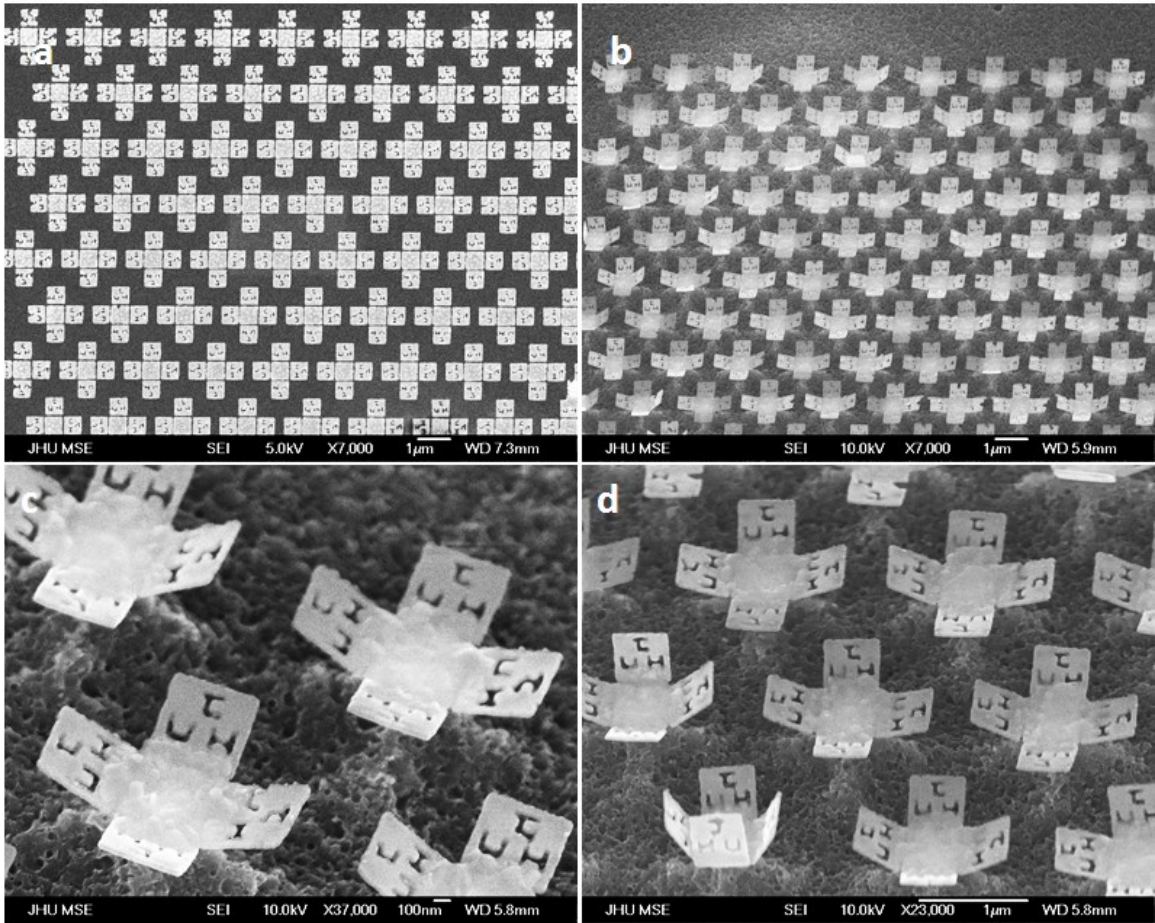


Figure 2.19 SEM Image of hinged particle folding process (a) SEM Images of 2D nets before plasma etching. (b, c, d) images showing that the 2D nets assemble after plasma etching.

Another important parameter is the flow rate of O_2 gas during etching. It was found that the angular orientation of the panels is dependent upon the etching conditions

especially the oxygen concentration. In all the particles, the central panel did not have any pattern while the other panels had some designs on them (Figure 2.18a). The CF_4 rate was kept constant and the O_2 flow rate was slowed down to 0.2sccm. In this case, the grain reflow was very small and the angles corresponding to this flow rate showed about 45deg. While a flow rate of 3.6sccm of O_2 showed increased grain coalescence and larger angles ($\sim 90\text{deg}$).

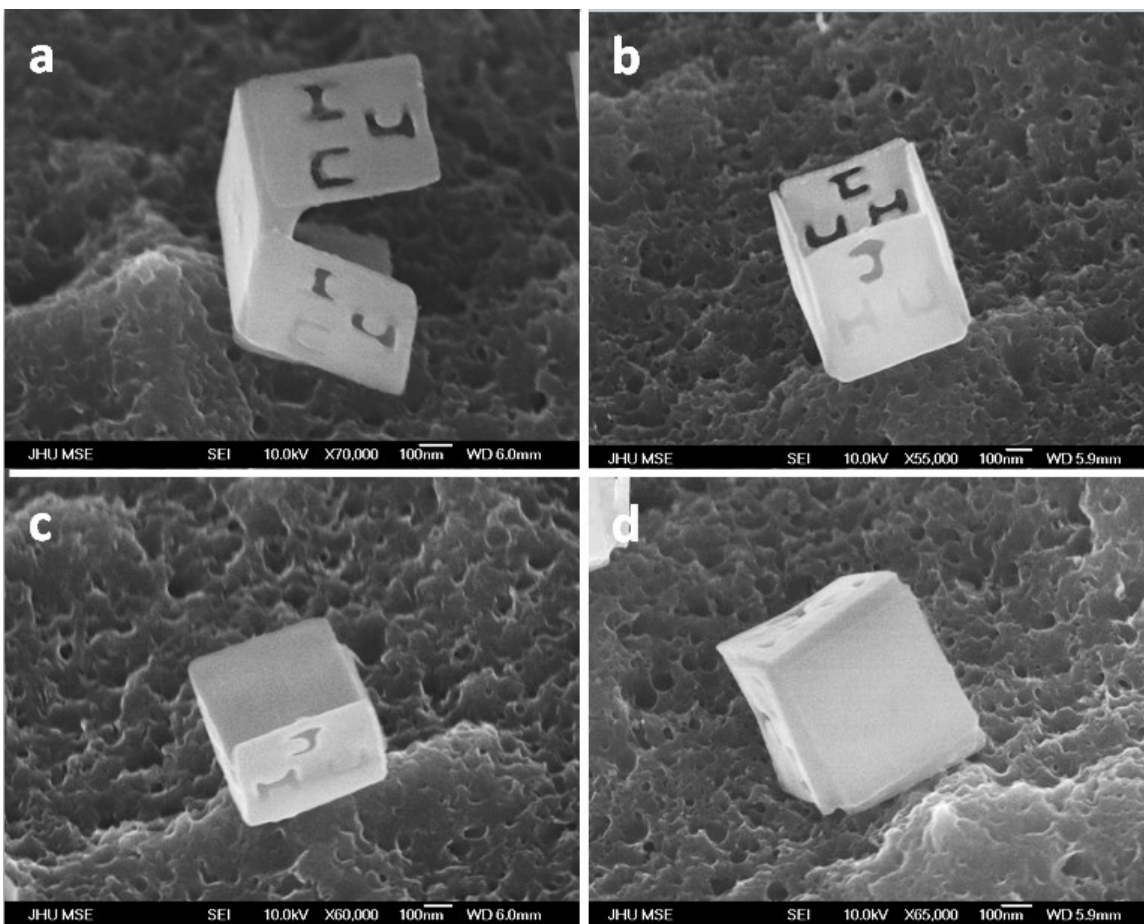


Figure 2.20 SEM images showing that the 2D nets assemble into box structure which are completely released from the Si substrate

Using this method, we can construct both free-standing and attached nanoparticles. In addition, these particles can be constructed with any desired nanoscale

pattern. Also, as the orientation angle between panels can be controlled, this method can be used to construct other polyhedral particles. In addition, they can be made multilayered and hence could display novel optical properties, such as unique plasmon resonances. Further, these hollow particles can be used as nanoscale encapsulants for drug delivery and other applications.

2.5 Material Characterization Processes

Work is currently underway in characterizing the underlying material property changes that occurs during the reflow process.

2.5.1 EDX Elemental Color Mapping

A qualitative energy dispersive spectroscopic elemental color heat map was performed to understand the spatial uniformity of the materials (Fig 2.21). The elemental mapping on the folded nanotubes indicated that the constituent elements Sn and Ni were uniformly distributed over the entire length. Further, the color mapping of Si substrate (Fig 2.21a) indicated no inter mixing of Si with the nanotube architecture during the etching process.

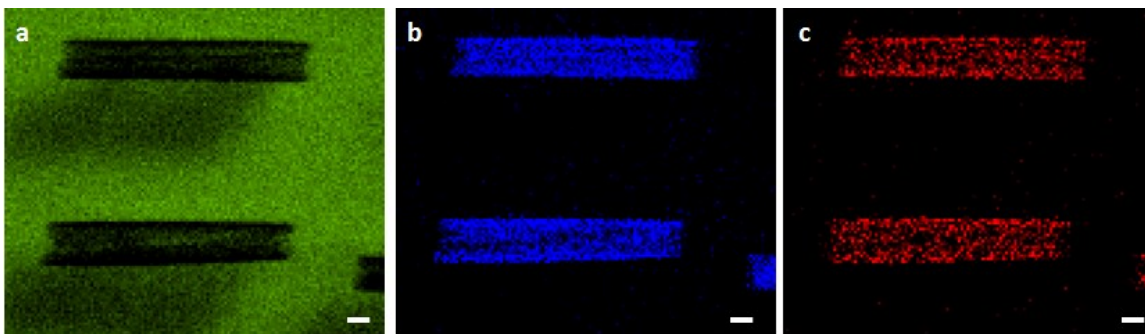


Figure 2.21: EDX elemental color heat mapping of rolled up nanotubes (a) silicon (b) Sn (c) Ni. Scale bar at 1 micron.

2.5.2 EBSD Analysis of folded structures

Electron back scatter diffraction (EBSD) is a technique that can offer orientation information about each individual grains in a sample surface. Information on the size of the individual grains can also be deduced from the differences in the lattice orientations obtained from a step by step scan. We performed EBSD analysis on the folded sample to distinguish textures in the Sn thin film to understand the preferred orientation of the component phases. The analysis is performed in FEI Quanta 200 FEG Environmental-SEM equipped with an integrated EBSD system.

The thickness of the Sn film used for most of our curling structures was 5nm. First, the appropriate acceleration voltage for the electron beam to obtain the most information from the Sn layer (penetration depth ~5nm) was chosen by using Monte Carlo simulations. Fig.2.22 shows the Monte Carlo simulations for penetration depths resulting from electron beams of acceleration voltages 15kV and 5kV. For 15kv electrons were found to be backscattered from depths of around 500nm in the sample. For 5kV backscattered electrons were mostly obtained from the top 5-10nm (Sn region) of the sample and was chosen to be the voltage for the EBSD analysis.

For EBSD analysis briefly, the sample is first tilted to an angle of about 70° and an electron beam is exposed to the sample. SEM image of the nanoline geometries after the Sn reflow process is shown in Fig. 2.23a.

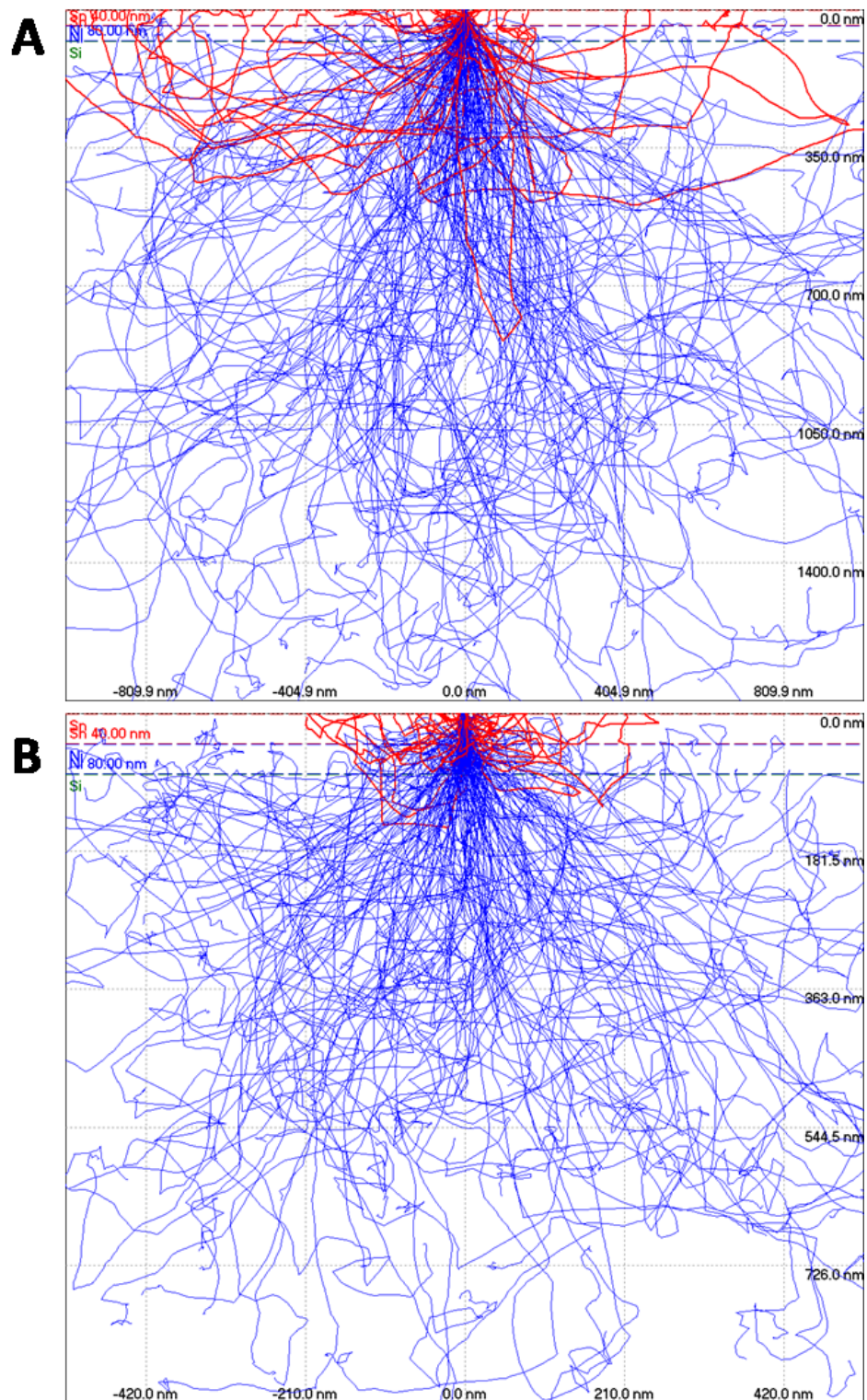


Figure 2.22: Monte-Carlo Simulation for penetration depth at acceleration voltages of 15kV (a) and 5kV (b). (5kV chosen for EBSD analysis)

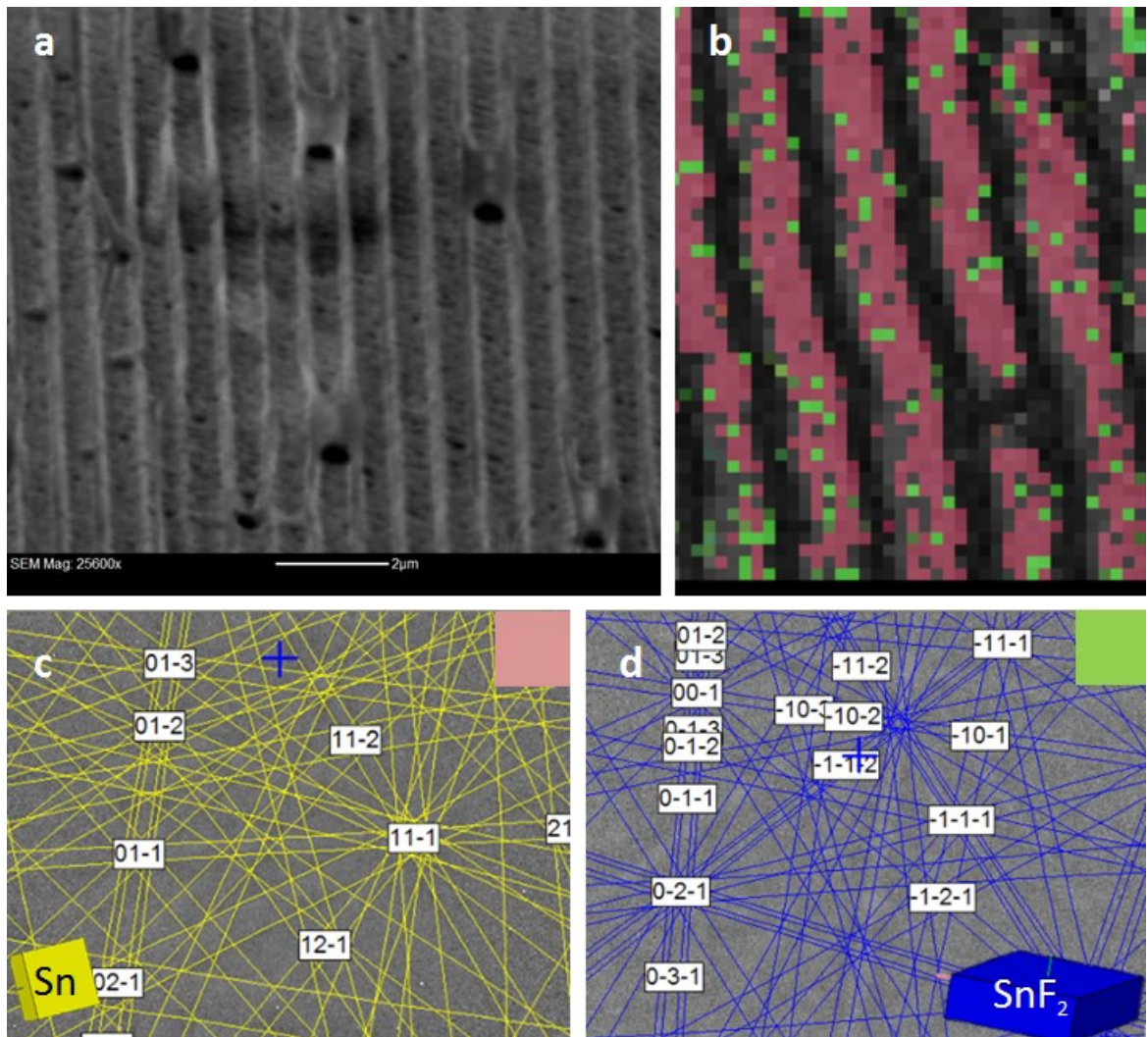


Figure 2.23: Phase map of nanoimprint lines (a) Nanoimprint lines after etching (b) EBSD phase mapping of nanoimprint lines after Sn reflow process.(c) and (d) shows the Indexed Kikuchi pattern of Sn and SnF₂ generated from the phase mapping as shown by the color code.

The backscattered diffracted electrons from the sample are used to form a “kikuchi” pattern on the fluorescent screen of the system. Information on the crystalline lattice and its orientation can further be obtained from the Kikuchi diffraction pattern.

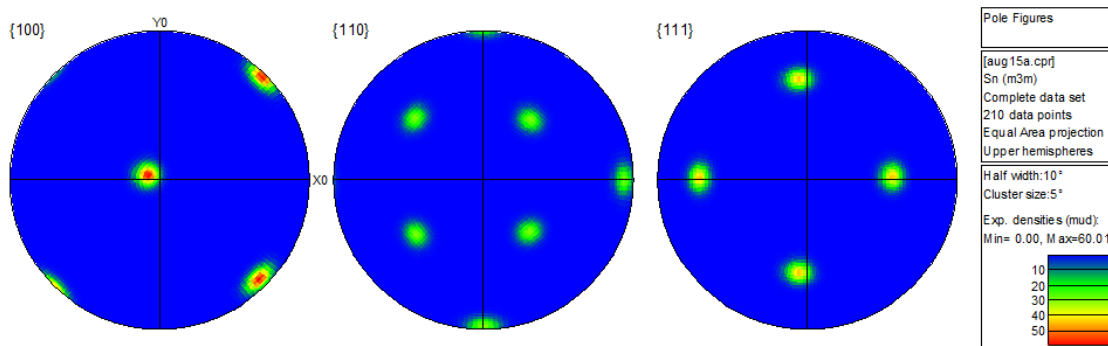


Figure 2.24: Pole figure of Sn obtained from phase map analysis of the nanoimprint lines

The crystal orientation and the phase of the analyzed area are decoded from each of the Kikuchi pattern corresponding to each pixel. This information on the orientation and phase is then mapped over the whole of the region (Fig.2.23b). The microstructure of Sn after reflow indicates the presence of large grains as a result of the grain coalescence. The orientation information of Sn grains is also shown in the pole-pole plots (Fig. 2.24). The information on the phase of the sample after plasma induced Sn reflow was found to be composed of Sn existing in two different phases as pure Sn and SnF₂. The Kikuchi patterns corresponding to Sn and SnF₂ are shown in Fig. 2.23c and d.

2.5.3 HRTEM Analysis

The changes in the lattice characteristics at the Ni-Sn interface after the reflow process is being characterized using high-resolution transmission electron microscopy (HRTEM). For analysis in the transmission electron microscopes (CM100 TEM and Philips CM200 FEGTEM), samples were dispersed in ethanol and dropcast on 200 mesh copper grids with holey carbon film (Electron Microscopy Sciences). TEM images of the surface of the Sn film after plasma induced folding is shown in Fig.2.25a. Magnified images of the Sn surface (Fig. 2.25b and c) indicate surface smoothing due to the grain coalescence.

We also looked at the diffraction pattern of the Ni-Sn interface and was found to show crystalline nature (Fig. 2.25d).

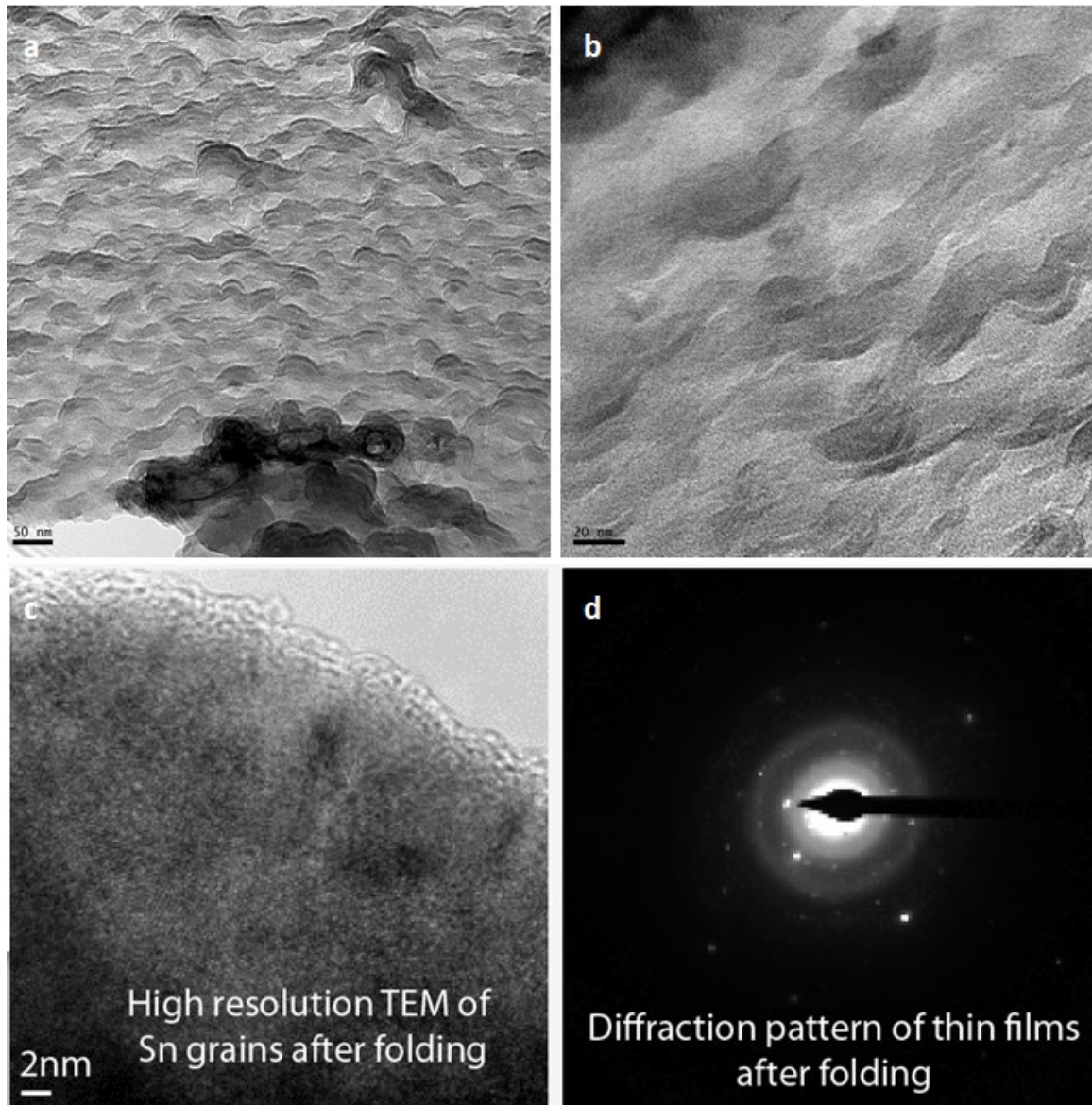


Figure 2.25: High resolution TEM image of Sn grains and diffraction pattern of the thin films (a) Shows the grain reflow on the surface after etching (b,c) Magnified image of the surface (d) Diffraction pattern of the Ni-Sn interface.

2.6 Mass Production of 3D Nanostructures[§]

2.6.1 Utilization of nanoimprint lithography to pattern geometries that self-assemble

The previous sections presented the creation of precisely patterned nanoparticles and curved nanostructures using Sn reflow based self-assembly. However, these approaches utilized e-beam lithography to pattern the 2D templates in a serial manner and as result is limited by the number of structures that could be formed. As described in the introduction chapter, an alternative top-down approach to generate precise nanoscale patterning in a parallel fashion is nanoimprint lithography (NIL). This section presents our work on the investigations to utilize nanoimprint lithography to mass produce such structures in a relatively cost-effective manner (Fig 2.26).

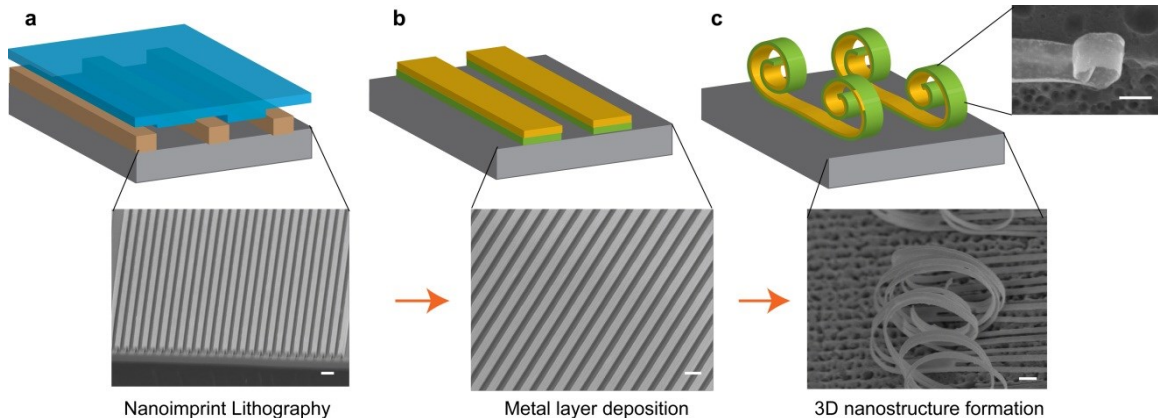


Figure 2.26: Nanoscale origami of nanoimprinted patterns (a) Nanoimprint lithography for making large area of nanoscale 2D patterns (b) Thin film deposition and (c) Folding of nanostructures by plasma etching Scale bar shows 500nm.

[§] The work reported in this section is based on the following manuscript in preparation James, T., Park, S-Y,..., Gracias, D. H. Mass scale production of 3D nanostructures using Nanoimprint lithography

NIL is a high throughput methodology for nanoscale patterning of structures based on mechanical contact and material displacement. The process involves the use of a rigid stamp (typically made of silicon) that is brought into mechanical contact with an imprint resist to create an impression of the stamp. This stamp pattern can then be transferred to other materials by utilizing dry etch and lift-off processes (Fig. 2.26a). The high-throughput feature of the process is a consequence of the fact that the rigid stamps can be cleaned and reused over multiple cycles. The two predominantly utilized methods for NIL are UV-NIL and thermal-NIL; the main difference being that the UV-NIL process can be achieved at room temperature and utilizes liquid films or droplets, whereas thermal-NIL utilizes thermoplastic resist films as polymethylmethacrylate (PMMA) or polystyrene (PS). All of our NIL patterning results, detailed later, were obtained using thermal-NIL with a PMMA resist. Here, we utilized thermal-NIL to pattern metallic structures, the details are outlined below.

2.6.2 Fabrication of nanostructures by Nanoimprinting Process

We utilized the Nanonex NX-2000 NIL system for the nanoimprint lithography process. The molds used for nanoimprinting were fabricated by e-beam lithography and some were commercially purchased (Fig. 2.27). For the patterns that were written using e-beam, they were developed using MIBK:IPA at 1:3 ratio for 60 secs. A thin chromium layer (10nm) was deposited as an etch mask. The mold was created by etching silicon to a depth of 300nm using deep reactive ion etching and then coated with an anti-sticking layer to prevent adhesion during imprinting. Figure 2.28 shows imprint molds for foldable nanobox (a and c), tetrahedron (b and d) and star like panels (e and f). NXR 1020 resist 6% was spun coated at 800 rpm and imprinted. The thickness the resist layer

before imprinting was about 380nm. The imprinting step was carried out at 130 °C and 210psi pressure for a processing time varying from 1min to 5mins depending on the pattern geometry.

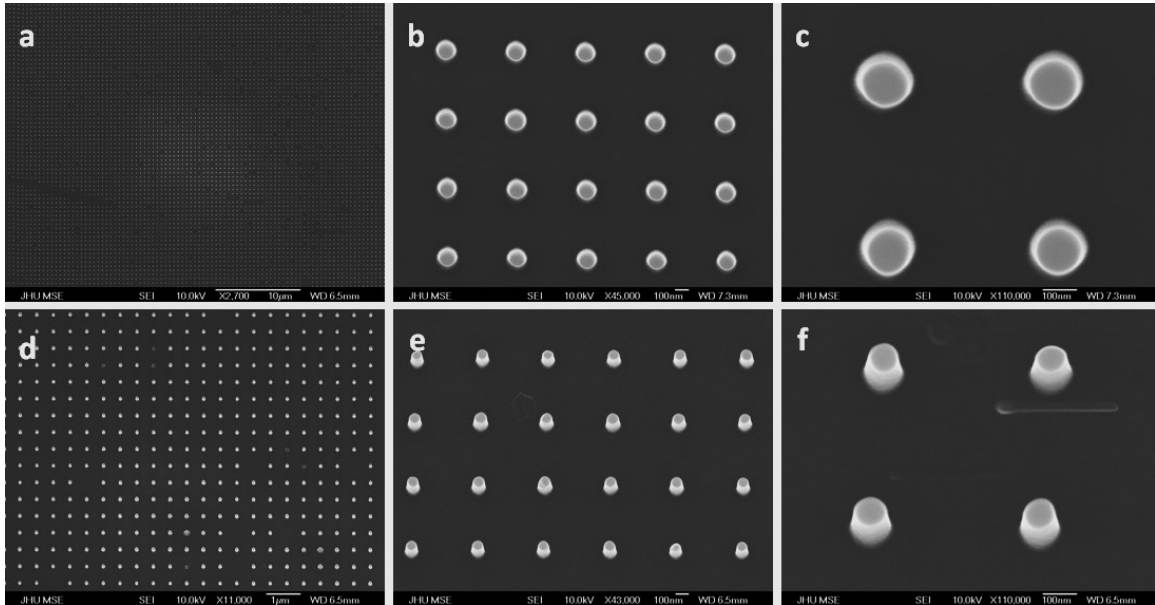


Figure 2.27 Commercial Nanoimprint Stamps: Nanoimprint circular stamps of diameters (a-c) 130 and (d-f) 105nm.

The sample was then cooled down and the mold was separated from the sample manually using a micro blade. The imprinted sample was plasma cleaned in oxygen plasma to remove the residual resist layer which was approximately 80nm in thickness. A thin layer of Chromium for adhesion and desired thickness of nickel and tin was patterned on the imprinted sample using liftoff metallization. The folding of the nanostructures was carried out in Plasma Therm 790 etcher with a CF₄ flow rate of 25sccm and oxygen of 4sccm. The total pressure in the chamber was set to 500mT and the power applied was 50W. Under these conditions, the silicon underneath the nanostructures was etched away releasing the patterns, while at the same time the tin

grain coalescence drove the self-assembly of the structures same as described before in the previous sections. The structures, if not entirely etched were tethered on the silicon and hence remained on the surface of the silicon for imaging.

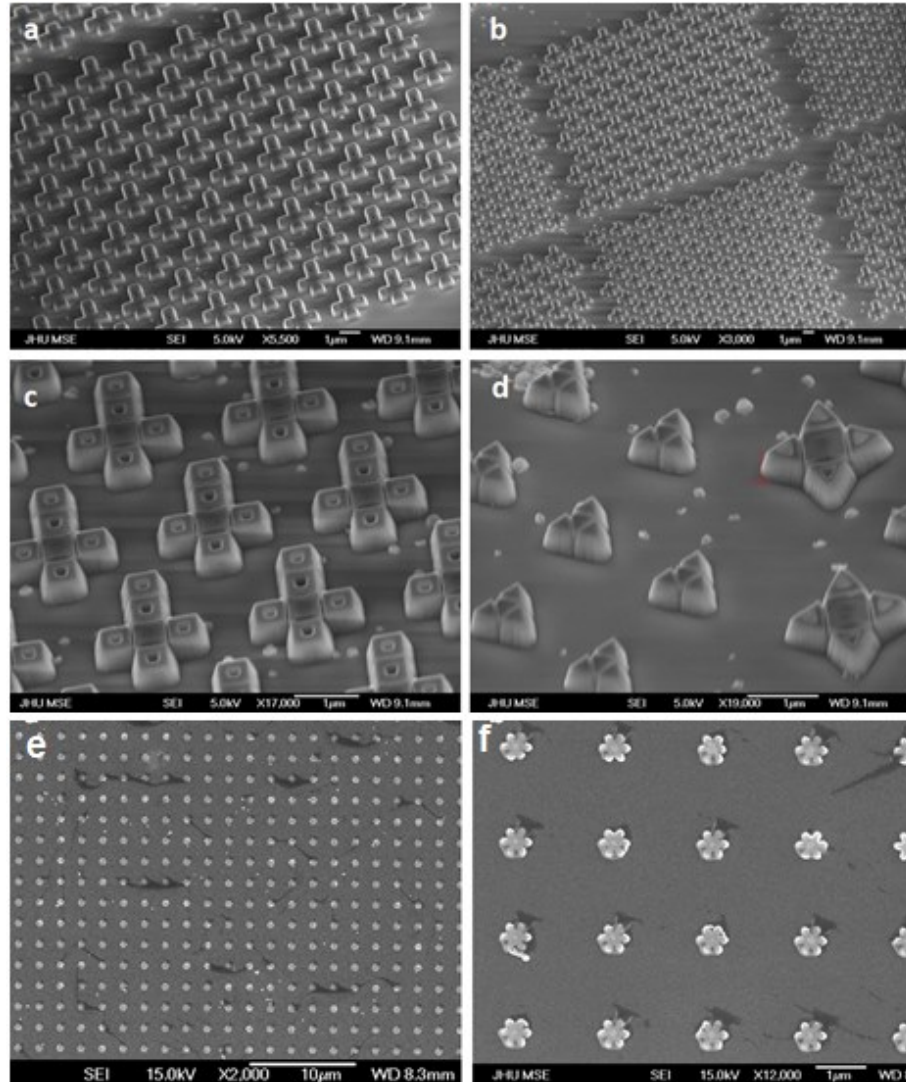


Figure 2.28: Lab fabricated nanoimprint stamps (a and c) Nanoimprint stamps fabricated in the lab for foldable cruciform panels to form nanoboxes (b and d) nanoimprint stamps for foldable panels to form tetrahedrons and (e and f) nanoimprint stamps to create panels for folded nanostars.

2.6.3 Examples of 3D folded nanostructures via nanoimprint lithography

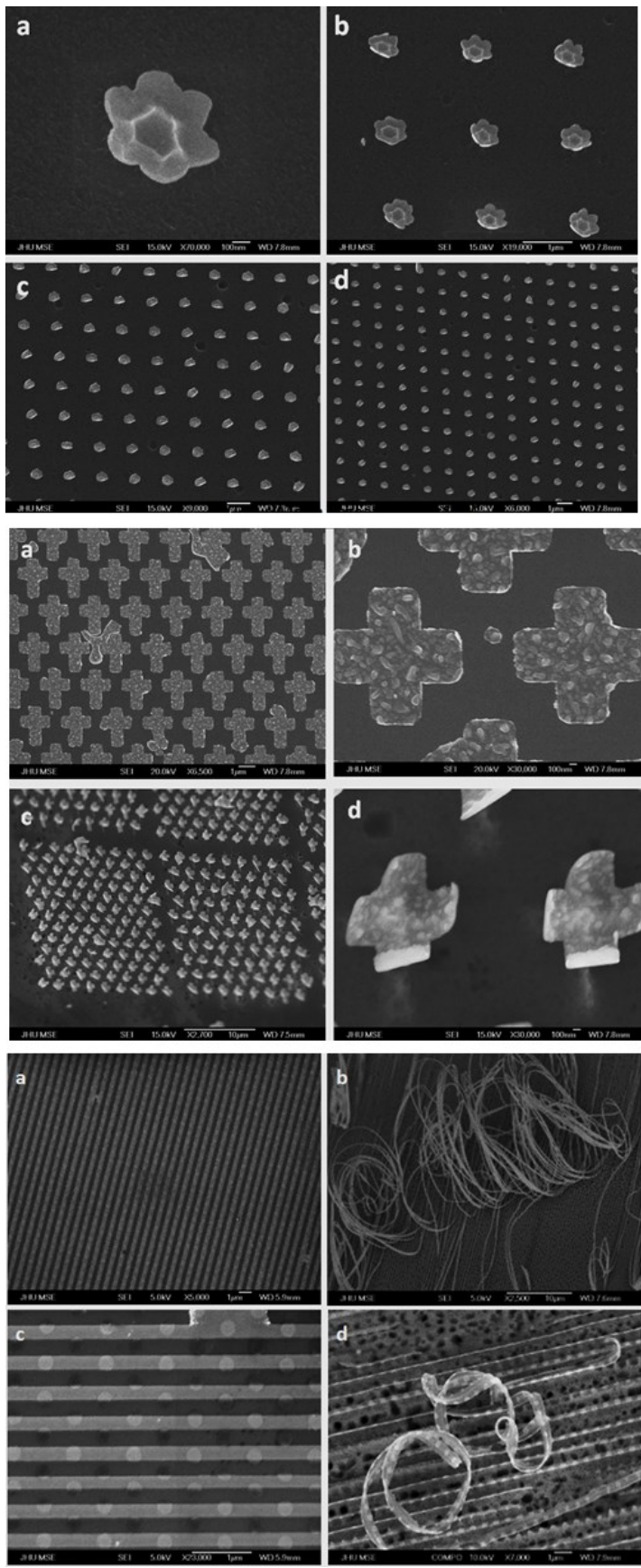


Figure 2.29: 3D folded nanostructures patterned using nanoimprint lithography. Top (a) shows magnified image of a 3D folded plasmonic nanostar. (b, c and d) shows the zoomed out image of the array of nanostars. Middle (a and b) shows magnified and arrays of cruciform geometries before folding (c and d) shows array and magnified image of the folded structures. Bottom (a and c) shows image of nanowire geometries of various widths before folding. (b and d) shows 3D structures of corresponding nanowires after folding.

We investigated the feasibility of mass-scale production of 3D nanostructures using the large area nanoimprint lithography patterned features of various geometries. Fig. 2.29 shows examples of geometries including plasmonic nanostars, cruciform geometries and nanowires of various widths.

2.7 Conclusions & Outlook

In conclusion, we have described self-assembly of 3D nanostructures. The strategy works well with panels composed of Ni, alumina or silica with Sn hinges; the use of other materials such as polymers are being explored. Our strategy is easy-to-use and only requires simple thin film deposition (thermal evaporation) which is widely accessible. Further, the strategy is compatible with all 2D nanoscale patterning techniques such as advanced photolithographic (phase shift etc.), e-beam, probe and nanoimprint lithography. Hence, it leverages already existing infrastructure and enables the creation of lithographically patterned 3D nanostructures. Applications of these previously non-existent nanostructures in optics, electronics and medicine continue to be explored.

CHAPTER 3

Nanopatterning of Silicon by Catalytic Etching[§]

Development of approaches for cost effective ways of realizing rapid nanoscale patterning in silicon is of importance in the advancement of nanoelectronics, photonics as well as biomedical sciences. The currently used strategies for nanopatterning silicon involves the use of high energy particles as in the case of ion beam sculpting or electron beam drilling methods to create nanopores in Si. These methods being done in a serial fashion are very time consuming to generate patterns in a large area and are also expensive as they demand access to high MeV or GeV energy sources. Alternative approaches for the rapid formation of nanoscale patterns in silicon in a parallel manner are thus highly desired. In this chapter we present a novel approach for the spontaneous formation of nanoscale patterns in silicon by utilizing the catalytic wet and dry (plasma) etching of silicon in the vicinity of noble metal geometries. Further, this method can also leverage up on the well-established nanolithographic techniques such as e-beam or nanoimprint lithography to pattern various geometries noble metal films. Using this method, we demonstrate the creation of three dimensional structures such as nanopore arrays and gold (Au) nanoparticles (NPs) coated micro or nano wells and channels in

[§] C The work reported in this chapter is based on the following original publication: James, T., Cho, J. H., Fernandes, R., Randhawa, J. S., Gracias, D. H. A one-step etching method to produce gold nanoparticle coated silicon microwells and microchannels. *Anal. Bioanal. Chem.* 398, 2949-2954 (2010) Copyright 2010 Springer.

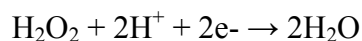
silicon in a highly parallel manner. Further, this methodology provides versatility in the types of micro/nano structures of the pattern that can be formed by varying the shape and dimensions of the metal (Au) patterns and the etch time.

Catalytic etching of silicon has been of interest in the recent years due to their immense potential in creating through holes and other structures in silicon in a rapid manner. Catalytic wet etching of silicon has been investigated in detail by a number of studies. However, we have recently discovered that the dry plasma etching of silicon can also be catalytically enhanced by the presence of noble metal geometries. Our results demonstrate that this can be used in the creation of various microfluidic as well as other structures in silicon. In the next sections two etching process; MaCE and MaPE are discussed in detail. The theory behind both the processes shall be discussed along with the application in making arrays of nanopatterns of various geometries in Si.

3.1 Metal assisted Chemical Etching (MaCE) of Si

It is well known that noble metals such as Au and Ag enhance the wet etch rate of Si with hydrogen fluoride (HF) and hydrogen peroxide (H₂O₂) and this process, sometimes referred to as MaCE (Metal assisted catalytic etching) has been used to form deep pores and vias in silicon.⁵⁴⁻⁵⁶ In this process, it has been suggested that the surface of Au particle facing the etching solution (hydrogen fluoride (HF) and hydrogen peroxide (H₂O₂)) acts as the cathode, which catalyzes H₂O₂ reduction, consuming H and electrons. It could be described by the following reactions:

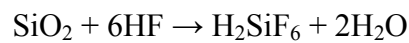
Cathode (Au):



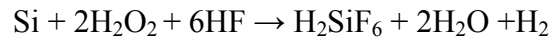


The anode becomes the surface of the Au particle facing the Si and it catalyzes Si oxidation, generating H and e⁻, which is described as:

Anode (Si):



This results in a potential difference between the cathode and the anode. The overall spontaneous power-generating reaction could be written in the following way:



So the etching process is localized in the regions covered by Au. Thus, the etching of Si under the Au-particle results in its “sinking” into the substrate.

3.1.1 Fabrication of arrays of nanoholes using MaCE

We investigated the use of the MaCE process in creating arrays of nanoholes in Si in a parallel fashion.

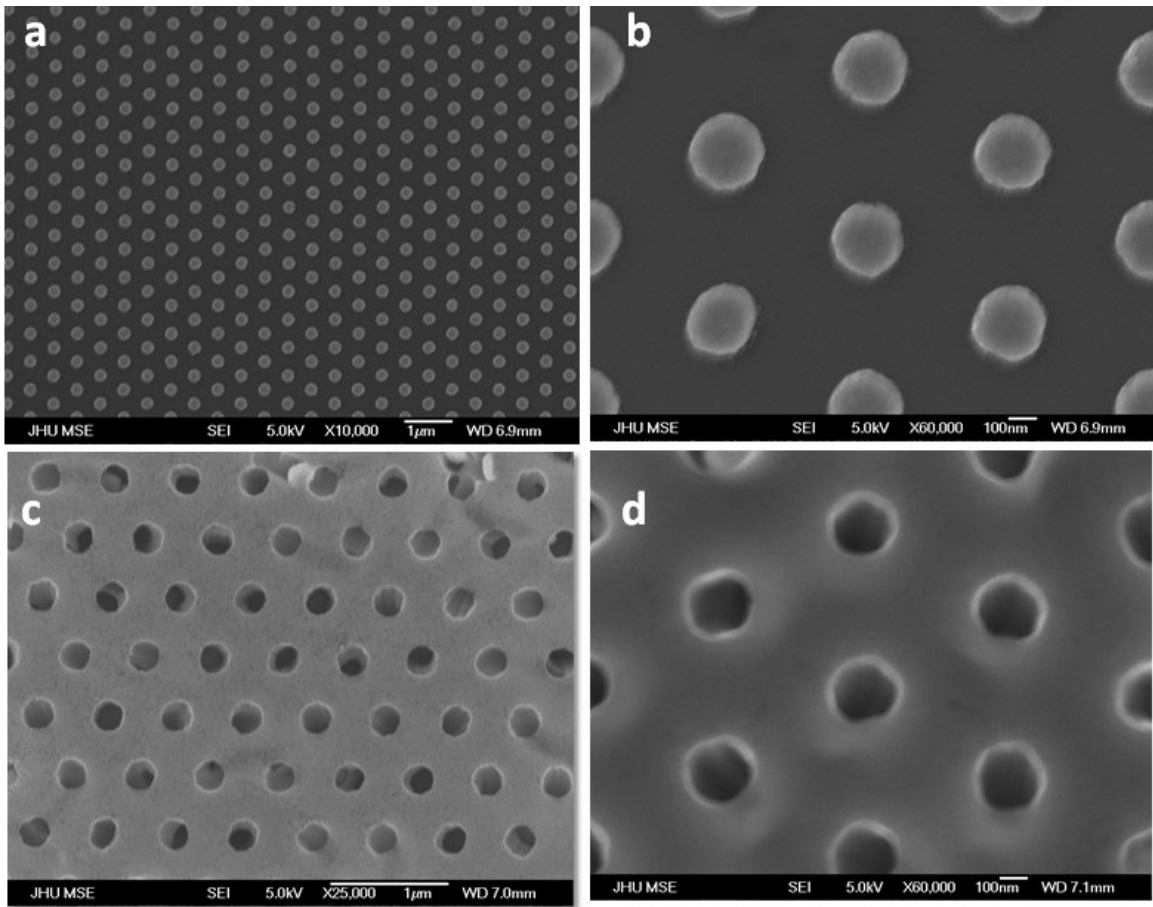


Figure 3.1: Fabrication of nanohole arrays in Si via MaCE using Ag (a and b) shows arrays of nanoimprint lithography patterned circular Au nanopatterns on Si and their magnified images (c and d) arrays of nanoholes and their magnified images after the MaCE process.

Arrays of noble metal (Au or Ag) nanopatterns were lithographically patterned on the Si surface using nanoimprint lithography and the MaCE process was conducted as explained above. Figure 3.1 a and b shows arrays and magnified images of circular gold features patterned using nanoimprint lithography before MaCE process. Fig 3.1 c and d shows the arrays of nanohole patterns and their magnified images formed as a result of the catalytic etching.

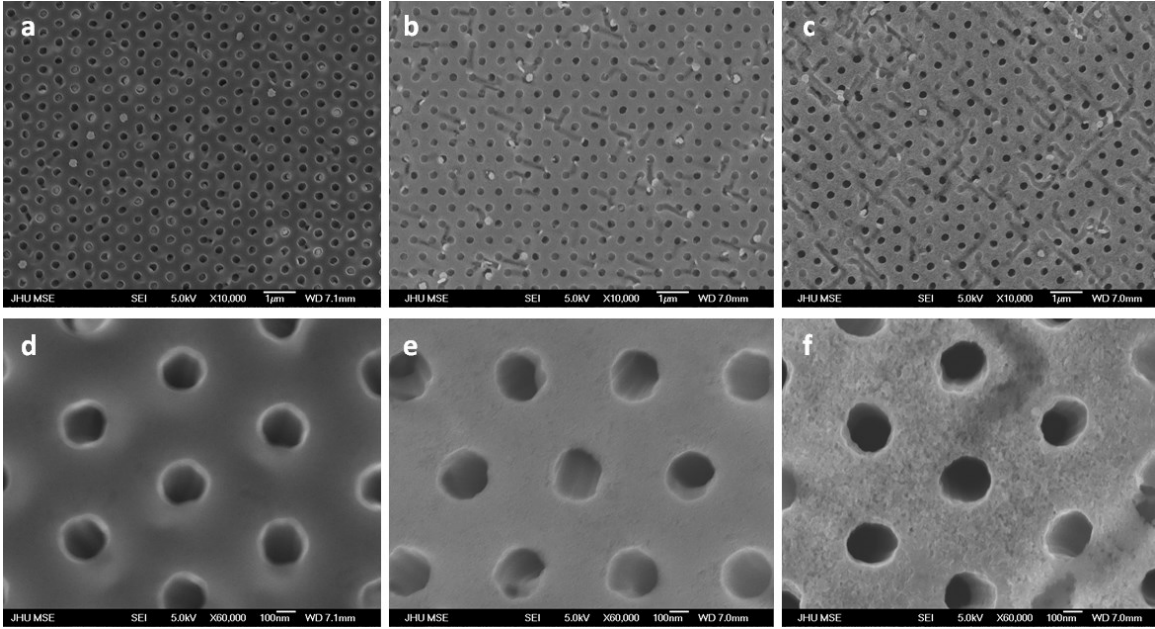


Figure 3.2:MaCE performed for various duration of time (a, b and c) show arrays of nanoholes created in Si as a result of Ag nanopattern assisted MaCE process of 2, 4 and 6 mins. (d ,e, and f) shows the corresponding magnified images.

We also performed MaCE process with Ag nanopatterns with varying duration of etch times. Fig.3.2 shows images of arrays of nanoholes in Si as a result of the MaCE process performed for 2,4 and 6 minutes.

Next, to understand the effect of etching chemistry, we performed MaCE for various concentration of HF in the mixture of the etchant (ρ) as indicated in the formula below.

$$\rho = \frac{[\text{HF}]}{[\text{HF}] + [\text{H}_2\text{O}_2]}$$

Figure 3.3 shows nanopatterns generated as a result of the MaCE process with percentage ρ values of 90, 60 and 40.

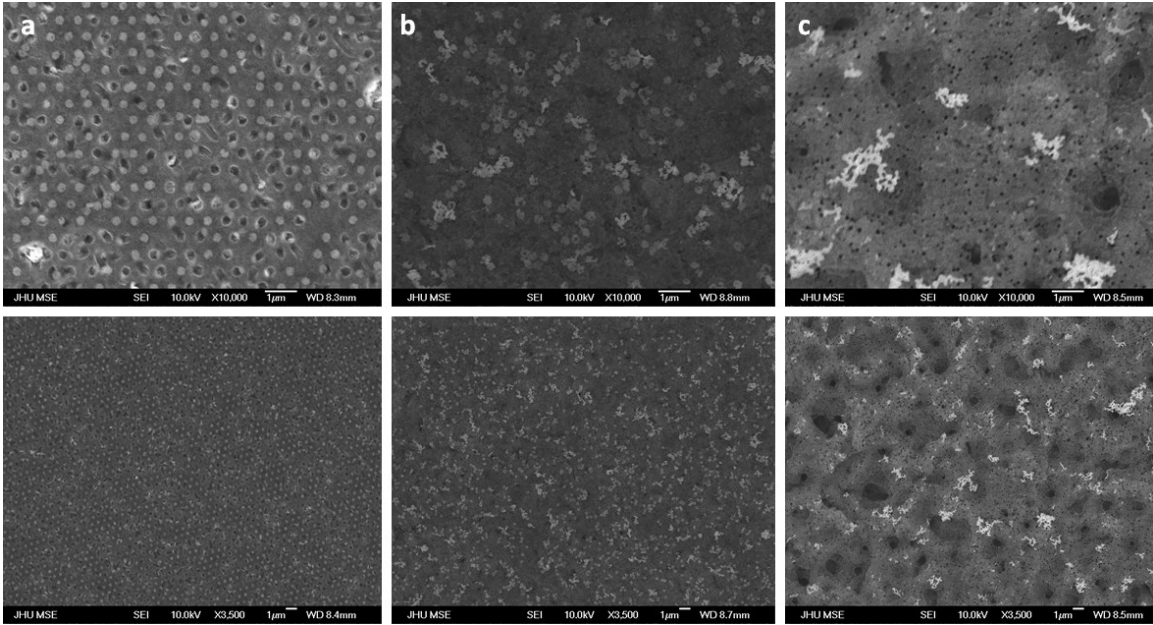


Figure 3.3: Effect of HF concentration in the MaCE etchant. (a, b and c) show arrays (bottom) and magnified images (top) of nanoholes created in Si as a result of Ag nanopattern assisted MaCE process with percentage ρ values of 90, 60 and 40.

3.2 Metal Assisted Plasma Etching (MaPE) of Si

In our studies, we found that gold nanostructures on silicon during plasma assisted dry etching using a gaseous mixture of carbon tetrafluoride (CF₄) and oxygen (O₂) resulted in various recessed structures in the silicon substrate. This section details our work in understanding the theory behind the formation of the structures by first taking a closer look at the plasma etching of process of silicon with CF₄/O₂ gas in detail.

Plasma itself means ionized gas; it's also considered as a distinct fourth state of matter. When a gas is "Ionized" it means that at least one electron is not bound to an atom or molecule. Therefore these free electric charges – electrons and ions – make

plasma electrically conductive-sometimes more than gold and copper, internally interactive, and strongly responsive to electromagnetic fields.

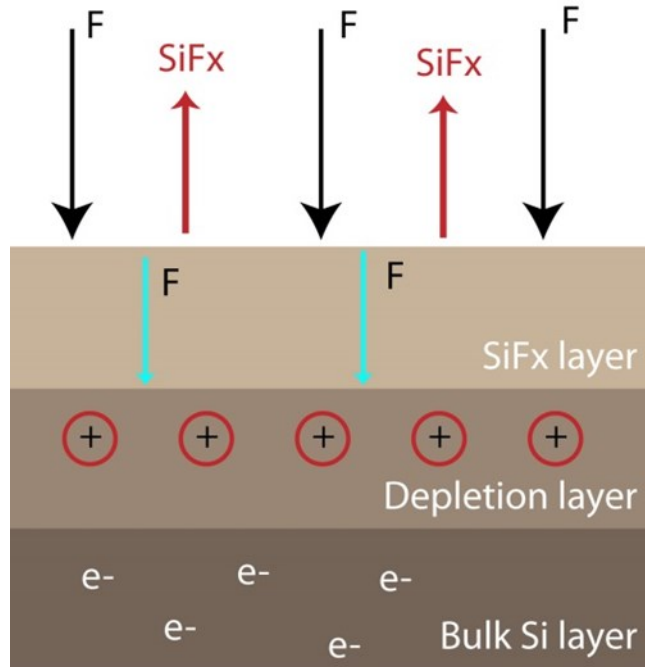
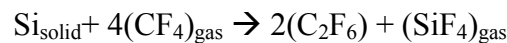
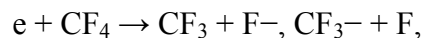


Figure 3.4: Plasma based dry etching process of Si. The image shows reaction pathways occurring during plasma etching of Si.

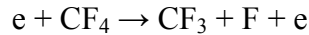
During plasma etching of Silicon with CF₄/O₂ gas mixture, various processes take place within the etching environment (Fig.3.4). Plasma etching of Si with CF₄ discharge can be summarized as



It is known that plasma etching with a CF₄/O₂ gas mixture results in the formation of reactive fluorine radicals (F*)⁵⁷ which are responsible for Si etching. The etching process is determined by F atoms created by dissociative attachment



and by CF₄ molecule dissociation



Formation of F atoms also takes place due to dissociative ionization of CF₄ molecules



The concentration of these radicals has been observed to increase in the presence of Au, silver and few other metals.⁵⁸⁻⁶⁰ Thus, CF₄/O₂ dissociates into CF₃*, F*, O* and few CF₂*. These etch active species is responsible for the etching of silicon. It has been found that Au reacts with the active species generated in the plasma discharge and the resulting compounds have high vapor pressure. It has also been found that Au oxides/compound maybe the catalyst and this accelerates the reaction of CF_x* and F* with Si. Once the F atoms reach the surface, the depletion layer forms and as a result, they become protonated making Si in the protonated state to be more susceptible to the active species. Gold has also been reported to increase this depletion layer thus making the Si underneath it more susceptible to etching. The etch rate is also dependent on a number of parameters such as RF power, which results in an increase in the number of CF_x radicals and the ion energy flux which appears to control this mechanism. In addition, the etch rate is also dependent on the process pressure due to the enhanced chemical reaction in the etching species. Also, the etch rate have seen to be affected by the relative changes in the atomic F and atomic O concentration in the gas phase as the oxygen percentage of CF₄/O₂ is increased.

The CF_x radicals also play an important role in anisotropic etching, forming protective films on the treated surfaces. An important surface kinetic feature of the CF_x radicals is their ability to dissociate on active surfaces, including silicon and the layer of intermediate silicon fluorides, SiF_x . This surface dissociation with formation of chemisorbed carbon atoms leads to a buildup of carbon or polymer film on the surface. Increasing the power and pressure of the process results in increased ion energy driven F-atom etching of Si mechanism and this ion bombardment causes chemical reaction that results in etch products that can be desorbed from the surface. In this case, the energetic ions destroy the Si-Si and Si-F bonds of the SiF_x layer and forms groups such as SiF_4 and SiF_2 which are weakly bound to the surface⁶¹. Thus they are easily thermally desorbed resulting in etching. In addition, these ion bombardments also results in the formation of damaged surface regions (such as lattice damage) which makes them more reactive to fluorine. Further, this also leads to a temperature increase which also results in accelerated etching^{61,62}.

Although, MaCE and MaPE processes share some similarities in terms of the processes, there are some unique features for the MaPE process that makes it well suited for the creation of nanopatterned surfaces in Si. One of the major difference is that Au does not deplete in wet etching⁵⁶ and hence behaves as a true catalyst, whereas we observe a depletion of Au MaPE. The other key difference is that the proposed wet etching mechanism is of an electrochemical nature, since the noble metal catalysts serve as galvanic cells short circuiting the peroxide electron transfer mechanism to Si, leading to Si destabilization and rapid etching.⁶³ In terms of the final structure formed by MaCE process, Si dissolution can either take place in its very near vicinity (regions within a few

nanometers) of the Au or in a wide area (hundreds of nanometers) around Au creating conical holes depending on the wet etchant composition.⁶⁴ However, as compared to our process, the MaCE etched structures formed are not coated with Au, the catalyst is not depleted and no nanoparticles are observed.

3.2.1 Fabrication of Arrays of nanopatterned features in Si using MaPE

In comparison to the MaCE process the MaPE process that we discovered offers more versatility in terms of controlling the nanostructure geometry, pore angle and etch rate by tuning the plasma chemistry, time and power used for etching. Therefore, we investigated further in to the utilization of this process to enable patterning of nanoscale geometries in Si. Figure 3.5 shows arrays of nanoholes created in Si using the MaPE process performed for various duration of times.

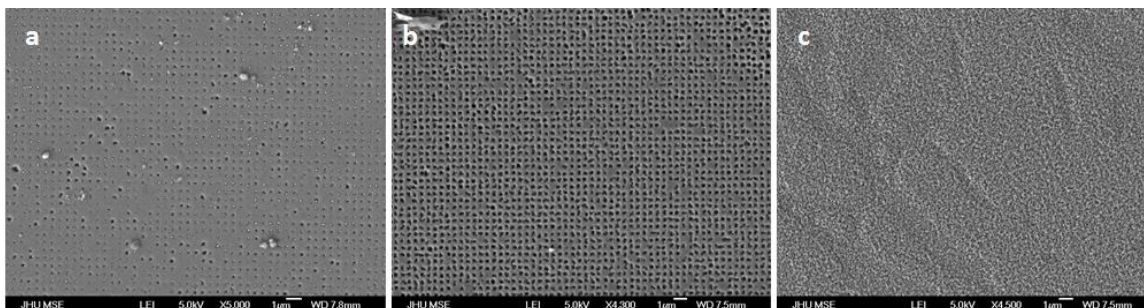


Figure 3.5. MaPE based creation of nanopores in silicon: nanopores formed as a result of MaPE process performed for 4 mins (a), 6 mins (b) and 8 mins (c).

Further, we investigated the ability to control the pore diameter by varying the etching power. Figure 3.6 shows the formation of pore geometries with varying cone angles and mouth diameters formed as result of varying the etching power in the MaPE process. This versatility in the MaPE process is further exploited to engineer patterned

nanopores, channels and microwells as described the section below. Additionally, we also utilized this process to create conical nanopores in semiconducting substrates of Si and this work is described in detail in Chapter 4.

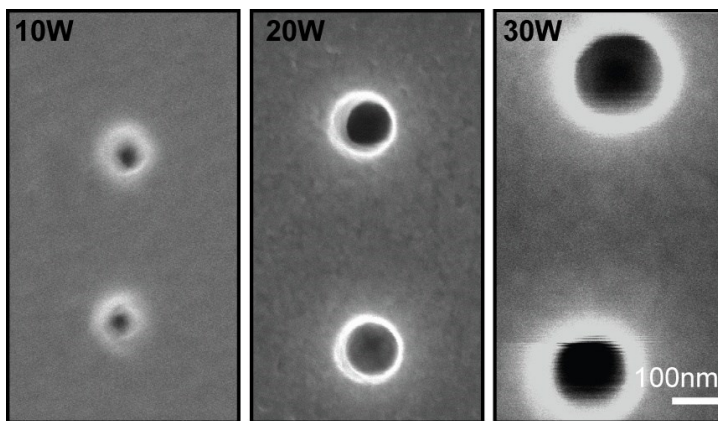


Figure 3.6 Variation of Power in MaPE process: nanopores formed as a result of MaPE process with etching powers of 10W (left), 20W (middle) and 30W (right).

3.3 Creation of Silicon nanostructures with AuNP Coating using MaPE

The selective patterning of biomolecules within well-defined microstructures such as microwells and channels is important for bioanalytical microdevices^{65,66}. Spatially separated recessed microstructures can physically isolate biomolecules from each other, thereby enabling bioprocesses to be carried out within a confined geometry and with minimal cross-contamination.^{67,68} Further, the selective chemical modification of surfaces is required to enable binding of biomolecules within these structures while retaining their bioactivity. Gold (Au) and silicon (Si) are two of the most commonly used materials for surface patterning due to their differential ability to bind thiol and silane based molecules respectively^{69,70}. Hence, Au and Si surfaces can readily be functionalized with different biomolecules. Si surfaces decorated with Au NPs provide a

favorable platform for protein patterning and bioanalytical assays as the NPs offer a large surface area for binding of molecules. Au NPs also provide novel electromagnetic responses such as a size dependent plasmon frequency and field enhancement⁷¹⁻⁷³.

Moreover, in some applications, it has been suggested that NPs can increase the binding affinity of proteins as compared to uncoated surfaces, since the protein molecules can assume a wider range of orientations on NPs⁷⁴. Although microstructures containing NPs have been demonstrated previously^{75,76}, multiple fabrication steps were needed and the deposition of NPs within them required an external electrochemical setup. Additionally, it is challenging to get a uniform coating of Au NPs due to their tendency to aggregate. Here, we demonstrate a relatively straightforward strategy to construct Si structures such as microwells and channels that have a uniform coating of Au NPs. These NP coated structures were formed spontaneously during plasma assisted dry etching of Si substrates which were patterned with Au using a gaseous mixture of carbon tetrafluoride (CF₄) and oxygen (O₂). We investigate the mechanism of formation and explore the utility of these recessed structures in biomolecular patterning, specifically, in the assembly of antibodies within the structures.

3.3.1 Fabrication Process

Au patterns on Si were formed by lift-off metallization. Briefly, Si wafers [<100>, p-type] were cleaned and rectangular and circular resist patterns were defined using either photolithography or ebeam lithography. Photolithography was performed with 2µm thick Shipley 1827 photoresist using an ultra µline series Quintel mask aligner. For E-beam lithography, 100 nm of an electron-beam (e-beam) resist, poly(methylmethacrylate) (PMMA, MW 950K A2) was spin coated and the wafer was baked at 185 °C for 3

minutes. An e-beam controlled by a RAITH system (Quantum v4.0) was used to pattern the resist and the resist was developed using an MIBK developer (1:3 = MIBK: IPA) for 35 seconds.

After resist patterning, a 0.2nm of chromium adhesion layer and the desired thickness of Au (10-100nm) were deposited by thermal evaporation at a pressure of approximately 10^{-5} Torr followed by lift-off in acetone. All thickness were measured in situ during thermal evaporation using a quartz crystal thickness monitor. Au NP coated Si structures formed spontaneously during plasma etching of the substrates using a radio-frequency (RF) plasma of 25W at 13.56MHz (Technics PEII-A) with etch gases, O₂ at a flow rate of 3.6 sccm and CF₄ at a rate of 14 sccm.

3.3.2 Au NP size characterization

SEM images of the microwell surface were taken using JEOL JSM-6700F cold cathode field emission SEM. The backscatter detector was used to take the images with the NPs having brighter intensity corresponding to the larger atomic mass of Au. The images were first image processed to set the calibration scale. The distance of the line was calculated in pixels and the scaling factor in pixels/ μm was determined by the known value of distance in μm . The images were converted to 8 bit gray scale mode and the thresholding of the images were done visually such that the nanoparticles appeared in red and the background in white. Once all the nanoparticles were within the threshold range, each image was processed into binary images for analyzing the particles. The particle analysis function in Image J yielded the outlines of detected nanoparticles that were counted and analyzed using the software.

3.3.4 Antibody assembly within the microwells

Au NP coated Si microwell substrates were immersed in solutions containing 0.1 mM nitrilotriacetic acid-terminated tetra (ethylene glycol) undecane thiol (NTA thiol, Prochimia) in ethanol for 16 h. The substrates were cleaned with ethanol, dried with compressed N₂ and immersed in a 0.1 M solution of Nickel (II) chloride (NiCl₂) for 30 minutes and rinsed with deionized water to remove any unbound NiCl₂. Subsequently, the substrates were immersed in 1 μM histidine tagged protein G (Abcam) containing 1 % bovine serum albumin (BSA) in phosphate buffered saline (PBS) for 2 hours and rinsed with PBS to removed unbound protein G. Finally, the substrates were immersed in 0.5 μM FITC labeled rabbit anti- Escherichia coli IgG (AbD Serotec) containing 1 % BSA in PBS for 2 hours and rinsed again in PBS to remove unbound antibodies and analyzed.

3.4 Results and Discussion

3.4.1 Au NP coated Si microwells

It might be expected that the Au would serve as an etch mask reducing etching under the Au pattern resulting in a mound or undercut structure. However, we observed that the etching rate of Si was accelerated in the immediate vicinity of the Au patterns resulting in the formation of Au NP coated microwells (Fig. 3.7). There are certain noteworthy characteristics of this process. From SEM images, we observed that the shape of the microwell resembled the shape of the original Au pattern indicating isotropic etch acceleration. We also observed that the size of the Au patterns decreased during etching, indicating that Au was depleted from the pattern during microwell formation (Fig. 3.7d). Zoomed-in SEM images revealed that, while Au was depleted from the pattern, a uniform

coating of NPs was being formed along the sidewalls of the microwells (Fig. 3.7e). Compositional Energy Dispersive X-ray Spectroscopy (EDS) mapping revealed that these NPs were composed of Au. Image analysis revealed that the majority of the NPs had diameters ranging from 20-30nm and the number density of the NPs was approximately $1.03 \times 10^{14}/\text{m}^2$ (Fig 3.7f).

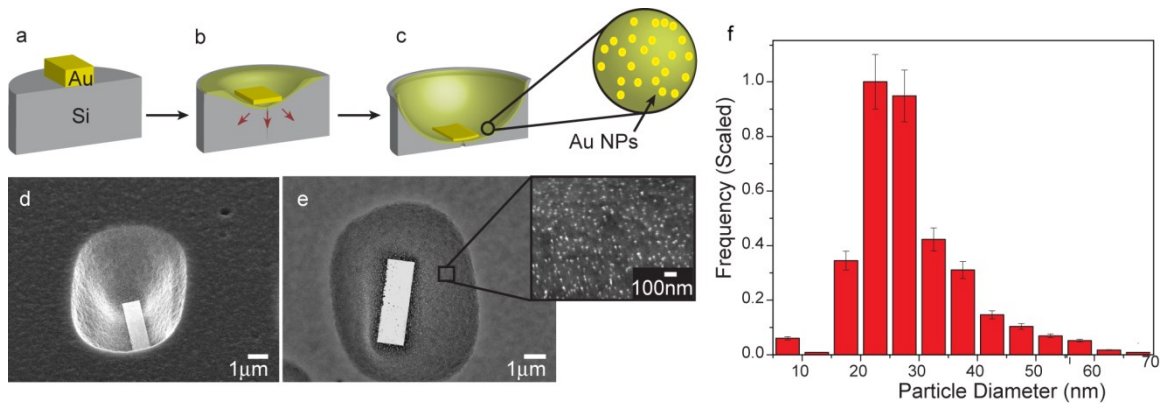


Figure 3.7 Spontaneous formation of Au NP coated Si microwells during plasma etching. (a-c) Conceptual schematic of the proposed mechanism showing depletion of Au patterns during etching which is accompanied by dissolution of Au in Si followed by Au NP precipitation. (d-e) SEM images using a (d) secondary electron and (e) backscatter detector. Since Au has a higher atomic mass as compared to Si, the NPs appear brighter and are clearly visible in the backscatter image (f) Size distribution of the NPs along the side walls of the microwells; particles are predominantly 20-30 nm in diameter.

3.4.2 Proposed mechanism

Based on our observations we propose the following mechanism for spontaneous Au NP coated well formation. It is known that plasma etching with a CF_4/O_2 gas mixture results in the formation of reactive fluorine radicals (F^*)⁵⁷ which are responsible for Si etching.

The concentration of these radicals has been observed to increase in the presence of metals such as Au, silver, copper and aluminum⁵⁸⁻⁶⁰. In our experiments, we believe that this increase in reactive radicals leads to the accelerated etching rate of Si in the vicinity of the Au patterns leading to the formation of microwells.

Further, this enhanced etching is accompanied by a local rise in temperature favoring the formation of Au-Si eutectic mixture^{77,78}. As the reaction proceeds, Au diffuses and dissolves into the Si forming a eutectic phase within a few atomic layers beneath the Si surface⁷⁹. An excess of Au is needed to form the Au-Si eutectic and this provides a driving force for Au to diffuse away from the pattern thereby reducing the size of the pattern. On super saturation of Au in the eutectic, it precipitates in the form of NPs⁸⁰ (Fig. 3.7e inset).

3.4.3 Influence of etch time

We observed that the size of our plasma etched microwells increased with increasing etch time (Fig. 3.8 a-b) and eventually Au was completely depleted from the pattern (Fig. 3.8 c). We also observed the formation of a ridge like structure between adjacent microwells in high density Au patterns, which limited further lateral growth of the microwells (Fig. 3.8 c).

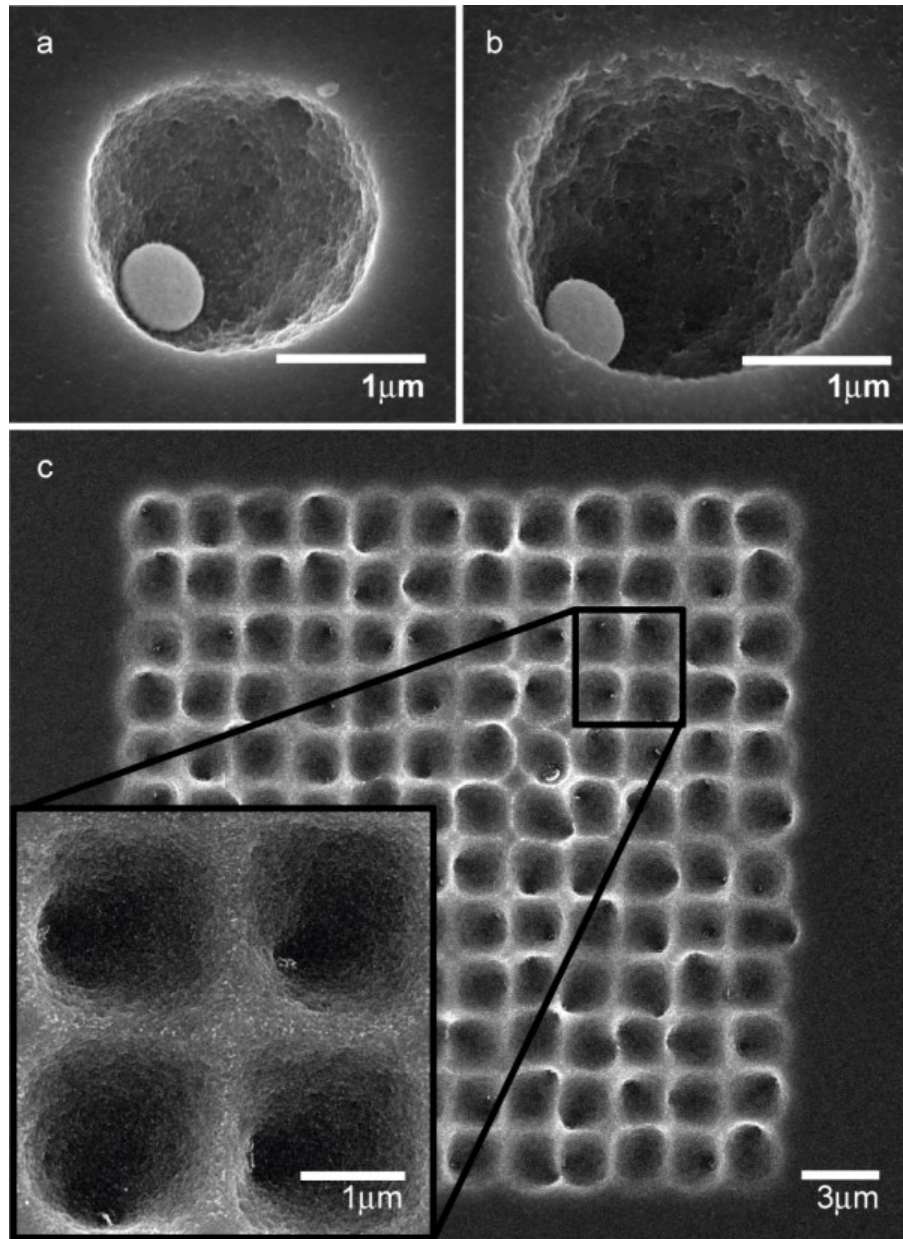


Figure 3.8 SEM images of Si microwells formed at different etch times of (a) 100s and (b) 160s. The same Au circular pattern with a 600 nm diameter was used in both cases but increasing etch times resulted in a larger and deeper microwell. Both images have the same scale bar to enable an easy visual comparison. (c) When dense Au patterns were used, lateral growth of microwells was self-limited as ridges formed between adjacent wells.

3.4.3 Influence of pattern geometry

Varying the size of the Au patterns were seen to effect the size of the microwells formed. It was found that decreasing the size of the circular patterns resulted in vertically shaped microwells with less or no nanoparticle coating along its sidewalls (Fig 3.9). We rationalize this observation by noting that a smaller amount of Au present within the wells results in reduced nucleation and supersaturation along the edges of the microwells. Consequently, an increase in the particle density was seen as the the size of the circular patterns are increased.

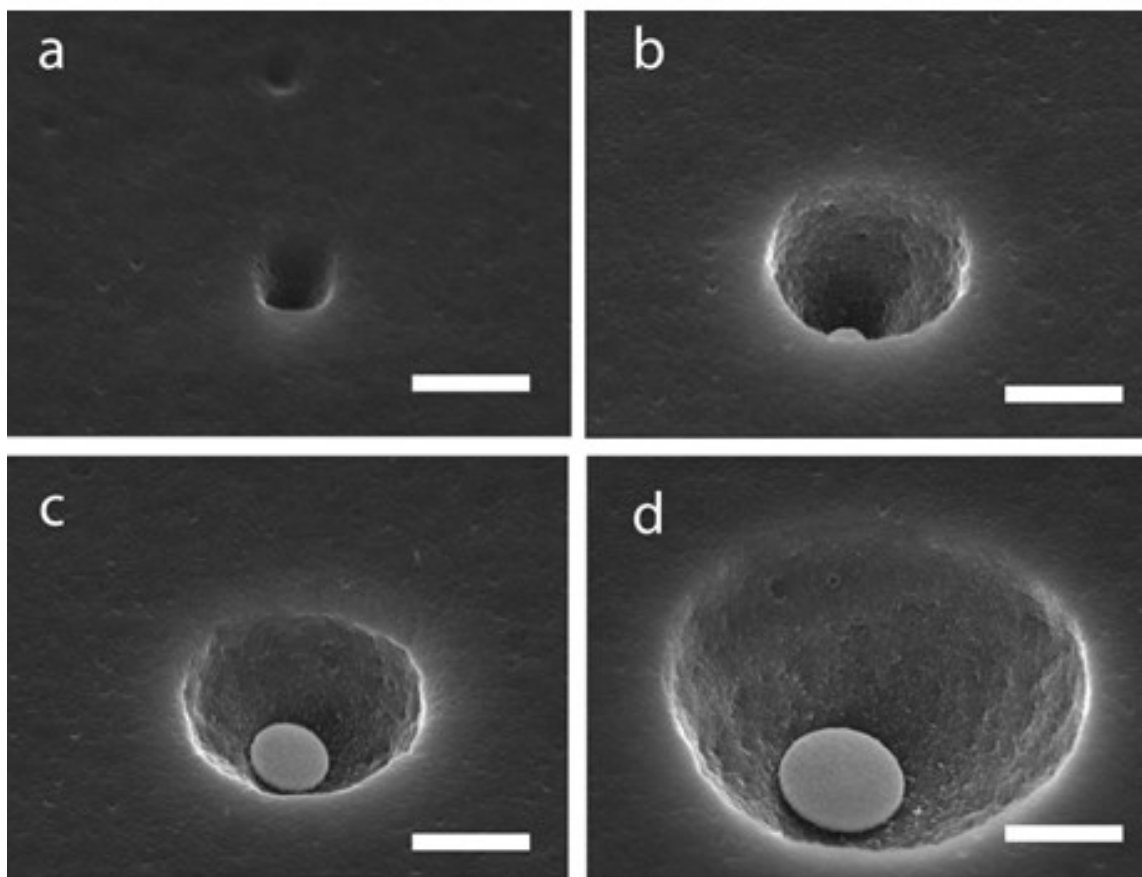


Figure 3.9: Microwell size can be varied by using Au patterns of different sizes. Pattern sizes are a) 50nm b) 100nm c) 600nm and d) 1 μ m. Scale bar 1 μ m

We systematically varied the shape of 50 nm thick Au patterns with identical lateral surface areas. Specifically, rectangular patterns with varying length to width ratios were patterned. This ratio was varied from 50 to 1 (Fig. 3.10a-f); all substrates were processed and etched simultaneously for a period of 100s. Plasma etching of the Au rectangular patterns produced similarly shaped Si microwells. We observed that the Au patterns moved around within the wells during etching, indicating mechanical perturbations, possibly due to convective forces. The Au patterns were seen to move down into the well as etching continued. We observed more etching at the base of the microwell as the Au pattern depleted and sunk down during continued etching. It is also noteworthy that the corners of the wells became rounded during etching.

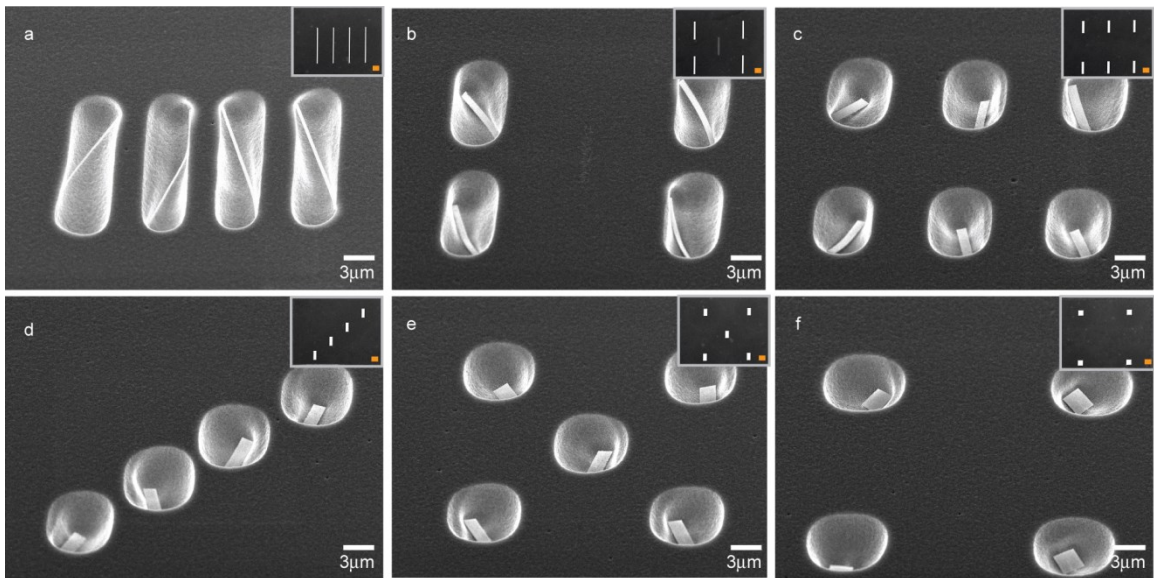


Figure 3.10 SEM images of Si microwells formed by plasma etching of Au patterns with varying shapes. All patterns (shown in the insets) were composed of rectangles; each rectangle had an identical surface area of $4.5 \mu\text{m}^2$ but a varying length to width ratio of (a) 50, (b) 9.8, (c) 5.5, (d) 3.2, (e) 1.8 and (f) 1. We observe that the shape of the microwell resembled that of the original Au pattern suggesting an isotropic etch.

3.4.5 Au NP coated microchannels

Apart from microwells, this methodology could also be used to create long, Au NP coated Si microchannels (Fig. 3.11). Here, approximately 16 μm wide and several mm long Au patterns (50 nm thick) were first deposited and etched to form approximately 65 μm wide channels after plasma etching for 45 min (Fig. 3.11 inset b).

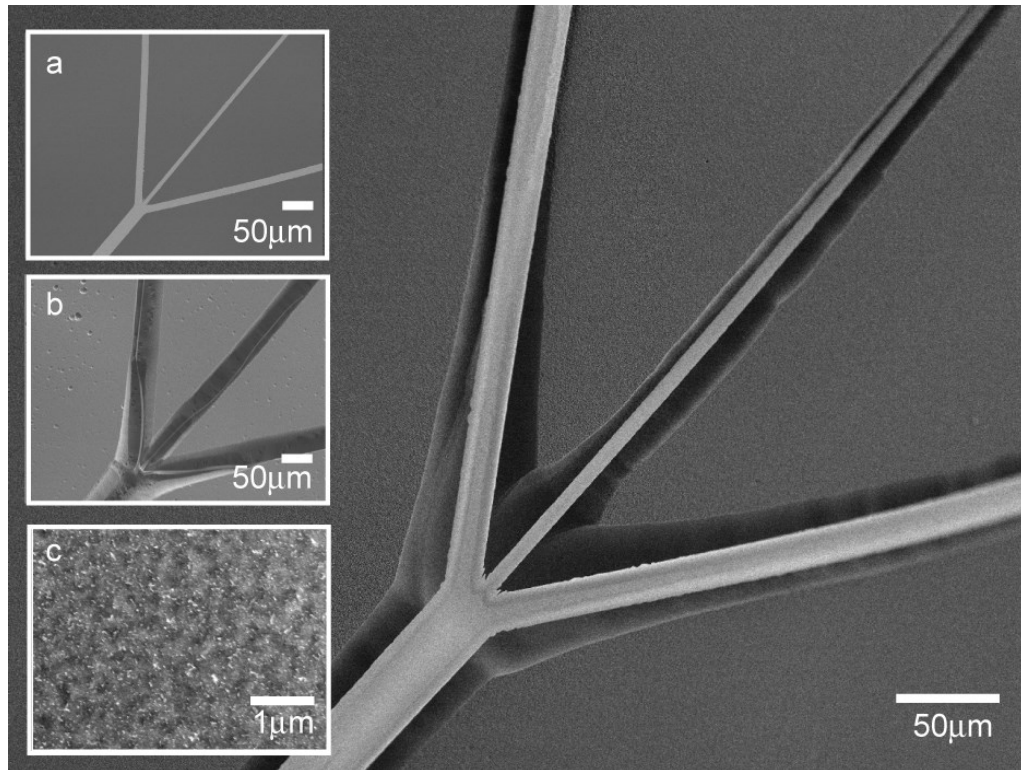


Figure 3.11 SEM image of a Au NP coated microchannel after etching approximately 16 μm wide and several mm long Au patterns (50 nm thick) for a period of 10 minutes. The SEM insets show (a) the pattern as deposited, before etching (b) the channel after 45 min of etching and (c) a zoomed-in image showing Au NPs within the microfluidic channel.

At shorter etch times of 10 mins, residual Au patterns were clearly observed within the microfluidic structures (Fig. 3.11). These residual Au patterns could be removed by ultrasonication to obtain predominantly Au NP coated channels (Fig 3.12).

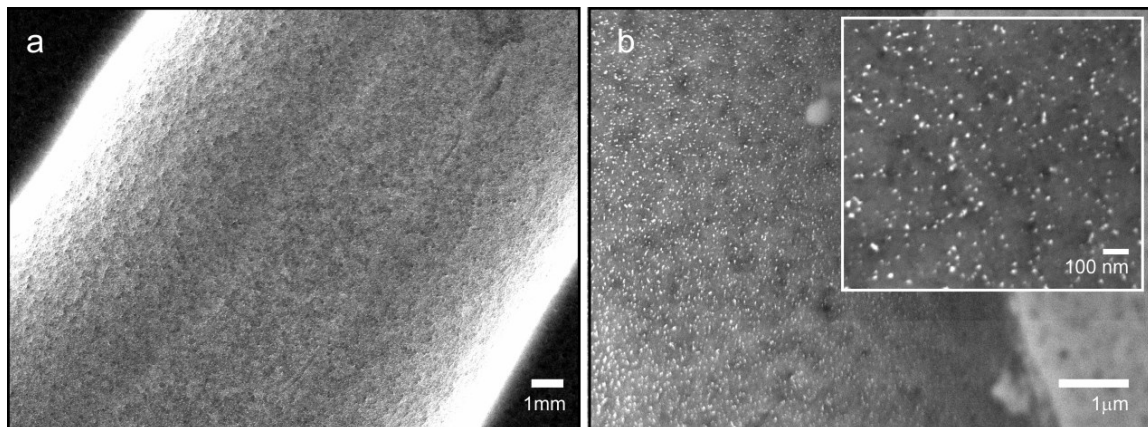


Figure 3.12 Sonication of the microchannel structure results in the removal of the solid Au film but not the Au NPs around the sidewalls. a) SEM image in secondary mode showing the Au pattern in Fig 5b removed from the channel b) SEM image in back scatter mode along the channel side wall showing that while the large Au structure was removed, the smaller NPs remained along the sidewalls. Inset showing an SEM image in back scatter mode showing a closer view of the NPs.

3.4.6 Antibody assembly within the microwells

We show the utility of Au NP coated Si microwells in biomolecular patterning by assembling fluorescently (FITC) labeled antibodies within the microwells. The patterning scheme resulted in antibodies (anti- *E. coli* IgG) being bound preferentially to the Au NPs within the wells (Fig. 3.13). Fluorescence intensity line scans show highest levels of antibody binding on the residual Au patterns, moderate binding along the NP coated microwell side walls and relatively low, non-specific binding on the Si substrates. The

Au NP coated microwells, therefore, can be used for patterning biomolecules such as protein G and antibodies and can, in principle, be used in ELISAs and related applications for the detection of antibodies and antigens.

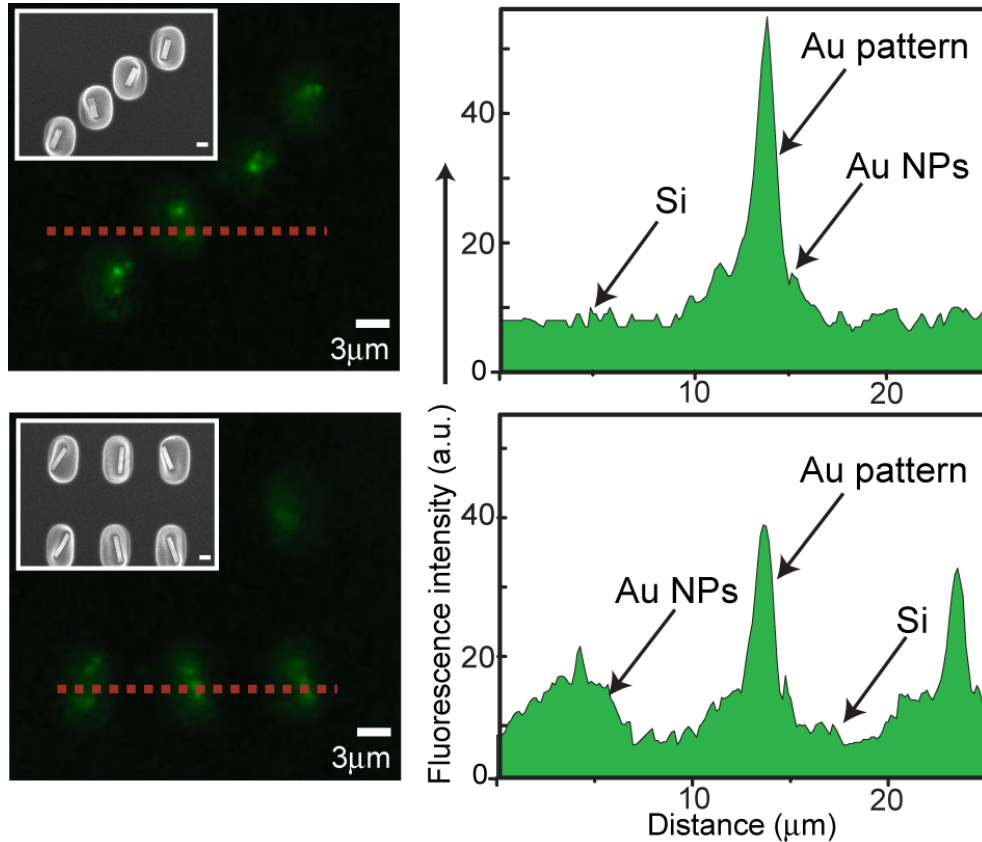


Figure 3.13 Spatial assembly of antibodies within the Au NP decorated Si microwells. SEM images of the microwells (inset, scale bar 3 μm) and optical fluorescent images after antibody assembly (left panel). The graphs in the right panel show the corresponding fluorescence intensity measured along the red dotted lines in the left panel.

3.5 Conclusions

In this chapter we described the use of the MaPE technique as a one-step plasma etching process that can be used to form Au NP coated Si recessed microstructures. We

demonstrated that these Au NP decorated recessed microstructures can be used for selective biomolecular patterning enabling biochemical reactions to be carried out in these microenvironments. While we demonstrated a use of this technique for selective antibody assembly, it can also be adapted to immobilize other proteins or molecules of interest. Hence, this simple one step approach is amenable to the creation of a range of Au NP coated recessed structures of utility in bioanalytical chemistry. While it could be argued that NP coated microwells can be fabricated by merely dispersing Au NPs on the substrate, it should be noted that it is challenging to create a relatively uniform dispersion of NPs on a substrate due to the tendency of the NPs to clump together. Moreover, selective functionalization of NPs within only the interior surfaces of microwells and microchannels would require additional lithographic processes.

CHAPTER 4

Semiconducting Conical Nanopores by Metal Assisted Plasma Etching (MaPE)[§]

Solid-state nanopores have attracted a great deal of scientific interest due to their possible use in replicating some behaviors observed in naturally occurring trans-membrane protein channels¹⁻³. In order to mimic the complex chemo-electrical control that is observed in protein channels^{4, 5}, there is a need to incorporate mechanisms for active control of ion transport through solid state nanopores^{6, 7}. Nanopores formed in semiconducting substrates such as silicon (Si) offer the possibility for voltage-gated control of transmembrane ionic and molecular transport^{8, 9}. Furthermore, nanopores in Si membranes are mechanically robust, biocompatible, able to tolerate a wide variety of environmental conditions and permit facile integration with existing Si-based electronic and micromechanical devices¹⁰. When considering the effect of geometry on nanopore transport characteristics, conical nanopores have been found to exhibit unique ion transport properties as a consequence of their asymmetric geometry¹¹. For example, the ionic rectification behavior observed in conical nanopores, due to surface charge density asymmetry¹², can be utilized to develop ionic analogs of electronic devices^{13, 14}. Further, for nanopores of conical geometry exhibit lower electrical resistance in comparison to those with cylindrical geometries of the same tip diameter, making them more suitable

[§] The work reported in this chapter is reproduced with permission from : Teena James, Yevgeniy V. Kalinin, Chih-Chieh Chan, Jatinder S. Randhawa, Mikhail Gaevski, and David H. Gracias Nano Letters 2012 12 (7), 3437-3442. Copyright 2012 American Chemical Society <http://pubs.acs.org/doi/abs/10.1021/nl300673r>

for molecular sensing applications, as these pores generate higher ionic currents¹⁵. Hence, conical nanopores in semiconducting substrates are attractive for a wide range of applications including the creation of synthetic analogues of biological nanochannels¹⁶, ionic logic circuitry^{17, 18} and actively controllable molecular separation platforms¹⁹. However, the generation of conical nanopores in single crystal Si, to enable gated, active control, is challenging using existing methodologies.

4.1 Introduction

There exist a variety of methods to create nanopores. These include the widely utilized track etching method, which enables the creation of conical nanopores in polymeric thin films through ion bombardment and subsequent chemical etching¹². However, this method is restricted to homogenous dielectrics and also requires the use of MeV to GeV ion sources²⁰. Although wet chemical etching of e-beam lithography patterned Si has been used to form nanopores, it offers limited control over the pore geometry in terms of cone angles and often results in faceted pores due to the varying etch rates along the different Si crystallographic planes²¹⁻²⁴. Here, we describe the process of nanopore formation in Si substrates, that relies on an enhancement of the dry etch rate observed in the presence of Au nanoparticles (NPs)²⁵. The process can be implemented in a maskless manner and does not require lithographic patterning. Further, the etch process allows considerable control over pore geometry and the application of a voltage to nanoporous Si membranes enables active control over small ion and protein transport.

We discovered that CF₄-O₂ plasma etching of single crystal Si substrates in the vicinity of Au NPs resulted in a conical etch profile (Figure 4.1).

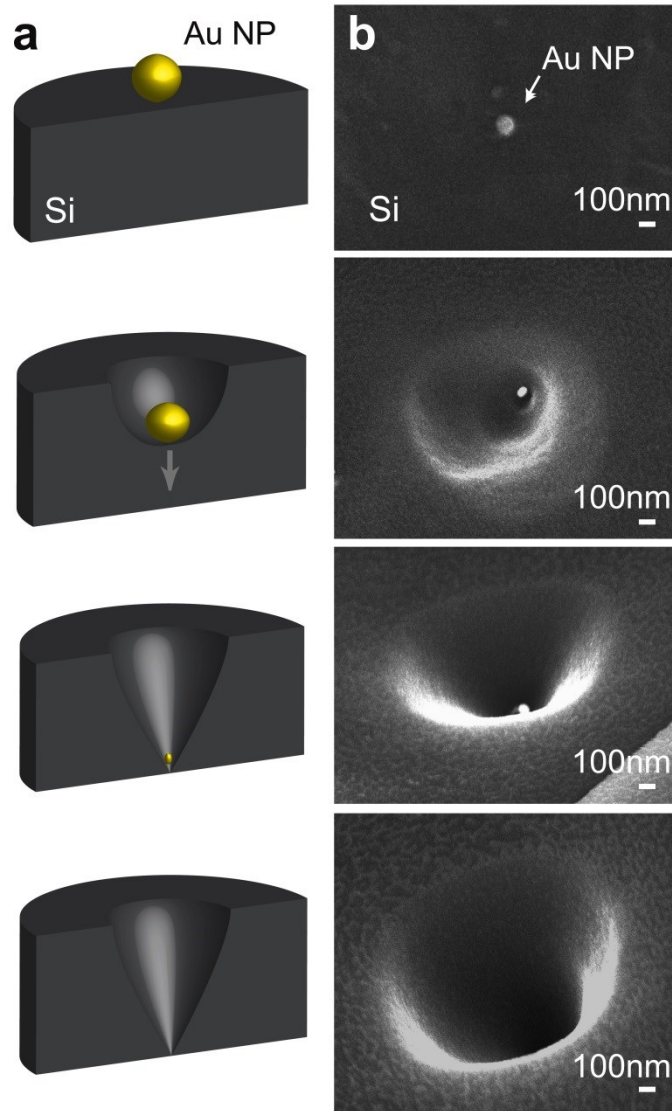


Figure 4.1. Schematic illustration and corresponding SEM images of conical nanopore formation during plasma etching of a Si substrate in the vicinity of an Au NP. (a) Schematic illustration of the process. (b) SEM image of an Au NP on the Si surface before etching and at different times during the plasma etching process.

In order to characterize the process, we utilized silicon on insulator (SOI) wafers with different Si device layer thicknesses. We dispersed Au NPs on the surface of the Si device layer; plasma etched and released the Si membranes by dissolving the buried

oxide layer in hydrofluoric acid (HF) (Figure 4.2a). It is also noteworthy that this process is versatile in that Au NPs can also be dispersed on flexible Si membranes or Si powder crystals so that such conical nanopores can be formed on these substrates (Figure 4.2b-d). While dispersal of NPs can be used to form conical nanopores in a lithography-free manner, our process is also compatible with lithographically defined Au patterns which may be required in applications that require precise positioning or ordered arrays of nanopores. We were able to utilize both e-beam lithography to pattern individual Au discs which could be plasma etched to form precisely positioned isolated nanopores as well as nanoimprint lithography (NIL) to define arrays of Au nano-discs (Figure 4.2e), which could also be plasma etched to create large-area ordered nanopore arrays on Si membranes (Figure 4.2f).

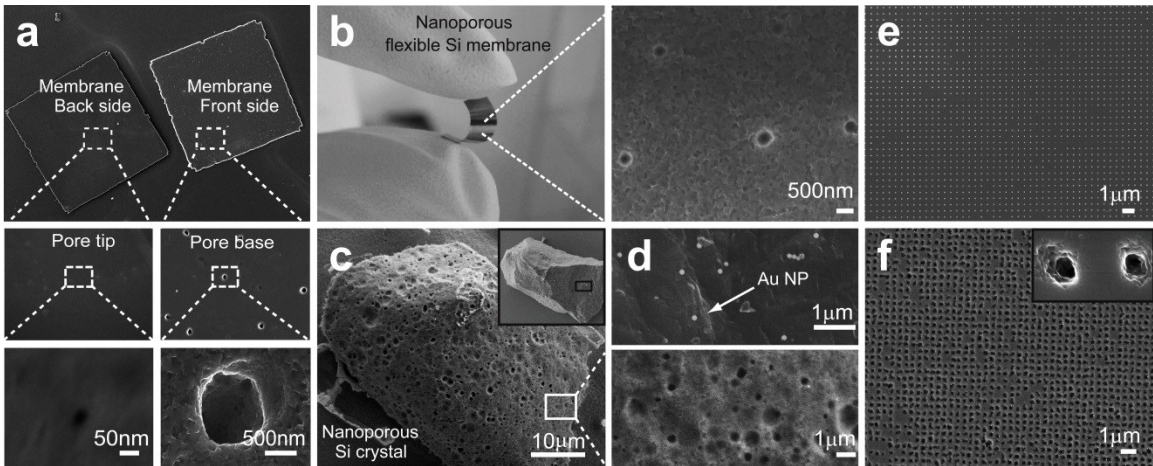


Figure 4.2: Versatility of conical nanopore formation in different Si substrates. (a) SEM images of nanoporous Si membranes (500 μm square) at different magnifications showing back-side (pore tip) and front-side (pore base). (b) Optical image of a large-area Si nanoporous membrane with nanopores evident in the SEM image (right panel) of the membrane surface. (c) Zoomed-in SEM images of a nanoporous Si crystal formed by our

etching process; inset shows a Si crystal with dispersed Au NPs before etching. (d) Zoomed-in SEM image of the Si surface dispersed with Au NPs before etching. (e-f) SEM images of an array of gold nanodiscs patterned using nanoimprint lithography (e) before and (f) after etching; the zoomed-in image of the nanopores are shown in the inset.

In order to optimize the etching conditions, we first explored the effects of varying CF_4/O_2 ratio on bare Si wafers and observed that a ratio of 25 sccm CF_4 and 4 sccm O_2 resulted in optimum etching (Supplementary Table S1).

4.1.1 Dependence of Si etching on CF_4/O_2 ratio

CF_4 (sccm)	O_2 (sccm)	O_2 (%)	Effect on silicon etching
25	0	0	30-50 nm/min
25	4	13.7	~110 nm/min
25	25	50	Fibrous silicon formation

Table 4.1. Variation of Si etching with varying O_2 concentration obtained at RF power 50 W, total pressure 0.5 Torr and etching time 3 mins. This etch characterization was done on bare Si wafers using a Technics PE-II-A etcher.

Further, we estimate that the Au NPs enhance the etch rate of Si by over a factor of ten, with measured increases in Si etch rate from ~110 nm/min to about ~4000 nm/min, and the etch rate was sensitive to the type of etcher used and the density of the nanoparticles. It is noteworthy that similar enhancements in wet etching rates of Si have been observed using a metal assisted chemical etching (MaCE) process^{26,27}. In the MaCE process, the Si substrate with a noble metal mask is wet etched with hydrofluoric acid (HF) and an

oxidative agent, typically hydrogen peroxide (H₂O₂). During etching, the Si beneath the noble metal is etched much faster than the uncovered Si, which is similar to our observation here. The enhanced etching of Si at the Si/metal interface has been attributed to preferential reduction of the oxidant at the surface of the noble metal with associated hole injection into the Si^{26, 28}.

In contrast, our mechanism for the formation of conical etch-profiles is based on the accelerated dry etching of Si in the vicinity of Au NPs²⁵. It has been shown that the presence of Au or Au oxide increases the etch rate of Si in CF₄-O₂ plasma²⁹; this acceleration has been attributed to a metal-catalyzed increase in the concentration of reactive fluorine radicals (F*)^{30, 31}. We developed a theoretical model (details in supplementary information) that captures the effects of an enhanced etch rate in the vicinity of the Au NP and predicts a conical etch profile (Figure 3a). From the model, the cone half- angle (θ) can be related to the etch rates and etch anisotropy (k) as,

$$\theta = \arctan \left[\frac{1}{k \sqrt{(v_1/v_0)^2 - 1}} \right] \quad (\text{Equation 1})$$

Experimentally, we varied the etch power and found that higher RF powers generated wider cone angles (Figure 4.4b; AFM characterization results in supplementary information), which we attribute to a decrease in the anisotropy factor k .

4.1.2 Effect of the power variation on conical nanopore geometry

We performed the AFM analysis of the conical nanopores etched in Si using the Technics PE-II-A etcher, under two different experimental conditions, namely 100 W and 25 W of RF power. In our experiments, the gold circular patterns were fabricated using e-beam

lithography and subsequent lift-off metallization as mentioned in the methods section. The images were obtained using Veeco's DI CP-II AFM model. Higher RF powers resulted in the increase of base diameter of the pore as can be seen from the analysis (Figure 4.3).

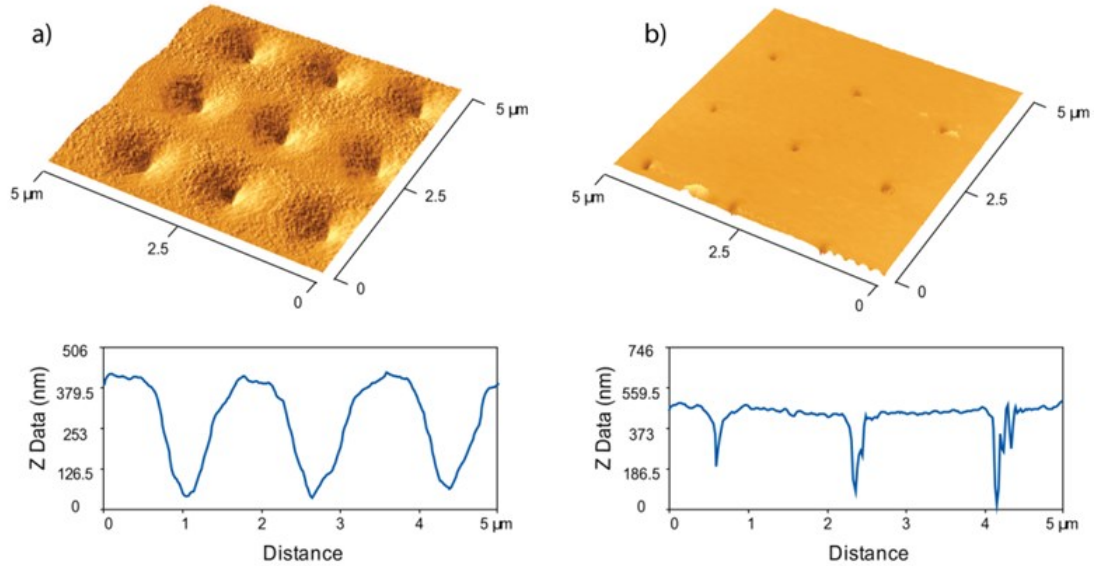


Figure 4.3 AFM analysis of conical nanopores formed at (a) 100W and (b) 25W RF power.

We observed that the conical tip radii of nanopores formed using Au NPs of 50 nm diameter were smaller than those formed using 100 nm particles and that the radii increased linearly with time (Figure 4.4c). The smallest pore diameter that we have reproducibly achieved is around 20 nm. Since the etch rate of Si is rapid, reproducible formation of even smaller pores would require further optimization in terms of tuning the etch rate as well as the Si device layer thickness.

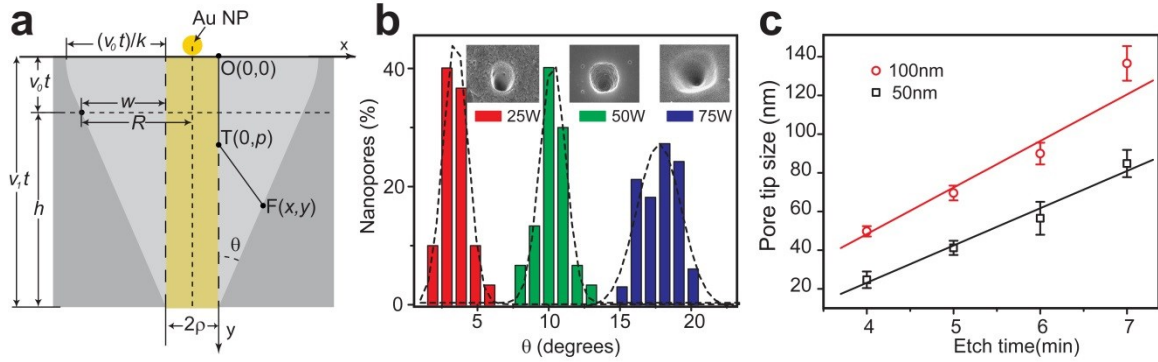


Figure 4.4 Model and experimental control of nanopore cone angle and size. (a) Illustration of our etch model for conical nanopore formation. (b) Plot of the variation of the cone half-angle with etch power (25, 50 and 75W) obtained using 100 nm Au NPs. (c) Plot of the variation of the nanopore tip size with etching time. The data was obtained using 50 nm and 100 nm diameter Au NPs (Bars indicate the standard deviation).

4.2 Material Characterization

We characterized the NP dispersed Si surface after plasma etching using Fourier Transform Infra-Red (FTIR) spectroscopy, X-Ray Photoelectron Spectroscopy (XPS) and contact angle measurements.

4.2.1 FTIR Analysis

Measurements were done on plasma etched Au NP dispersed Si wafers. The wafers were etched at 50 W, 25 sccm CF_4 / 4sccm O_2 at 500 mTorr pressure for 5 minutes using Plasma-Therm 790™ etcher. A Varian 650-IR spectrometer (Varian, Inc.) with a liquid-nitrogen-cooled mercury cadmium telluride detector was employed. Surface films were characterized with a universal reflectance accessory set to a reflectance angle of 45° . A fresh silicon wafer was employed as a background sample and was used as a reference

for background subtraction. All samples were mounted in a dry-air purged sample chamber. Each spectrum was collected over 1,024 scans with 14,236 points per scan at a 2.0 cm^{-1} resolution and the sensitivity set to 8. Samples were measured in the range of $4000\text{-}1500\text{ cm}^{-1}$. A linear baseline correction was applied. The peaks between 1000 and 1250 cm^{-1} can be attributed to oxidized Si⁴⁻⁶. Some peaks can be assigned to carbon and fluoride based bonds⁴⁻⁶.

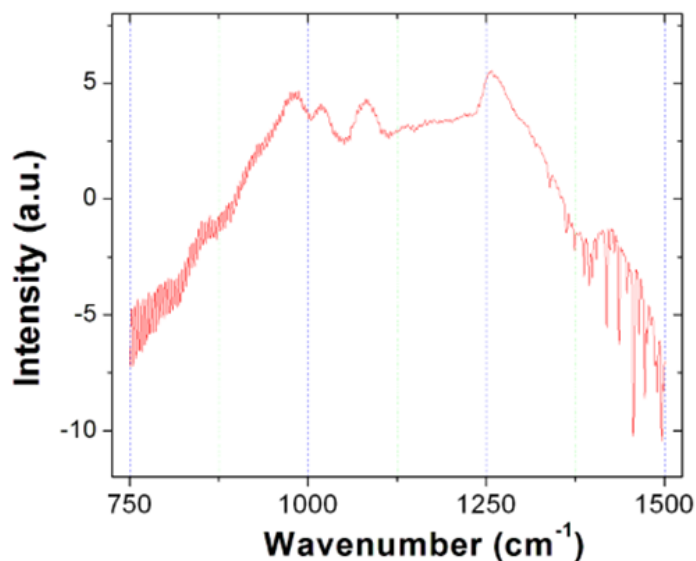


Figure 4.5 FTIR spectrum of plasma etched Si surface.

4.2.2 X-ray photoelectron spectroscopy (XPS) Analysis

XPS spectra were obtained on a Si wafer which was plasma etched after 20 nm Au NP were dispersed on its surface. The wafers were etched at 50 W, 25 sccm CF₄ / 4 sccm O₂ at 500 mTorr pressure for 5 mins using the PlasmaTherm 790™ etcher. XPS analysis was carried out using PHI 5400 high resolution spectrometer with Mg anode (300W) and anode voltage at 15kV. The X-Ray source - analyzer angle was 54.7°. Sputter Ion Gun

Model PHI 04-303 with beam voltage at 4 kV, raster size 4 mm x 4 mm, 25 mA emission and pressure of 25 mPa of Argon was used to do sputter depth profiling. Important peaks are labeled in Figure 4.6. The sputter depth profiling revealed 1.55 nm of oxide film on the silicon. The spectra revealed that the surface is predominantly composed of oxidized silicon.

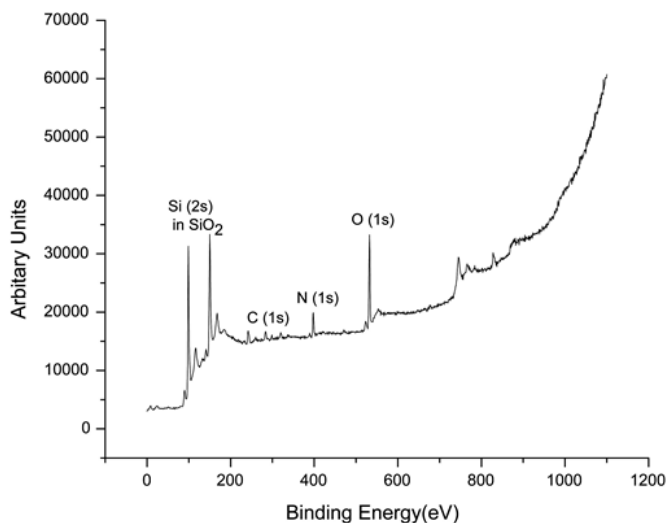


Figure 4.6 XPS of the plasma etched Si surface.

4.2.3 Contact Angle analysis

Contact angle measurements were done on plasma etched Au NP dispersed Si wafers (Figure 4.7). The wafers were etched at 50 W, 25 sccm CF₄ / 4sccm O₂ at 500 mTorr pressure for 5 minutes using Plasma-Therm 790™ etcher. A water drop at pH 7 was dispensed on the etched surface and image was obtained as shown in figure S5. Using the Java plug-in (<http://bigwww.epfl.ch/demo/dropanalysis/>) for Image J software, the contact angle (θ) was calculated using *LB-ADSA fitting* from the shape of the drop. We found that the contact angles were typically 70-80° and that the contact angle changed

with time presumably due to the rough nature of the surface. Hence, the dynamic electro-wetting of the inner nanopore walls, from the applied electric field may contribute to the appearance of noise in the system.

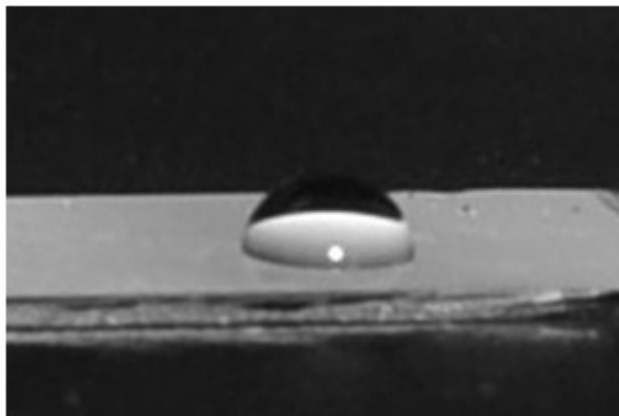


Figure 4.7 Contact angle of a pH 7 water drop on the plasma etched Si surface.

Our characterization studies suggest that the Si surface is coated with a dielectric layer, about 1.5 nm thick, composed largely of oxidized silicon. Such oxidized Si surfaces (pI ~2) are known to exhibit a negative surface charge when in contact with aqueous electrolyte solutions of pH >3 due to de-protonation of the Si-OH surface groups (pKa ~6.9)^{32,33}.

4.3 Electrical Characterization

4.3.1 Ion-current Rectification

In order to explore the use of these conical nanopores in the creation of bio-mimetic ion channels, we measured the transmembrane current across a single plasma etched nanopore (Figure 4.8). The nanopore was fabricated in a 20 μm thick Si device layer with a pore base and tip diameter of approximately 2.5 μm and 43 nm respectively (Figure 4a,

see supporting information for fabrication details). We attribute the origin of the observed rectification to the conical asymmetric geometry and the negative charge present on the pore surface^{13, 34-36} (Figure 4.8b). We observed that the rectification ratio (f) decreased from 3.9 to 2.3 when the KCl electrolyte concentration increased from 20 mM to 100 mM (Figure 4.8c). We rationalize this observation by noting that theoretical predictions based on Poisson-Nernst-Planck equations suggest that rectification occurs when the electrical double layer widths become comparable to the charged conical nanopore dimensions³⁷⁻³⁹. As the concentration of the electrolyte and consequently ionic strength increases, the double layer width decreases relative to the pore size and hence the pore becomes a less effective rectifier^{36,37}. Further, at a fixed electrolyte concentration of 20 mM KCl, we observed that the rectification ratio also varied with pH (Figure 4.8d). Significantly, the rectification ratio was found to decrease from $f = 4.2$ at pH 8 to $f = 1.1$ at pH 2, indicating that the surface charge of the pore walls play a major role in the rectification behavior. The low degree of rectification at low pH is indicative of the neutralization of the negative surface charges present on the pore wall, due to protonation. Such a pH sensitive behavior of Electrolyte Insulator Semiconductor (EIS) systems consisting of Si, oxidized silicon and aqueous electrolyte have been well previously described in the context of Ion Selective Field Effect Transistors (ISFETs)³³,

40

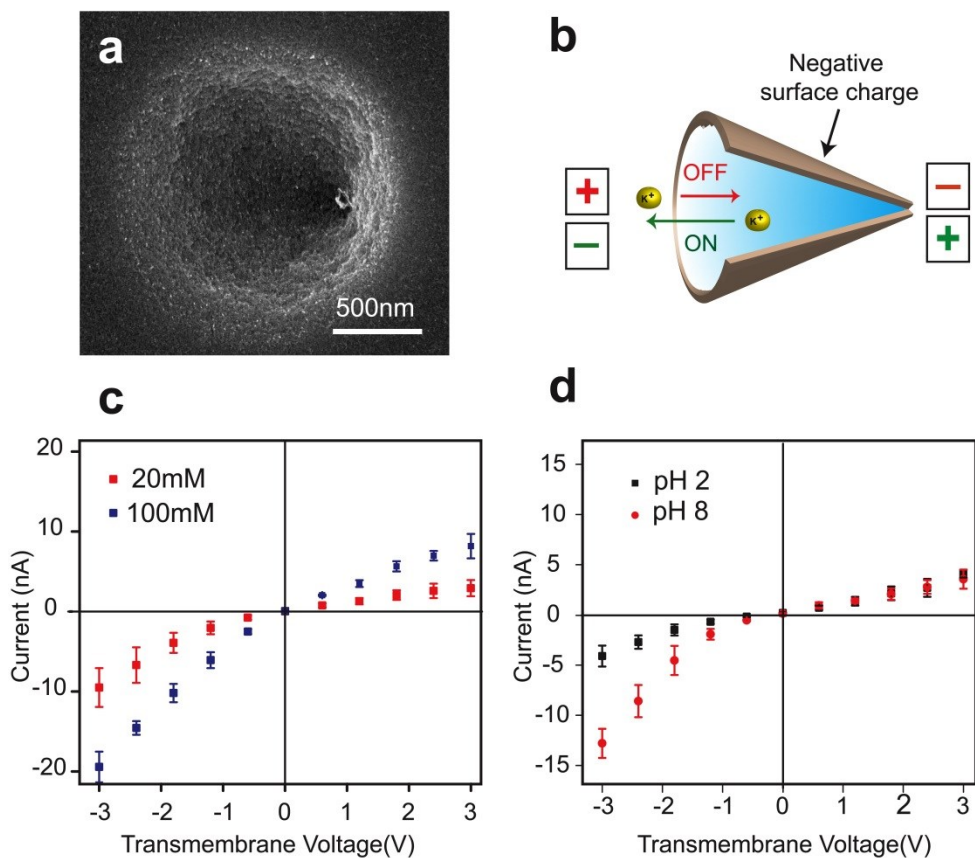


Figure 4.8 Ion-current rectification observed in an individual conical nanopore. (a) Representative SEM image of the individual conical nanopore formed by plasma etching of an e-beam patterned Au disc. (b) Illustration of ionic current rectification in a conical nanopore. The arrows illustrate the motion of cations and relative magnitude of ionic current in the corresponding electrode configurations. (c) I - V curves measured in 20 mM and 100 mM KCl at pH 7. (d) I - V curves measured in 20 mM KCl at pH 2 and pH 8 (bars indicate the standard deviation, $N=3$). The measurements were performed on a single conical nanopore with tip diameter of approximately 43 nm.

4.3.2 Switching Characteristics

One significant advantage of semiconducting conical nanopores is that the space charge at the semiconductor interface can be manipulated by the application of a voltage. We measured the I - V characteristics of transmembrane ionic transport in 20 mM KCl and observed a variation in the ionic current as a function of the voltage applied to the Si membrane (Figure 4.9).

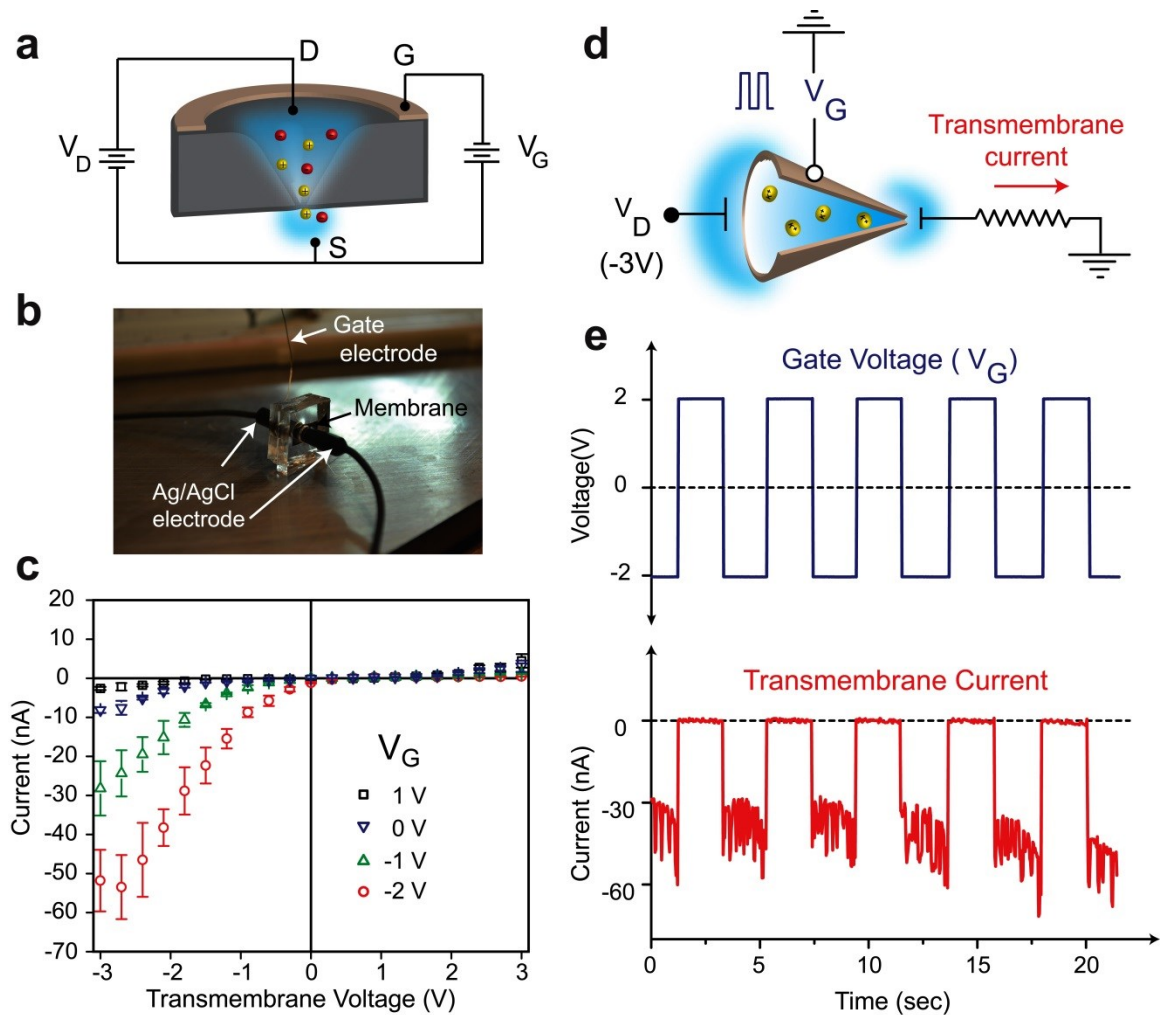


Figure 4.9 Voltage-gated switching of ionic current through an individual conical nanopore. (a) Schematic illustrating the gated ionic transmembrane transport through a Si conical nanopore. (b) Optical image of the measurement setup and (c) I_D - V_D plot with

varying V_G between -2 V to 1 V. (d-e) Switching ionic circuit. (d) Schematic of the circuit used to measure the switching behavior of the conical nanopore device, and (e) switching behavior obtained by varying the gate voltage which results in synchronized transmembrane current across the load resistor. The current-voltage recordings were made with a solution of 20 mM KCl, pH 7 and the measurements were performed on a single conical nanopore with tip diameter of approximately 35 nm (bars indicate the standard deviation, N=3).

Using a transistor analogy, we plotted the ionic current (I_D) as a function of drain voltage (V_D) for a fixed gate voltage (V_G) (Figure 4.9c). In contrast to manipulating transmembrane ion transport by varying the size, shape or surface charge of the pore using various strategies such as thiolated DNA molecules⁴¹, polyelectrolyte deposition⁴² and pH responsive polymer brushes^{43, 44}, we observe that active control can be achieved by voltage gating. We found the variation to be more pronounced at negative V_G . For example, at $V_G = -2$ V, I_D was increased by a factor of six as compared to that when no gate voltage was applied, while there was a negligible effect at positive voltages, as expected. We rationalize this result by noting that increasing the negative gate bias on the Si enhances the negative space charge within the semiconducting Si surface (as verified by Kelvin probe microscopy resulting in higher transport rate of K⁺ ions through the more negatively charged pore).

We note that this non-linear I - V behavior can be used to enable ionic switching (ON/OFF) devices (Figure 4.9) of relevance to ionic logic circuitry. Here, a square wave pulse of amplitude -2 V to +2 V was applied to the gate electrode and the transmembrane current was measured. The nanopore device was found to continuously switch between

ON and OFF states at negative gate bias (-2 V) and positive gate bias (+2 V) respectively (Figure 4.9e). We attribute the high noise in the ON state of the device to the combined effects of fluctuations in the pore surface charge, dynamic electrowetting phenomena in the porewall and the thermal fluctuations in the conductivity of the salt solution⁴⁵⁻⁴⁹. We estimate that the rectification ratios in our devices could be readily varied across two orders of magnitude by voltage gating alone and the ionic switching measurement revealed an ionic current on/off ratio of approximately 260.

4.3.3 Kelvin Probe Measurements

Measurements were done on plasma etched Au NP dispersed Si wafers. The wafers were etched at 50 W, 25 sccm CF₄ / 4sccm O₂ at 500 mTorr pressure for 5 minutes using PlasmaTherm 790™ etcher. Au NP dispersed Si wafers In Kelvin probe microscopy the AFM tip forms a capacitor with the sample surface. By applying a combination of AC and DC voltages to the tip it is possible to create a high-resolution map of the work function of the sample surface⁷ (see Figure 4.10a for a diagram of our KPFM setup). The work function can then be used to infer the charges residing on the surface.

Our KPFM scans of the wafer surface are shown in Figure 4.10a b, panels II-IV with panel I presenting the topographic scan of the same area. The images were taken using a Multimode III Atomic Force Microscope (Bruker, Inc.) configured for Kelvin probe microscopy (Figure 4.10a a). In our setup DC voltage was also applied to the sample (p-type Si wafer) and the measurement of the potential was recorded along with the topographical data from the sample. The resulting plots were analyzed in Gwyddion SPM visualization and analysis software, version 2.27 by averaging the potential across the scanned area ('matching height median' correction was applied to the image shown

here in Figure S6b, panel II). The resulting averages were then plotted vs. the potentials which was applied to the wafer (i.e. -3V, 0V, or +3V) as shown in Figure 4.10a c.

The interpretation of data on semiconducting samples is complicated by the fact that the charges are not located at the surface but are distributed inside the semiconductor over a distance which depends, for an applied voltage, on the tip-surface distance⁸. Hudlet *et al.* have determined that the interactions that occur in the system depend on the voltage applied to the wafer; it is possible that either, (1) the majority carriers accumulate on the semiconductor surface (accumulation regime), (2) minority carriers accumulate at the surface (inversion regime) or (3) the surface can be depleted of the free carriers (depletion regime)⁸. For the p-type wafers utilized in our experiments holes are the majority carriers. Application of relatively high positive potential to the wafer leads to accumulation of positively-charged holes in close proximity to the wafer surface. When high negative voltage is applied to the wafer, electrons accumulate on the surface. Hence, on application of a positive voltage to the Si membrane we expect a positive space charged region and vice-versa.

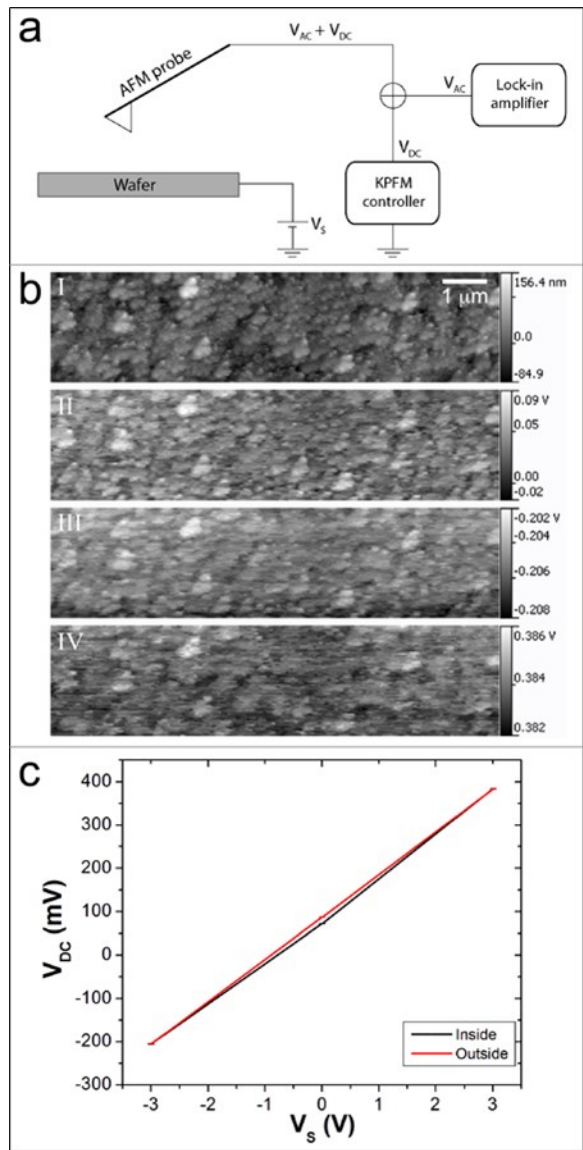


Figure 4.10. (a) Schematic illustrating the applied voltages in our Kelvin Probe Force Microscopy (KPFM) measurement. (b) KPFM scans of an area inside a pore cone. (I) Topography scan, $V_S=0\text{V}$. (II-IV) Potential scans, $V_S=0\text{V}$, $V_S=-3\text{V}$ and $V_S=3\text{V}$ respectively. (c) Work function variation as a function of the voltage applied to the sample. The work function changes by about 100 mV for each volt applied to the wafer.

4.4 Biomolecular Transport through pores

In addition to gate modulated rectification properties of small ions, we observed that active control over permeation of charged biomolecules can also be achieved through semiconducting nanoporous membranes, which is important for the creation of synthetic mimics of transmembrane cellular channels⁵⁰. We studied the time dependent permeation of fluorescently labeled Bovine Serum Albumin (BSA) molecules through an approximately 4 nm diameter nanoporous region of the membrane with and without the application of a voltage (Figure 4.11)

Importantly, as shown in the plot of fluorescence intensity with time (Figure 4.11 b), we observed significantly enhanced transport at +0.3 V bias as compared to that at 0 V and -0.3 V. We attribute this change to electrostatic effects of the negatively charged BSA (pI 4.7), and enhanced diffusion at positive voltages. In order to estimate the significance of this difference, we developed a transport model (details in supplementary information) which suggests that this difference is equivalent to a change in the diffusion coefficient of BSA by over an order of magnitude when either +0.3 V or -0.3V is applied. Thus, analogous to biological membranes, active control over transmembrane molecular transport can be achieved by the application of electric potential to Si nanoporous membrane.

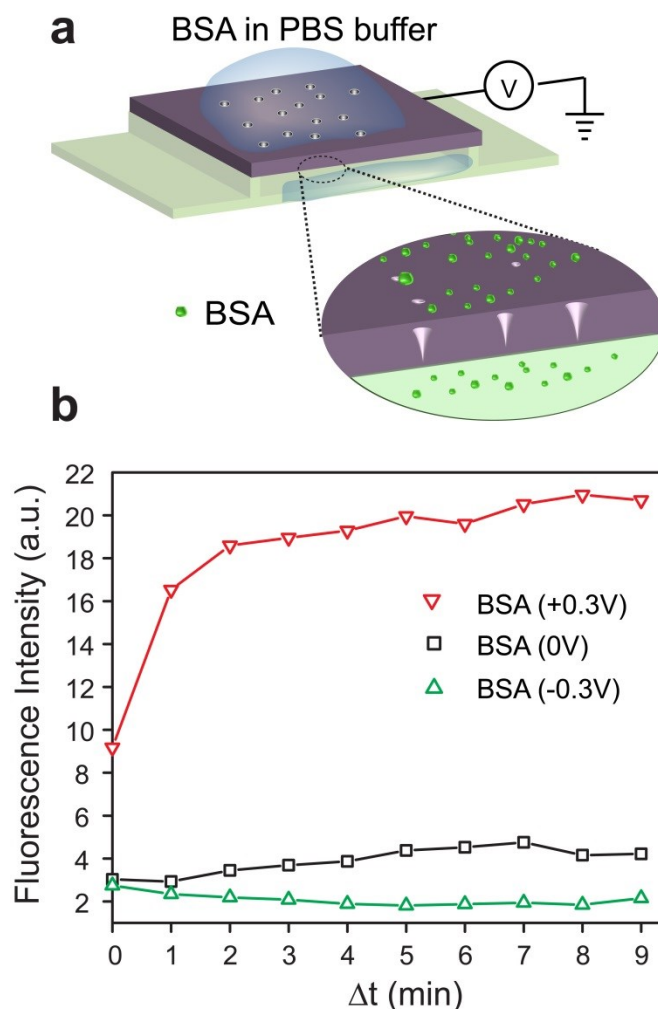


Figure 4.11 Voltage control of protein transport. (a) Schematic illustration of BSA protein transport across a nanoporous membrane, and (b) representative plot of fluorescence intensity vs. time for voltage gated (-0.3 V, 0 V, 0.3 V) transport of BSA-FITC conjugate through the membrane; Δt indicates the time from the start of observation.

4.5 Details of experimental methods

4.5.1 Nanopore Membrane Fabrication Process

Conical nanopores were etched in Si membrane by plasma etching (Figure 4.12). It is noteworthy that to test reproducibility, we used two different etchers (Technics PE-II-A and Plasma-Therm 790™) and observed some fluorine contamination while etching with the Technics PE-II-A etcher. We obtained less variation in etch characteristics using the Plasma-Therm 790™ etcher and this etcher was utilized to obtain all ionic and BSA transport results in the main text. SOI wafers with P/Boron doped device layer JM+ with <100> orientation, either 5 or 20± 0.5 μm thickness and 1-10 Ohm-cm resistivity was purchased from Ultrasil Corporation. The wafers were cleaned and the Si device layer was photolithographically patterned and dry etched to form square Si shapes. Atop the Si shapes, a dilute solution of Au NPs in DI water (~4.5x10⁷ per ml) was dispersed and dried. Plasma etching of the substrates were carried using etch gases, O₂ and CF₄ which were introduced into the chamber at a flow rate of 4 sccm and 25 sccm respectively and the pressure was maintained at 0.5 Torr. Radio-frequency (RF) plasma of 50 W at 13.56 MHz was applied for a time calibrated for the specific device layer thickness and Au NP density. Conical nanopores were formed during this process in the device layer. The Si membranes containing the nanopores were released from the wafer by etching the SiO₂ layer in conc. HF (58%) and were rinsed thoroughly in DI water. The nanopore tips and base diameters were measured using SEM imaging.

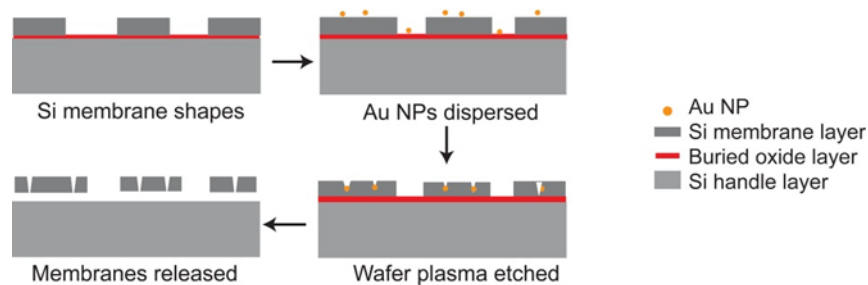


Figure 4.12 Schematic diagram of nanopore fabrication in Si membranes.

For the fabrication of individual conical nanopores, circular nanostructures were patterned using electron beam lithography process with Zeiss EVO 50 at acceleration voltage was 30kV and an area dose of approximately $200\mu\text{C}/\text{cm}^2$. The patterned substrates were developed using MIBK-IPA (methyl isobutyl ketone & Isopropanol) developer. Nanoimprinted arrays were made done using the Nanonex NX 2000-4 system. The resist NXR 1020 (6%) was spin coated at 800 rpm and imprinted. The thickness of the resist layer before imprinting was about 380 nm. The imprinting step was carried out at 130 °C and 210 psi pressure for a processing time varying from 1 min to 5 min depending on the pattern geometry. The sample was then cooled down and the mold was separated from the sample manually using a micro blade. The imprinted sample was plasma cleaned in oxygen plasma to remove the residual resist layer which was approximately 80 nm thick. For both e-beam and nano imprinted samples, 200 nm Au was thermally evaporated on the substrates and lift off metallization was performed to obtain the Au nanodiscs. Plasma etching process was carried out on these substrates to obtain the conical nanostructures.

4.5.2 Ionic Rectification Studies

Single conical nanopores were formed in Si membranes by plasma etching Au nanodiscs patterned by e-beam lithography using the methodology given above. Measurements were done on plasma etched Au NP dispersed Si wafers. The wafers were etched at 50 W, 25 sccm CF_4 / 4sccm O_2 at 500 mTorr pressure for 5 minutes using Plasma-Therm 790™ etcher. Electrical characterization of the nanopore was performed under symmetric

solution condition by measuring the current-voltage (I-V) characteristics of the Si membrane aligned with in a PDMS flow cell. Ag/AgCl electrodes (Harvard Apparatus, Holliston, MA) were attached to either sides of the flow cell by inserting the cylindrical pellets into flow channels and sealed tightly. Electrolyte solutions were then injected using a syringe in to both sides of the flow cell chambers. A Keithley 6487 picoammeter-voltage source assisted with a probe-station was used for applying the membrane voltage and the resulting current response was recorded using a Lab-view program. For all transport studies shown in Figures 4 through 5, 20 micron thick Si membranes with gold nanodiscs with 500 nm diameter and 200 nm thickness was plasma etched to form the single nanopores. The diameter of the nanopore tip was estimated using the theoretical treatment for ionic conductance through conical pore⁹. For this, we obtained electron-microscopy images of the base diameters and measured the conductance (G) of the pores in an electrolyte of known conductivity. The cells were filled with 1 M KCl solution, the current-voltage curve was recorded over low voltages and the conductance of the nanopore was calculated from the I-V graph. Using this measured conductance value; the average diameter of the nanopore tips was calculated using the equation for the ionic conductance of the conical pore⁹:

$$G = \frac{\sigma \pi d_b d_t}{4L}$$

Where σ is the specific conductivity of the electrolyte solution (Scm^{-1}), L is the length of the nanopore (thickness of the membrane), d_b is the base opening diameter and d_t is the nanopore tip opening. For studying the voltage gating behavior of Si conical nanopore Ag/AgCl electrodes were connected to the electrolyte reservoirs as mentioned previously

at the base and tip of the conical pore to act as drain and source probes respectively. A circular Au electrode was patterned using e-beam lithography around the base of the Si conical nanopore, integrated with in the PDMS flow cell as described above and was contacted by a gate probe. To analyze the switching characteristics of the conical nanopore device, we applied a square wave input signal of amplitude -2 to +2V to the gate electrode using a signal generator. The base to tip voltage was kept constant at -3V using an external power source and the input and the output signals were recorded by the Lab-View program. For these studies, more than 20 devices were prepared and tested. Based on our studies, the variability was based on pore size and for the same pore the variability was minimum (around 5-8%).

4.5.3 Biomolecular permeation studies

In contrast to ion rectification studies that were done across a single nanopore, to enhance mass flow, as might be required in practical separation experiments, we dispersed 50 nm Au NPs across a 20 μm thick Si membrane and used large areas (approximately 4 mm diameter regions) of the membrane in our studies. Due to the large size of the membrane relative to the nanopores, we anticipate that biomolecular transport is occurring across a broad pore distribution. We performed permeation studies through the conical nanoporous membranes with fluorescently labeled protein BSA (Bovine Serum Albumin, M_w 67kDa; we used BSA-FITC conjugate A9771, Sigma) diluted to 1 μM in phosphate buffered saline (PBS) through these membranes. The membranes were mounted between PDMS chambers and Ag/AgCl electrodes were used to make electrical connections with the solutions in each side of the PDMS reservoirs. The control voltages were applied to the Si membrane with respect to the Ag/AgCl electrodes in the solution. About 10 μl of

the protein solution was used for each run and the fluorescent intensity of the filtrate was monitored over a period of 10mins, with time zero set as the start of observation. The images were obtained at 350ms exposure time at 60x magnification and image stack was analyzed using MBF-Image J analysis plug-in (*Intensity vs timeplot*) for a specific region of the membrane defined by the x,y coordinates and width and height of ROI (region of interest).

4.5.4 Theoretical etch model

A theoretical model was developed to gain insight into the conical pore formation. The etch profile was calculated by minimizing the time it takes for the etch front to propagate between two points^{1,2}. The model is based on the observed accelerated etching of Si in the vicinity of Au NPs³. Figure 4.4a of the main text schematically illustrates a cross-section of the pore. The following assumptions are made in the model.

The presence of Au NP results in accelerated vertical etch rate v_1 in a narrow cylindrical region of radius ρ in the vicinity of the NP. The radius ρ of the region is assumed to be a function of the NP size; it was also assumed that the radius of the enhanced etching regions is larger than the size of the NP itself.

Experiments show that the NPs decrease in size during the etching process, which in combination with the previous assumption means that the radius of the region ρ where the vertical etch rate is enhanced decreases with increasing etch depth y . First, we neglect this decrease in the NP size, and the decrease is later accounted as a correction.

Bulk Si etching is assumed to be anisotropic with vertical etch rate denoted as v_0 and horizontal etch rate being v_0/k .

In the model, we assume two regions, one in the vicinity of the NP where etch rate v_1 is enhanced as compared to v_0 , the etch rate in the absence of the NP. Etching starts simultaneously across the top of the cylinder shown in yellow. Accordingly, the etch front is assumed to be flat across the enhanced etch region at all times.

Vertical bulk etching of Si far away from the NP is taken into account once the profile of the pore has been found.

We apply the principle of least time^{2,3} to obtain a simple analytical expression of the etch-edge profile. The principle, as applied to the problem under consideration, states that etching proceeds along the path that minimizes etching time. In other words, etching will proceed along the path OTF (path line along points O, T, and F in Figure 4.4a) such that the derivative of time t with respect to the position p of point T is zero: $dt/dp=0$.

The time it takes for the etch front to propagate along the path OTF is given by

$$t = \frac{p}{v_1} + \frac{\sqrt{k^2 x^2 + (y-p)^2}}{v_0} \quad (\text{Equation S1}).$$

Here we have chosen the origin of our coordinate system to be displaced by p from the axis of symmetry of the system to simplify mathematical expressions. Setting the derivative of time with respect to p to 0 (

$$dt/dp=0) \text{ yields the following expression for } p: p = y \pm \frac{kv_0|x|}{\sqrt{v_1^2 - v_0^2}} \quad (\text{Equation S2}).$$

This expression can be used to eliminate p from Equation S1 and thus to link the coordinates

$$\text{of the point F}(x,y) \text{ and time } t: y = v_1 t - \frac{k|x|\sqrt{v_1^2 - v_0^2}}{v_0} \quad (\text{Equation S3}).$$

Equation S3 is linear in y and x and thus describes a straight line. The three-dimensional etch-edge profile is obtained by rotating this line around the axis of symmetry defined by the NP.

This rotation results in an etch profile which is a cone with a flat bottom and straight sides. We note that the vertical etching of bulk Si results in removal of layer of thickness $v_0 t$ from the top of the Si. Thus the final height of the cylindrical pore is $h = (v_1 - v_0)t$.

The radius R of the base of the pore can be calculated by setting $y = v_0 t$ in Equation S3,

and then solving for x : $w = x(y = v_0 t) = \sqrt{\frac{v_1 - v_0}{v_1 + v_0}} \frac{v_0 t}{k}$ (Equation S4) and then adding the

radius ρ of the cylinder, where etching rate is increased: $R = \rho + w = \rho + \sqrt{\frac{v_1 - v_0}{v_1 + v_0}} \frac{v_0 t}{k}$

(Equation S5a). Similarly the radius r of the tip of the cone is obtained by setting y to be equal to the thickness τ of the SOI layer ($\tau = 5.0 \mu m$ in our case) and solving Equation

S3, for x : $r = \rho + \frac{v_0(v_1 t - \tau)}{k\sqrt{v_1^2 - v_0^2}}$ (Equation S5b), where we have assumed that $t > \frac{\tau}{v_1}$. The

half-angle of the cone θ can be obtained from its height and tip and base radii:

$\theta = \arctan \left[\frac{1}{k\sqrt{(v_1/v_0)^2 - 1}} \right]$ (Equation S6). A plot of values of the cone half-angle as a

function of (v_1/v_0) ratio for $k=1/4, 1/2, 1, 2, 4$ is shown in Figure 4.12. For practical purposes the region of low k is most interesting since it allows for gradual variations in the cone angle.

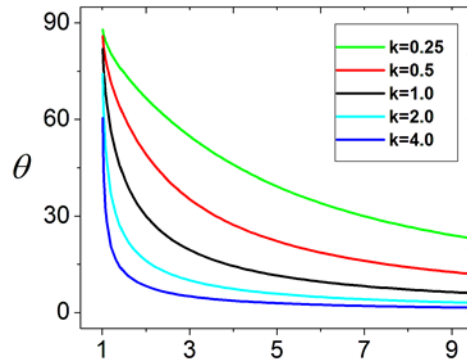


Figure 4.13 Plot of the cone half angle as a function of the ratio of the enhanced etch rate to the unmodified etch rate for different etch rate anisotropies.

We now turn to the effects that decreasing NP size has on the cone angle. We note that under typical conditions the NPs decrease in size from ~ 100 nm to ~ 50 nm as they pass through the $5 \mu\text{m}$ thick Si layer. According to our first assumption this implies that the region where the vertical etch rate is enhanced is not cylindrical but instead conical in shape. The half angle of the cone can be estimated as follows. Our experiments show that the NPs typically decrease in size from 100 nm to 50 nm as they traverse the silicon layer $5 \mu\text{m}$ thick, i. e. the cone half-angle is $\tan(\alpha) \sim (50\text{nm})/(5\mu\text{m})$, i.e. typically α is less than 1° . When etching of bulk Si is almost isotropic, i.e. when k is close to 1 we can approximate the effects of the enhanced region being a cone by simply adding α to the value of the half -cone angle obtained above: $\theta' = \theta + \alpha$, where θ' is the approximation to the half-cone angle which results when the NP size decrease is taken into account. More detailed analysis would require knowledge of mechanisms of etch rate enhancements in the vicinity of the NP and specifically how r depends on the particle size

4.5.5 Numerical Simulations of Protein Diffusion through Nanopores

As we have shown in Figure 4.11b of the main text, transport of charged protein molecules, specifically of BSA can be changed by the application of external voltages to the wafer. Importantly, application of positive potential to the wafer increases transport of BSA (isoelectric point in water at pH 4.7).

We performed numerical simulations of BSA diffusion through a single pore in order to estimate diffusion coefficient variation as a function of applied voltage. Numerical simulations were conducted using COMSOL 3.5 (COMSOL, Inc.). The pore and the PDMS chamber were assumed to be cylindrically symmetric. The height of the PDMS chamber (shown in green in Figure 4.13a) was set to 2 mm to match the experimental conditions. The diameter of the chamber was determined from the average separation between the pores. We used a representative density with an approximated pore separation of 1642 nm. Accordingly, the radius of the chamber around a single pore was set to be 821 nm. The dimensions of the pore tip were assumed to be 80 nm with a slope angle of 10° within a 20 μm thick membrane. For the boundary conditions, we assumed that the chemical concentration was maintained at constant value at the base of the pore; all the other boundaries were set to have no flux through them.

We modeled both non-mixed static (Figure 4.14b) and well-mixed (Figure 4.14c) systems in the PDMS chamber. Here, mixing was modeled by increasing the diffusion coefficient of the protein by a factor of 10^5 , i.e. the diffusion coefficient in the PDMS chamber was assumed to be $6 \times 10^{-6} \text{ m}^2/\text{s}$ while the diffusion coefficient of BSA¹⁰ was

assumed to be $6 \times 10^{-11} \text{ m}^2/\text{s}$. Mixing the solution in the PDMS chamber results in more uniform distribution of the diffusing protein in the PDMS chamber.

Comparison of the numerical simulations with the experimental data shown in Figure 4.11 of the main text suggests that the diffusion coefficient in our experiments varies by over an order of magnitude as a function of the voltage applied to the wafer between +0.3 and -0.3 V. The model also provides insight in that it suggests that increasing the pore density would decrease the effective diffusion variation as a function of applied voltage.

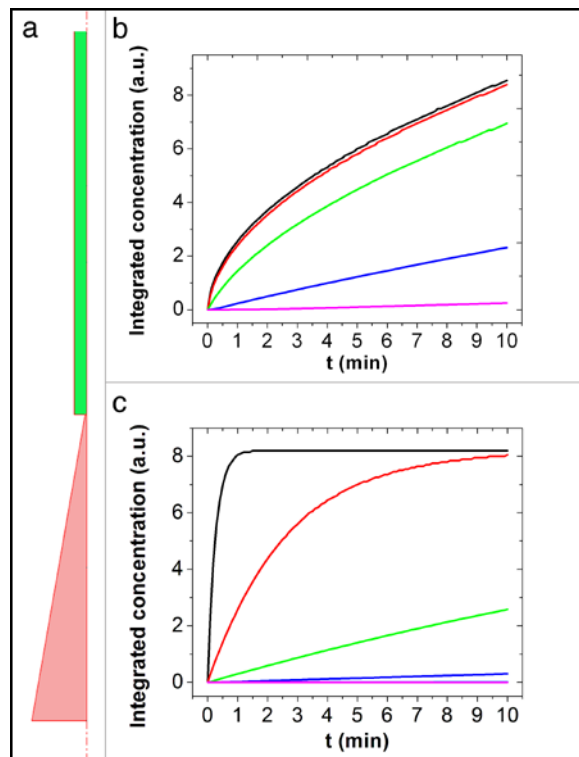


Figure 4.14 (a) A schematic of the geometry used in the numerical simulations. The pore is shown in red while the PDMS chamber is shown in green. The axis of cylindrical symmetry is shown with the dashed red line. (b) Plot of integrated concentration of BSA in the chamber as a function of time; no mixing was assumed. The black line corresponds

to diffusion coefficient of BSA being 6×10^{-9} m²/s, red to 6×10^{-10} m²/s, green to 6×10^{-11} m²/s, blue to 6×10^{-12} m²/s, cyan to 6×10^{-13} m²/s and purple (overlaps with cyan) to 6×10^{-14} m²/s. (c) Plot of the integrated concentration of BSA in the chamber as a function of time; strong mixing was assumed. The color scheme is the same as used in (b).

4.6 Summary

In summary, we have uncovered a convenient and versatile process to form conical nanopores in semiconducting, single crystal Si substrates. The process is simple, can be utilized in a maskless, lithography free manner which increases its accessibility. Additionally, semiconducting nanopores allow facile control over transmembrane ionic and molecular transport and it is conceivable that the incorporation of gate dielectrics could enable ionic field effect transistors. Since the process is versatile and compatible with MEMS / CMOS processes, these voltage gated ionic devices could be integrated with electronic and micromechanical systems.

Chapter 5

Bacterial Nanohybrid Devices[§]

5.1 Introduction

Nano-scale science and engineering enables the creation of functional materials, devices, and structures with precise geometry by controlling matter at the atomic and molecular scales⁸¹. Such nano-structured objects can be engineered to possess a wide variety of functionalities such as mechanical, electronic, plasmonic, magnetic, optical and sensing, by exploiting novel properties and phenomena exhibited at these size scales. In particular, nanostructures can be engineered to offer numerous potential applications in a variety of biomedical fields such as drug delivery, minimally invasive surgery, endoscopy, sensing etc⁸² (Fig.5.1). Micro and Nano-lithography processes including nano-imprint lithography enables the fabrication of such sub-micron structures with high-throughput and low cost. In addition, configuration of nano-lithographically patterned two-dimensional geometries to specific three-dimensional architectures possessing numerous physical properties can be achieved by utilizing the power of self-assembly phenomena described in the previous chapters^{44,45,83-85}. However, much of the potential of the nano-objects made possible by the miniaturization techniques is limited by the challenges in enabling motion or propulsion to such nano-structures and devices. Providing

[§] The work reported in this chapter is based on manuscript under preparation: James T et al “Remote Control of a Bacteria using Plasmonic Nanoantenna”

actuation/propulsion and manipulating these structures at these size scales has thus been of increasing scientific interest⁸⁶⁻⁸⁹.

In the biological world, micro-organisms such as bacteria possess a unique ability to move at small length scales with very high efficiency^{86,90}. Bacteria are highly agile and are power efficient swimmers, exhibiting different types of motions such as run-and-tumble, swarming, gliding, and twitching and they have remarkable swimming speeds of up to 30 times their body lengths per second^{91,92}. These modes of motion play an important role in guiding the response of bacteria to external stimuli in phenomena such as chemo-taxis, photo-taxis, and magneto-taxis. Bacteria propel themselves in viscous fluid owing to the “asymmetry” of flagellar rotation making them function as biological “Brownian motors” by the efficient conversion of chemical energy into mechanical motion⁹³⁻⁹⁵. In addition bacteria are ubiquitous, which makes their machinery easily accessible in almost all kinds of environments. Due to the vast amount of genetic and metabolic knowledge associated with *Escherichia coli*, they have been used in delivery of drugs as well as in regenerative medicine⁹⁶. Intravenous injection of *E. coli* into live animals has been used for real-time visualization of localization, survival and replication of engineered bacteria in implanted tumours and their metastases in live animals⁹⁷. They have also been utilized to serve as carriers of DNA based vaccines^{98,99}. Recently, there has been interest in using randomly moving bacteria to power mechanical micro-machines such as systems of microscopic gears¹⁰⁰. However, since the bacterial motion is random walk, thermodynamic laws prohibit the harnessing of any useful work from it. The potential in utilizing the chemical energy powered bacterial motion is thus

significantly dependent on the ability in "taming" them or in bringing forth control to their motion.

5.2 Interfacing of Functional Nanostructures with Motile Bacteria

Nanoscale engineering and biological systems are two fields that can mutually benefit from each other; with nanoscale engineering providing tools to control and modify biological processes while biology provides the systems and materials to enable higher functionalities for nano-engineered tools. Enabling such a biotic-abiotic conjugate at the nano-scale can hence provide the platform to perform tasks that are currently deemed difficult or impossible by the realization of hybrid systems possessing advanced capabilities¹⁰¹. A synergistic integration of biological components with abiotic systems enables ways to design and create hybrid devices with some of the amazing capabilities exhibited by living systems. For instance, living system composing of biological components possesses the astounding ability to produce mechanical motion from chemical energy making them an attractive means to provide actuation and motility to functional abiotic components^{87,100,102}. In addition, the functionalities such as plasmonic property of the nanostructures interfaced with the microorganism can be utilized to make them function as nanoantenna to receive external signal and exert control over the motility of the microorganism.

Here we present a conceptually new approach where engineered functional nano objects are directly interfaced with motile bacterial cells enabling the creation of multi-functional 'nanostructure-bacteria hybrid devices'. Such bacteria-nanostructure hybrid devices will be self-propelling in addition to exhibiting the engineered functionality of the interfaced nanostructure (Fig.5.1a). Further, the integrated nano-structure on the

bacterial cell wall could act as an antenna for external stimuli and hence enable the possibility of remotely controlling the bacterial motion. Specifically, we demonstrate the interfacing of plasmonic nanostructures with motile bacterial cells and the ability to plasmonically induce changes in the normal bacterial motion. Such an interfacing of the nanoengineered multifunctional structures with motile bacterial cells thus results in an outcome that is two-fold- 1. It renders propulsion to the nanostructures and thereby enables to utilize their full potential. 2. It enables a way to remotely control the bacterial motion by the nanostructures acting as antenna for control signals (Fig. 5.1a).

Nano-scale objects can be engineered to exhibit a number of functionalities/properties that are not present in their micro or macro counter parts. Metal nano-objects such as nano-rods exhibit heating effect under light illumination and this effect is more pronounced at the frequencies corresponding to their plasmon resonances¹⁰³⁻¹⁰⁵. Here we exploit the use of such plasmonic nano-objects to act as nano antennas for accepting external applied electromagnetic energy and exerting a thermal control signals in the bacterial nanohybrid device^{106,107}. Among different nanostructures that has the potential to be used as photothermal antennas, gold nanoparticles are among the top choices as they are the strongest nanoabsorbers .

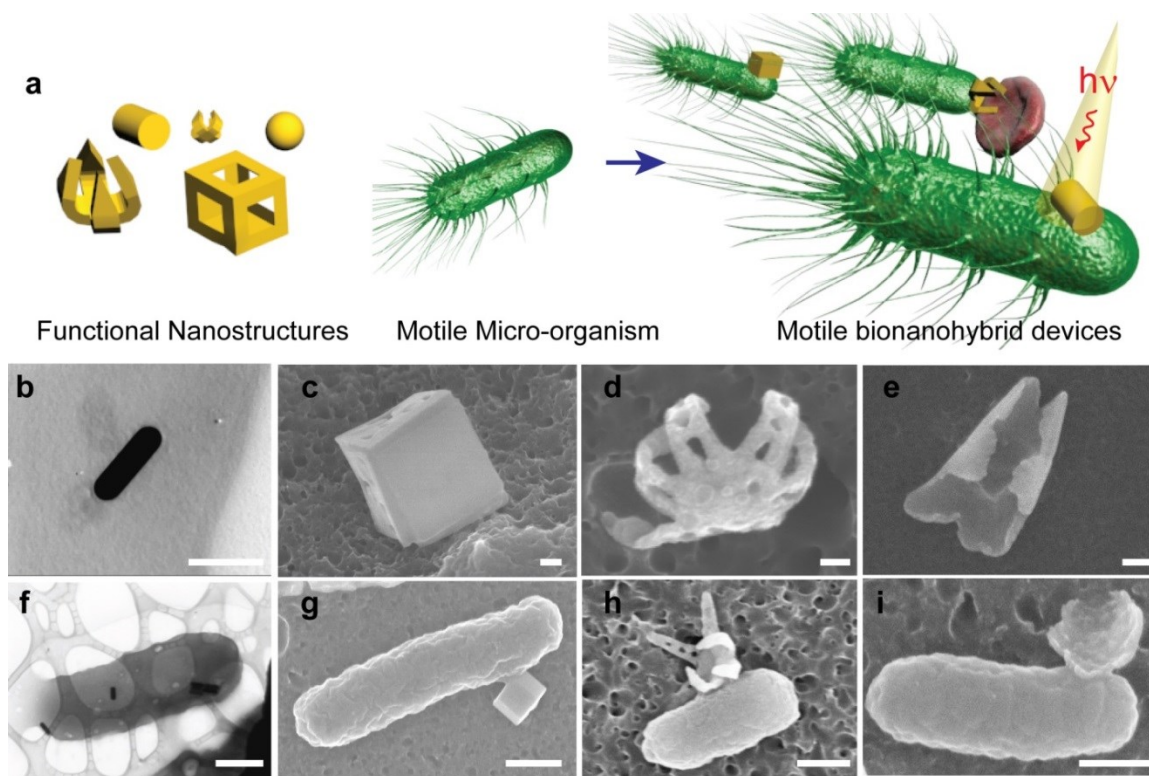


Figure 5.1: Bacterial nanohybrid devices (a) Schematic illustrating the concept of bacteria-nanostructure assembly. (b) TEM image of nanorod and SEM images of various 3D nanostructures such as (c) nanoboxes (d) nanogripper and (e) nanostar architectures. The corresponding assembled bacterial nanohybrid devices are shown in (f), (g), (h) and (i). Scale bars for Fig. 5.1(b) - Fig. 5.1(e) indicate 100nm and Fig. 5.1(f) – Fig. 5.1(i) indicate 500nm.

Simple nano-objects such as plasmonic nano-rods (Fig. 5.1b) can be attached to bacteria to form these bio-nanohybrid devices. Further, utilizing advances in nanotechnology and self-assembly described in the earlier chapters, nanostructures of various geometries, precisely patterned in all three dimensions can be formed such as nanoboxes, nanogrippers, and plasmonic nanostar antennas (Fig. 5.1b-e). These 3D nanostructures are attached onto motile *E. coli* cell surface (Fig. 5.1g-i). These bio-nanohybrid devices

thus combine the functionalities of bacteria in serving as stimuli responsive biological locomotives possessing the engineered functionalities of the nano-structures.

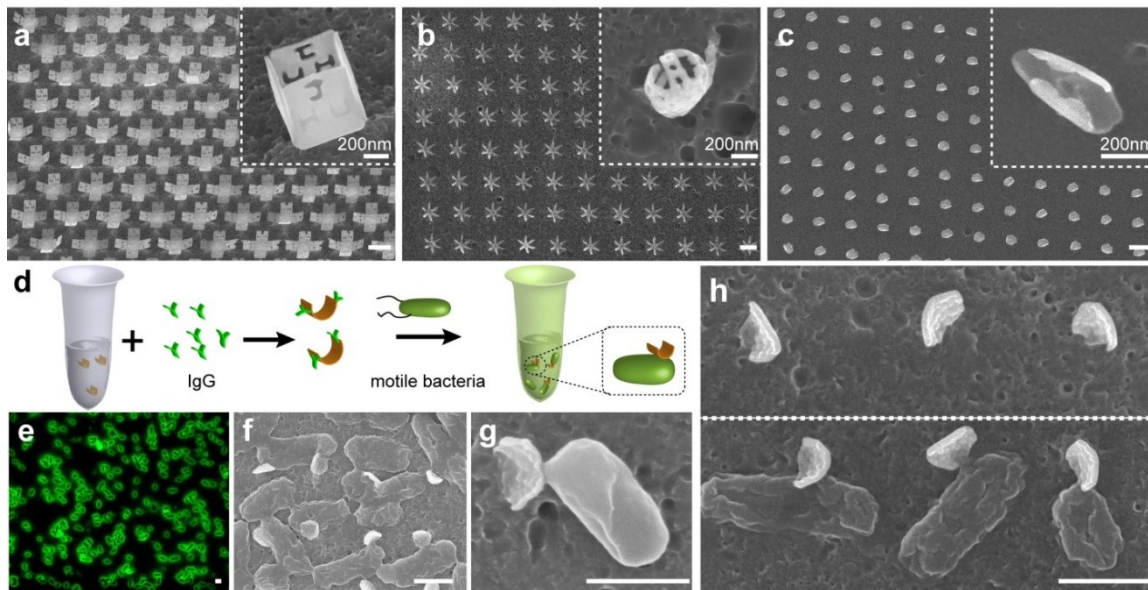


Figure 5.2: Nanostructure fabrication and bacterial assembly (a) nanoboxes (b) nanogrippers and (c) nanostar architectures fabricated using nanolithography and tin-reflow folding process (d) Schematic illustration of attachment scheme. (e) Fluorescence image and (f) SEM image of the assembled bacterial nanohybrid devices and (g) magnified image of a single bacterium nanohybrid device. (h) SEM image and of nanostructures before (top panel) and after bacterial assembly (bottom panel). Scale bars indicate 1 μ m.

5.2.1. Creation of Bacterial-Nanostructure Interfaces

Figure 5.2 demonstrates the fabrication of large number of 3D multifunctional structures such as nanocubes (a), nanogrippers (b) and nanostar shaped plasmonic antennas (c) by utilizing e-beam lithography and nanoimprint lithography. We have utilized grain coalescence to fold these structures to 3D geometries thus resulting in the assembly of

nano-scale structures that are precisely patterned in all three dimensions. (See Materials & Methods). Next, the interfacing of nano engineered structures with motile bacterial cells was achieved through selective immuno link chemistry (Fig.5.2d). First, the surfaces of the structures were prepared for biofunctionalization using a thiol based self-assembled monolayers (SAM). The structures were then biofunctionalized with polyclonal anti-*E coli* IgG and incubated with the bacterial culture, leading to a full interfacing on to the bacterial cell wall. Large scale production of the various 3D nanostructures using nanoimprint lithography followed by self-assembly based folding techniques enable the formation of a large number of bacterial- nano hybrid devices (Fig. 5.2e-g). Notably, this offers the ability to selectively interface the nanostructures on the bacterial cell as demonstrated by the SEM image of the biofunctionalized nanostructures before and after the attachment to bacterial cells (Fig 5.2 h).

5.3 Motion Analysis of Bacterial-Nano hybrids

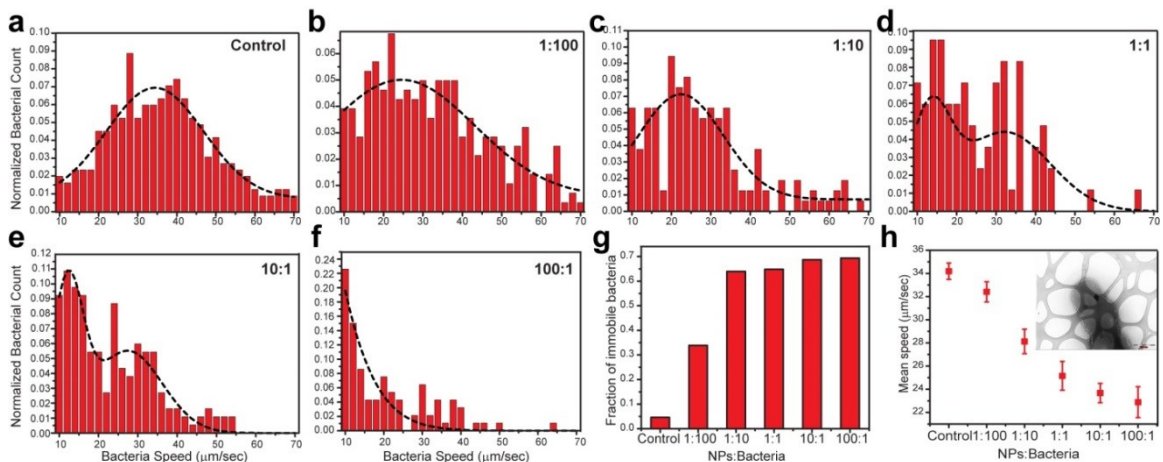


Figure 5.3: Enabling propulsion to nanostructures through motile bacterial interfacing. (a-f) variation of linear speed of the nanostructure interfaced bacterial cells at various densities of nanostructures. Ratios indicate nanoparticle to bacteria interfacing

ratio (g) histogram showing the fraction of bacterial population with speed less than $10\mu\text{m}/\text{sec}$ and (h) mean speed of the bacterial population corresponding to nanostructure density (errors bars at std. error). Inset showing TEM image of bacteria with attached plasmonic nanoparticle.

To demonstrate the ability of the motile bacterial cells to impart motion to the engineered nano-objects, we interfaced nanorods with cultured bacterial cells at various densities and analyzed their motion. To understand the effect of the nanostructure interfacing to the bacterial cell wall, linear speeds of bacterial cells interfaced with plasmonic nanostructures were analyzed using a particle tracking algorithm (Metamorph, Molecular devices) from recorded videos. The unmodified bacterial cells without any nanostructure attachment were found to exhibit an average swimming speed of $\sim 34.5\mu\text{m}/\text{sec}$ (Figure 5.3a). Figure 5.3 b-f shows the histograms of the speeds of bacteria-nanostructure hybrids at various ratios of nanostructures: bacteria interfacing. Upon increasing the nanostructure density, we observe a reduction in their mean speed from $\sim 34.5\mu\text{m}/\text{sec}$ corresponding to unmodified bacteria to $\sim 23\mu\text{m}/\text{sec}$ for an interfacing ratio of 100:1 (Fig. 5.3g). At higher densities of nanostructure attachment the fraction of bacteria that was considered to be very slow/immobile ($<10\mu\text{m}/\text{sec}$) was found to increase (Fig. 5.3h). This demonstrates the concept of utilizing the biological motors of motile bacteria a means to provide locomotion to the nano-engineered tools.

5.4 Plasmonic control of bacterial motion

Next we investigated the ability to remotely control bacterial motion through the interfaced plasmonic nanostructure acting as receiving antenna. Plasmonic nanostructures

such as nanostars¹⁰⁸ and nanorods¹⁰⁹, owing to their immense optical absorption has the potential to act as nanoantennas to receive remotely applied control signals.

Normal bacterial taxis involves a series of run and tumble motion in response to sensory cues such as chemical gradients and variations in temperature etc.- a process that involves steps in sensory reception, signal transduction and motor modulation. Modulation of bacterial motile behavior through controlled changes in chemical¹¹⁰⁻¹¹², electrical¹¹³, optical^{114,115} and thermal¹¹⁶⁻¹¹⁸ triggers have been previously reported¹¹⁹. Specifically, thermal impulses have been shown to influence the run and tumble bias of the bacterial motion^{116,120}. The plasmonic antennas can be excited with light wavelengths corresponding to their plasmon resonances, allowing to control the motile behavior of the bacterial nanohybrids via photothermal signals.

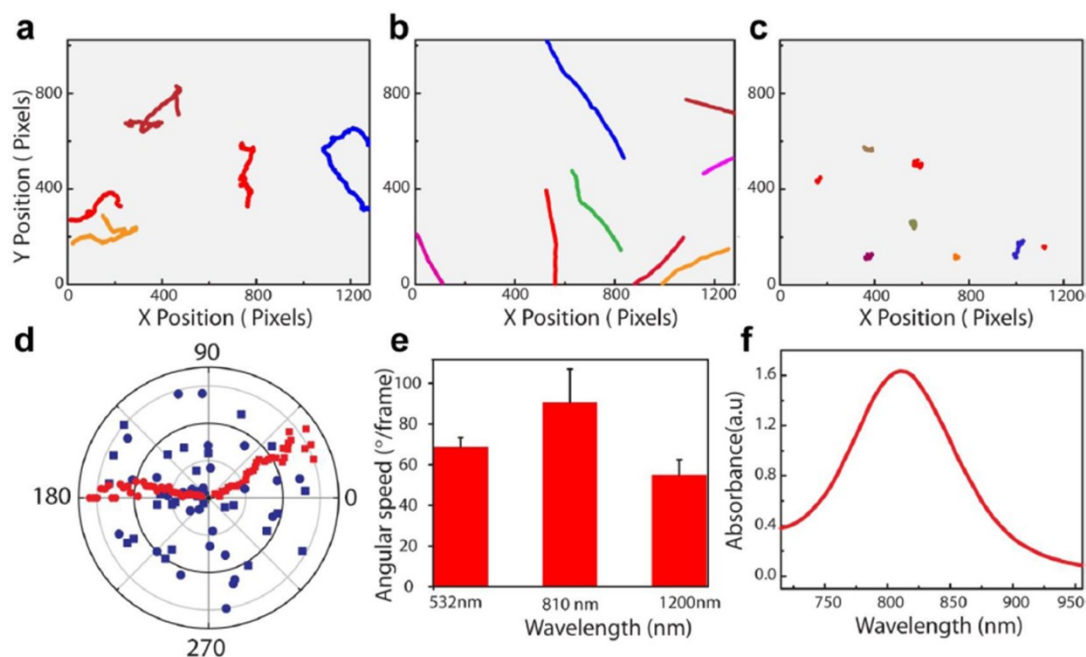


Figure 5.4: Characterization of plasmonic control: Trace images showing the trajectories of bacterial motion with (a) no LASER (b) plasmonically induced straight runs and (c) plasmonically induced exclusive tumbles. (d) Radial pole plot of angular variation of the laser induced runs (red) and tumbles (blue) for two bacterial hybrids each (e) Angular speed of bacterial nanohybrids exposed to 3 different frequencies. (f) UV spectrum of nanoparticles.

While our results suggest that nanostructure loading can alter the motility of bacteria, the unique properties of abiotic nanostructures provide an important means to enable real-time interfacing with the macroworld. Hence, we conjugated motile bacterial cells with plasmonic nanoobjects in a ratio of 10:1 (nanoobjects to bacteria) and analyzed their motion under the exposure to Near Infra-Red (NIR) radiation (Fig. 5.4a-d). The changes in the linear and angular speeds of the bacteria were used as measures to quantify the mode of bacterial motion (supplementary information). Tumbliness of the

bacteria has been reported previously to be directly proportional to the angular speed of the bacteria¹²¹. We observed that bacterial hybrids showed the classic run and tumble motion without laser irradiation which is dramatically altered to straight runs at low intensity ($2\text{W}/\text{cm}^2$) and predominantly tumbling motion at higher intensity ($10\text{W}/\text{cm}^2$). We attribute the change in motility to nanoparticle plasmon absorption and local heating of the microorganism and performed several experiments to test this explanation. Firstly, since plasmon resonances are frequency selective, we measured the angular speed which is a measure of the extent of tumbliness on irradiation with three lasers of different frequencies 532 nm, 810 nm and 1200 nm (Fig. 5.4e). We observed the largest effect with irradiation of 810 nm which coincides with the maximal absorption and plasmon frequency of the gold nanorods that were attached to the bacteria (Fig. 5.4f).

We believe that the photothermal heating corresponding to the plasmonic control signal I1 influences the thermotactic behavior of the bacteria. This could be saturating the response mechanism of the cells resulting in the “straight runs”. This is consistent with the response to heating from mild electric shocks¹¹³ as well as chemoattractants¹²². The plasmonic control signal I2 causes a greater transient temperature increase and bacteria were found to exhibit predominant tumbling. Such response was previously reported for stronger electric shocks¹¹³ and could be resulting from an emergency response of the cells to divert away from strong negative signals.

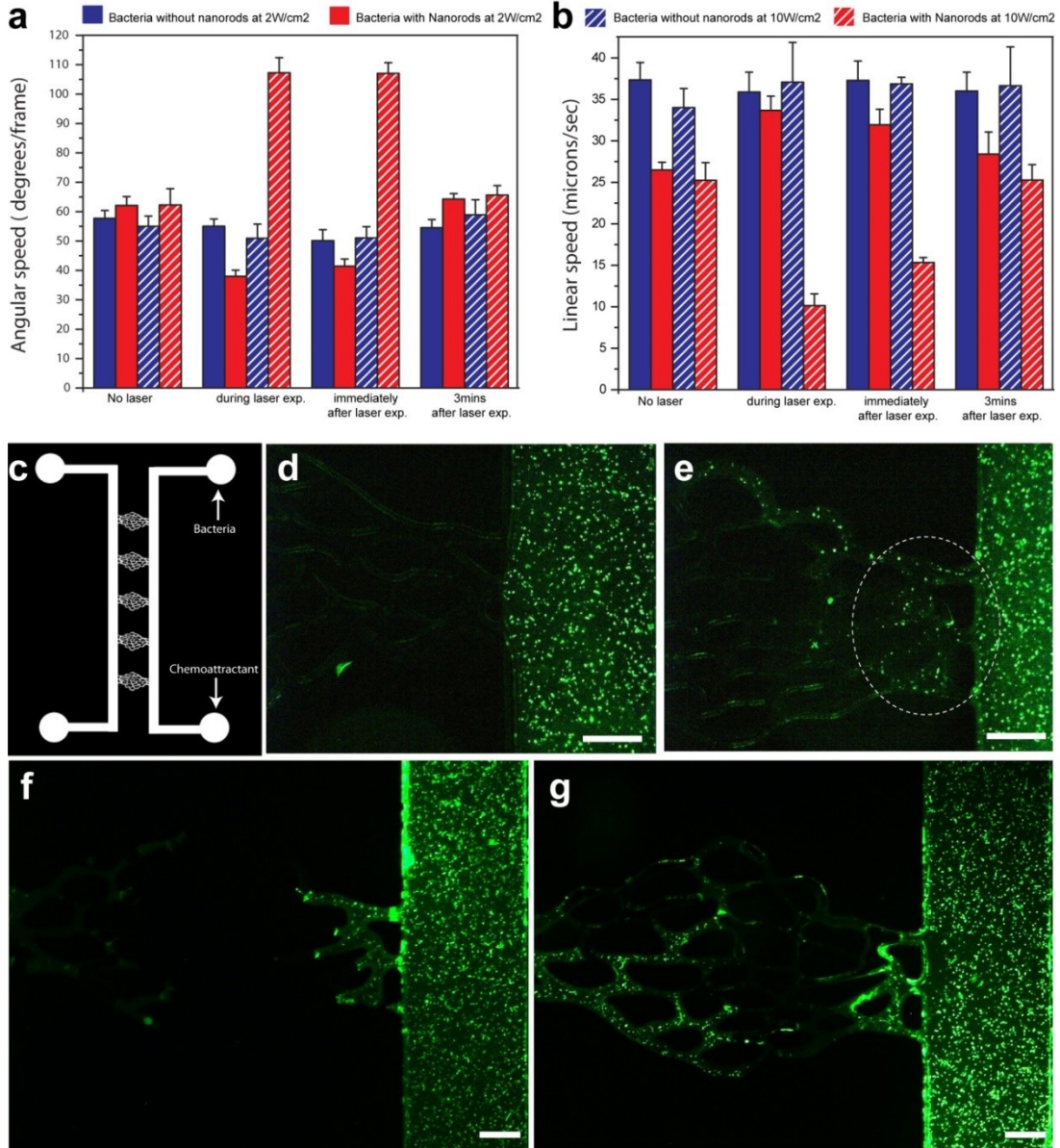


Figure 5.5: Remote control of bacterial motility via plasmonic nanoantenna: Variation in angular (a) and linear (b) speed of bacterial motion during various stages of laser exposure at intensities. (c) Schematic of the engineered microvasculature geometry. (d) Fluorescent image of bacterial motion in the channel without the exposure of NIR signals preferentially towards the chemo-attractants. (e) Plasmonically controlled bacterial nanoantenna hybrid showing control and change in motion direction towards

microcapillary network caused by induced tumble. **(f and g)** Fluorescent images of the bacterial motion and progressive dispersion in to microcapillary network with the laser exposure.

Next, in order to better understand the degree of control that can be exerted on the bacterial motile behavior through the plasmonic nanoantenna, we went on to characterize their motion in detail. The changes in the linear and angular speeds of the bacteria are used as measure to quantify the mode of bacterial motion. Tumbliness of the bacteria has previously been reported to be directly proportional to the angular speed of the bacteria¹²¹. Figure 5.5a and b shows the variation in angular and linear speeds of bacterial motion during various stages of exposure to plasmonic control signals such as before exposure, during exposure, immediately after exposure and ~ 3mins after exposure.

The blue bars indicate the results of the control experiment with bacterial cells not interfaced with plasmonic nanoantennas exhibiting no noticeable effect in their motility due to the control signals. The bacteria-nanohybrids when exposed to the control signal I1 was found to exhibit a decrease in the angular speed and corresponding increase in the linear speed indicative of exclusive runs during and immediately after the exposure to the plasmonic signal, as was already indicated by the motility trajectories. Next, the angular and linear speed of the bacterial-nanoantenna hybrids are analyzed up on the exposure to the tumbling inducing plasmonic control signal I2. The angular speed was found to increase, with a corresponding decrease in linear speed during and immediately after the exposure, consistent with the exclusive tumbling behavior observed. The linear and angular velocities were found to return to normal after ca. 3min of the NIR exposure of both in both cases.

To demonstrate the ability to use this plasmonic control of the motile behavior of the bacterial-nanohybrids, in remotely guiding them, we performed a series of experiments in micro-channels and junctions. Most importantly as a demonstrative example for the ability to remotely control the bacterial nanohybrids to move in to constricted and hard to reach areas, we examined the ability to control the bacterial motion in an engineered microchannel structure that simulates microvasculature geometry, against a chemo-attractant gradient (Fig. 5.5c to g). Fig. 5.5c shows the drawing of the microvasculature geometry indicating the location of the bacterial nanohybrid entry and the application of the chemo-attractant L-serine. Without the exposure of the plasmonic signals the bacteria shows preferential motion towards the chemoattractant as expected without entering in to the microvasculature. The exposure to plasmonic control signal I2 breaks this normal chemotactic behavior and induces tumbles and triggers entry in to microvasculature (Fig.5.5e). This was used as a way to disperse bacterial nanohybrids in to various sites in the microvasculature geometry progressively (Fig. 5.5 f and g). This demonstrates that in addition to the bacterial cell acting as a means to provide locomotion to the nano tools and objects, such a direct integration of functional abiotic nanostructures with biological microorganisms also brings forth an ability to control the motion of these microorganisms by acting as an antenna for external stimuli.

5.5 Materials and Methods

5.5.1 Fabrication of Multifunctional Nanostructures

E-beam fabrication of structures (Nanoboxes, Nanogrippers): On an n-type <100> bare silicon wafer, 100nm of an electron-beam (e-beam) resist, polymethylmethacrylate

(PMMA, MW950K 2A) was spun at 3000rpm and the wafer was baked at 185 °C for 3 min. An electron beam controlled by a RAITH system (v 4.0) was used to pattern the resist. The resist was developed using an MIBK developer (1 to 3 parts IPA) for 35 s. Then, 5nm gold (Au), and the respective thickness of Ni (thickness varying from 10nm - 50nm) and the required thickness of Sn (thickness varying from 10nm- 50nm) were evaporated using e-beam evaporator. After evaporation, the resist was dissolved in acetone for lift-off metallization. The substrate was rinsed in IPA and DI water and blow dried with Nitrogen. Various kinds of nanostructures were produced after plasma etching as shown in Figure 5.6

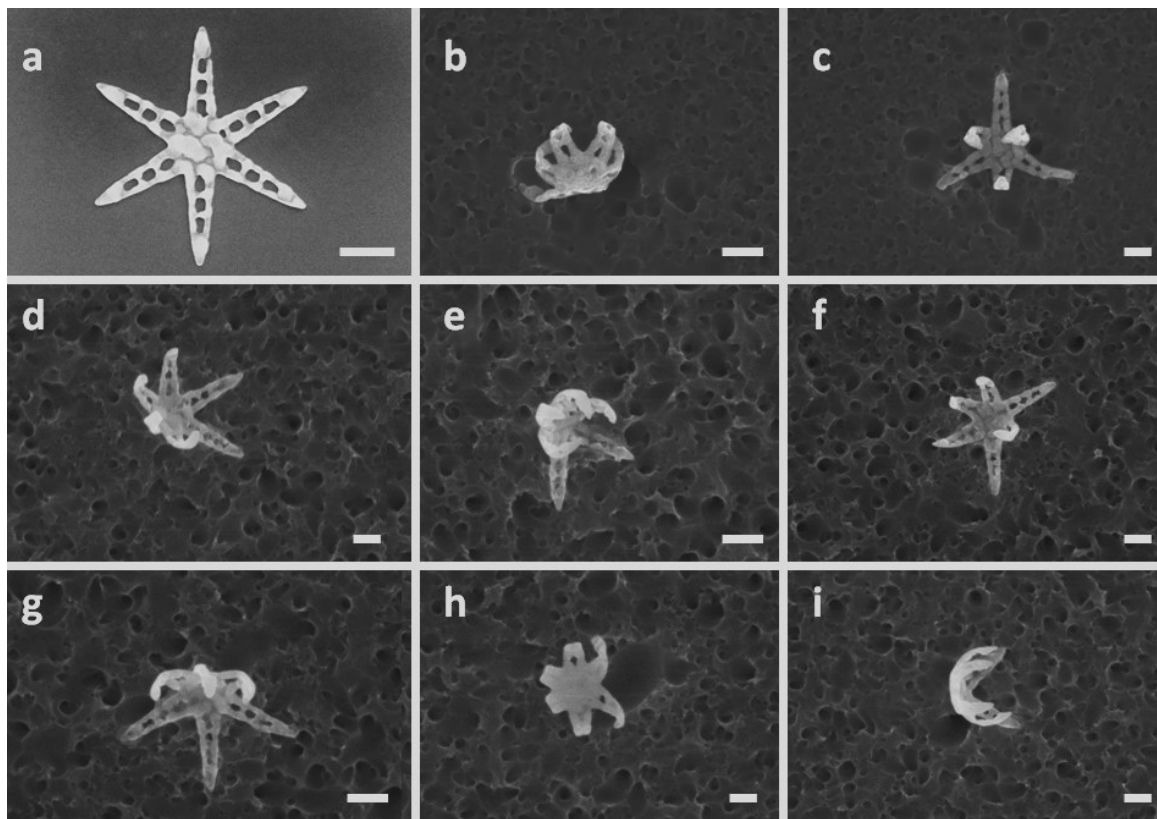


Figure 5.6: Formation of various configuration of nanogripper

5.5.2 Mass Fabrication of structures using nanoimprinting technique

Mold fabrication: For making the initial molds, e-beam patterning was done on PMMA spun wafers as described above and the patterns were developed using MIBK:IPA at 1:3 ratio for 35 secs. A thin chromium layer (10nm) was deposited to act as an etch mask. The mold was created by etching silicon to a depth of 300nm using deep reactive ion etching and then coated with an antisticking layer to prevent adhesion during imprinting. Nanoimprinting was done using the Nanonex Lithography system(Machine details). NXR 1020 resist 6% was spun coated at 800 rpm on Si wafer. The thickness of the resist layer before imprinting was about 380nm. The imprinting step was carried out at 130°C and 210psi pressure for a processing time varying from 1min to 5mins depending on the pattern geometry. The sample was then cooled down and the mold was separated from the sample manually using a micro blade. The imprinted sample was plasma cleaned in oxygen plasma to remove the residual resist layer which was approximately 80nm in thickness. A thin layer of Chromium for adhesion and desired thickness of gold, nickel and tin was patterned on the imprinted sample using liftoff metallization.

The folding of the nanostructures was carried out in Plasma Therm 790 etcher with a CF₄ flow rate of 25sccm and oxygen of 4sccm. The total pressure in the chamber was set to 500mT and the power applied was 50W. Under these conditions, the silicon underneath the nanostructures was etched away releasing the patterns, while at the same time the tin grain coalescence drove the selfassembly of the structures. The structures, if not entirely etched were tethered on the silicon and hence remained on the surface of the silicon for imaging. The structures were imaged using JEOL field emission SEM under 15kV.

5.5.3 Formation of nanobiohybrid devices

5.5.3.1 Bacterial Culture

Escherichia coli strain RP437 were grown in tryptone broth (TB) (10.0 g/liter of Bacto tryptone powder dissolved in 10 mM phosphate buffer) pH 7.3 supplemented with 100 µg/ml ampicillin in a shaker bath at 32°C at 110 rpm. Cultures grown overnight were diluted in the ratio 1:25 into fresh media and grown in the shaker bath until the indicated OD660 (~0.3 to 0.4) value was reached. The cells were then spun down at 4500 rpm for 5mins. Prior to experiments, cells were washed twice in chemotaxis buffer (10 mM phosphate buffer-0.1 mM EDTA-1 µM methionine-10 mM lactic acid). The washed cells were suspended in chemotaxis buffer to an OD660 of approximately 0.1 (approximately 8×10^7 cells per ml).

5.5.3.2 Attachment of structures to bacteria

The fabricated samples were rinsed with DI water to remove any solvent residues. In order to selectively attach bacteria to the structures, the Si surface was passivated using poly(ethylene glycol) (PEG) terminated self-assembled monolayer. The samples were rinsed DI water and ethanol and dried in stream of Nitrogen. Then, 100ul mixed solution of 2.5mM 16-mercaptohexadecanoic acid (MHA) (Sigma Aldrich) in ethanol was placed on the sample and incubated at room temperature for 24 hrs to form the self-assembled layer on Au surface. The unbound thiols were removed by rinsing with pure ethanol. The samples were then rinsed with ultra pure water and dried in Nitrogen before use. The thiol based SAM was treated in solution of 2mg/ml NHS (N-Hydroxysulfosuccinimide) (Sigma Aldrich) and 2mg/ml EDC (1-ethyl-3-(dimethylaminopropyl) carbodiimide hydrochloride) (Sigma Aldrich) . This activated SAM layer was then rinsed with ultra-pure water and dried in N₂ stream and the sample was soaked into the protein solution of

0.2mg/ml goat polyclonal Anti-E. coli antibody (from Abcam) in PBS and incubated at 4°C for 8 hrs to immobilize the proteins onto the SAM. The prepared sample was stored in PBS at 4°C before use. For attachment of the bacteria to the substrate, the samples were incubated with the bacterial culture in motility media at room temperature for 30mins. After incubation the samples were gently rinsed with motility buffer to remove unbound cells.

We used antibody conjugated 40nm diameter gold nanorods of SPR peak at 800nm (C12-40-800-IgG-50) and 25nm diameter with SPR peak at 550nm (C12-25-550-IgG- 50) purchased from NanoPartz (<http://www.nanopartz.com/>). Different concentration of nanorods for the experiment was made by suspending the nanorod solution in motility medium. 50 µl of bacteria were transferred from stock solution into 200 µl of motility medium. Subsequently, 100 µl of nanorod suspension of specified concentration was added to the bacteria suspension. The sample was incubated at room temperature for 10 minutes. During those minutes, bacteria randomly interacted with the nanorods. A 100ul aliquot of the final sample was diluted in 100 µl of motility medium and 10 µl sample was placed in the imaging enclosure. To construct the enclosure, an approximately 100 µm thick PDMS ring was placed on a microscope glass slide. Once the sample is deposited in the chamber, it was covered with a coverslip to prevent evaporation.

5.5.3.3 Motility tracking

Motion of the bacteria-nanorod assembly was recorded by taking sequential images at 16 fps for 5 seconds. 10 µl aliquot of the bacterial suspension was placed in a 10 mm x 10 mm imaging enclosure and were imaged using a Nikon microscope under a 40 × DIC

objective with video imaging (using Optixcam summit series). To track the trajectories of the bacteria–nanorod conjugates, the video was converted to an image series (TIF series) using ImageJ. Bacteria were tracked at their centroid using the semi-automated threshold dependent “track objects” function in Metamorph (Universal Imaging, Downington, PA). The algorithm detects the position of bacteria in successive frames. Tracked bacteria were imaged about 10 mins after mixing with extract to ensure this analysis included only bacteria moving at steady-state. The trajectories were plotted and parameters such as the mean speed were calculated using tracking software. We limited our analysis to bacteria from a single population observed all on the same day to eliminate, as much as possible, variations in our bacterial speed measurements that arise from experimental variation (e.g. differences in extract dilutions, temperature, etc). Bacteria used in this experiment were highly motile (average speed of approximately 30 $\mu\text{m/s}$). Many of them moved in and out of the observation window during the time period of the experiment. The data is based on the bacteria that stayed within the observation window and were tracked the entire experiment.

5.6 Summary

In summary, our concept of interfacing engineered multifunctional nanoobjects with motile bacterial cells synergistically combines the functionalities offered by both groups to result in bionic hybrids possessing unique and advanced capabilities. Through such an interface, the biological motors of motile bacteria provide actuation to the nanoengineered tools and devices. In addition, the engineered functionalities of the cell surface interfaced nanostructures imparts additional control functions to the biological microorganism as demonstrated by the example of bringing forth control to their motile

behavior *via* interfaced plasmonic nanoantennas. The result of this biotic-abiotic conjugate at the nanoscale is the realization of hybrid systems with unique capabilities, as validated by our demonstrative example of remotely controlling the bacterial-nanostructure hybrids *via* plasmonic nanoantenna. This generic concept of integrating engineered nanoscale devices and structures with motile bacterial cells thus represents a new, general strategy in creating a functional integration of engineered nanoobjects with biological systems to create microrobots that can perform tasks that are currently deemed impossible

Chapter 6

Conclusions and Future Outlook

6.1 Summary of Main Conclusions

This thesis presented our investigations in the development of novel approaches for achieving parallel and cost-effective patterning and 3D assembly at the nanoscale and our explorations of their potential applications. Specifically, we presented two new approaches that we developed for the spontaneous curving of nanostructures using grain reflow and creation of nanopatterned channels, wells, and semiconducting conical nanopores using metal assisted plasma etching process.

Chapter 1 presented the motivations and significance of achieving 3D assembly and patterning at the nanoscale, addressed the challenges and limitations of the current nanoengineering tools and discussed the already existing strategies to overcome these limitations. A few examples of the surface patterned 3D nanostructures from nature and the self-assembly strategy resulting in their formation is presented. Next, an overview of artificial self-assembly strategies are presented starting with the closest approach in mimicking natural self-assembly by the use of biomolecular interactions as the driving force of the assembly. Finally, the approach that we developed for the creation of 3D nanostructures by the curving of nanolithographically patterned 2D geometries and 3D assembly of hinged nanopanels using plasma induced grain reflow is introduced.

Chapter 2 presented in detail our work on the development of a parallel and cost effective method for the creation of surface patterned 3D nanostructures and an in-depth view of the underlying phenomenon of plasma induced grain reflow process. Two strategies for the creation of nanoscale 3D structures was presented in detail: curving and bending hingeless structures patterned using single layer lithography process and assembly of hinged structures patterned using multiple lithography processes. A major highlight of these strategies was that they leveraged on the well-developed nanolithographic techniques such as e-beam and nanoimprint lithography. Demonstrative examples of the creation of various geometries of 3D nanostructures including nanotubes, Venus-flytrap like, nanogrippers and nanoflowers with sizes as small as 100 nm while simultaneously incorporating specific and lithographically defined surface patterns were presented. Also, the creation of surface patterned nanobox structures were presented using the grain coalescence based 3D assembly of lithographically patterned hinged nanopanels. Further, the ongoing work in understanding in detail the material property changes that occurs during the folding process using EDX, EBSD and HRTEM analysis was presented. Finally, as the means of mass producing of 3D nanostructures, nanoimprint lithography technique is utilized and the formation of various 3d structures using nanoimprint patterned geometries is demonstrated.

In third chapter, we discussed about the formation nanostructured patterns in silicon using catalytic etching assisted by the presence of noble metal particles. We demonstrated the formation of nanohole arrays using Metal assisted chemical etching (MaCE) and our newly discovered process: metal assisted plasma etching (MaPE). The formation of gold nanoparticles coated microfluidic structures is demonstrated using the

MaPE process as the plasma etch rate of Si was enhanced in the vicinity of 10-100 nm thick Au patterns. We also demonstrated the formation of wells or channels coated with 20-30 nm sized Au NPs. The methodology provides versatility in the types of structures that can be formed by varying the shape and dimensions of the Au patterns and the etch time. Further, the applications of Au NP coated Si microwells for bioanalytical science is explored by the selective assembly of antibodies within them using thiol chemistry.

In the fourth chapter, we discussed the formation of conical nanopores using MaPE process. By varying the process parameters and gold nanoparticle sizes, formation of various pore geometries and cone angles were demonstrated on planar and 3D silicon crystals. Additionally, ionic transports through the pores were investigated. It was found that the pores behave as ion-current rectifiers with high on-off ratios. By applying voltage on the pores, it was found that these pores could function as ionic switches and the rectification ratios can be enhanced by a fraction of 100. Further, voltage gated control over protein transport through these pores was demonstrated which is of importance in lab-on-a-chip devices and biomolecular separations.

Chapter 5 presented our investigations on the use of 3D nanostructures in the formation of nanobionic devices. The engineered functional 3D nano objects were directly interfaced with motile bacterial cells enabling the creation of multi-functional ‘nanostructure-bacteria hybrid devices’. Such an interfacing of the nanoengineered multifunctional structures with motile bacterial cells results in an outcome that is in general two-fold- 1. It renders propulsion to the nanostructures and thereby enables to utilize their full potential. 2. It enables a way to remotely control the bacterial motion by the nanostructures acting as antenna for control signals. We investigated the effect of

plasmonically heating the bacterial cells *via* the interfaced nanoantennas. It was found that the bacterial cells undergo characteristic changes in their run and tumble behaviors at various intensities corresponding to their plasmonic resonance frequencies. As a demonstration of the use of such biohybrid systems, we investigated the ability to control their motile behavior in an engineered microcappillary network.

6.2 Outlook

Overall this thesis presented considerable advances in the development of 3D nanostructures with surface patterns with a variety of potential technological applications. The approaches that we developed using plasma induced grain coalescence and noble metal assisted catalytic etching can serve as a general strategy to create 3D nanostructured devices and complex multifunctional architectures. The 3D nanoparticles created could display novel optical properties, such as unique plasmon resonances. These particles can be used as encapsulants and since could be designed such that there is specific surface patterning, a well-defined subsequent molecular patterning using self-assembled monolayers for targeted therapeutics can also be envisioned. Further, the particles also represent an attractive building blocks for hierarchical self-assembly of nanostructured three-dimensional devices.

6.2.1 Actuation of nanostructures

One direction for interesting future work would be in engineering approaches for providing actuation for the nanoengineered structures. Reversible actuation of 3D nanostructures could pave the way to the formation of automatic robotic systems. One

such example is demonstrated below. As the folded structures are heated with electron beam, they were seen to be set in motion as seen in the figure (Fig 6.1 c , d).

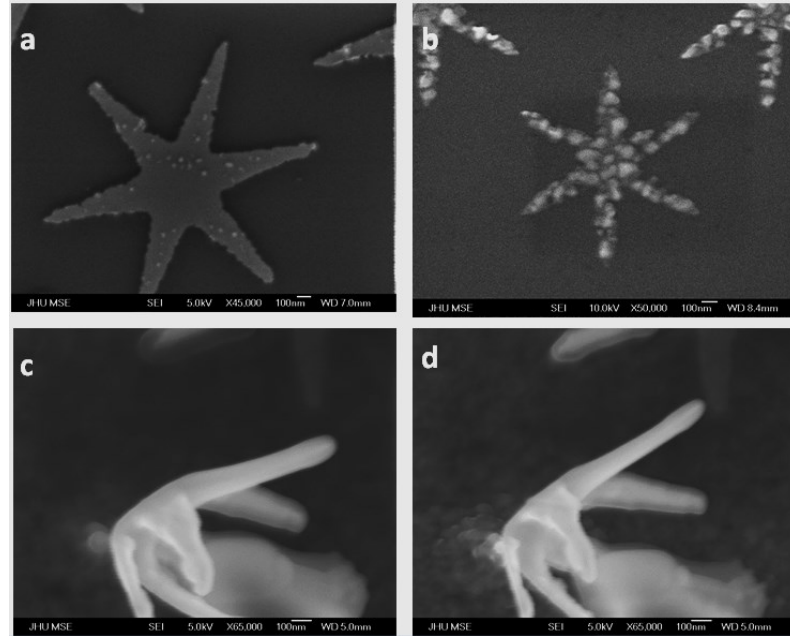


Figure 6.1: Actuation of nanostructures with electron beam. (a,b) SEM images of nanogrippers as they are patterned (c,d) SEM image of the same folded nanogripper during irradiation with electron beam for approximately 1 sec.

With regards to the work on the development of conical nanopore our work opens up mainly two new opportunities especially in the formation of ionic logic gates and in energy harvesting devices as detailed below.

6.2.2 Application of semiconducting conical nanopores

6.2.2.1 Ionic Logic Gates

Developing ionic circuits for manipulating and probing biomolecules in solution phase is very important. To date, there has been no logic nanodevices demonstrated capable of information processing like biological ion channels. Work has been done to regulate the

nanopore conductance using a dielectric film deposited on a metallic surface inside the pore¹²³, however gating a Si conical nanopore offers further advantages with regard to integrating circuit components and semiconductor fabrication processes. Our work has demonstrated that Silicon (Si) conical nanopores show varying conductance levels that can be tuned externally by voltage gating. We can also explore the utilization of these gated Si conical nanopores to form logic gate schemes where binary and multivalued logical functions can be implemented in ionic circuits through electrical inputs.

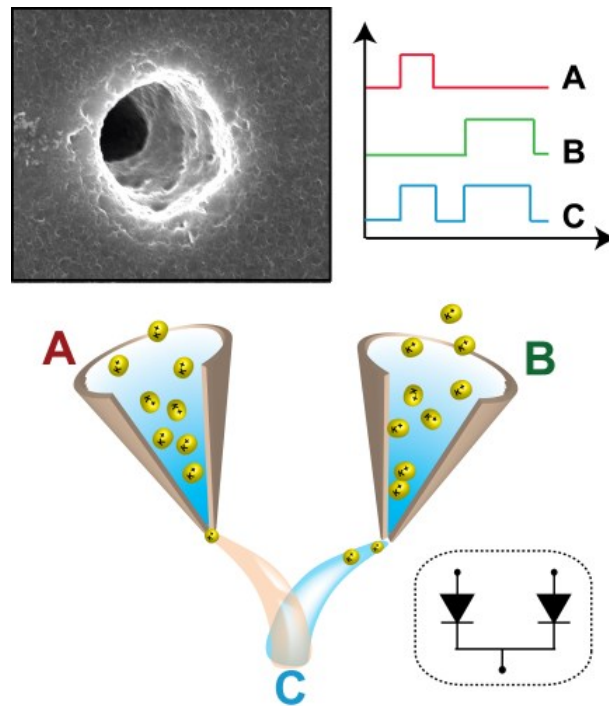


Figure 6.2: Potential applications of Si conical nanopores in the creation of Ionic logic circuits.

6.2.2.2 Energy harvesting

In addition, it can also be perceived that such conical pore membrane can be used in electro-kinetic energy harvesting applications. Investigation of cheaper and efficient way

to harvest energy with minimal cost is important in many aspects. One such way to harvest energy relies on the extraordinary transport properties observed at nanopores, due to the unusual properties of fluids confined to such molecularly narrow pores. An example of one such phenomenon is the water flow observed in carbon nanotubes with nanometre-scale diameters, where water flow exceeds expectations of macroscopic hydrodynamics by orders of magnitude^{124,125}.

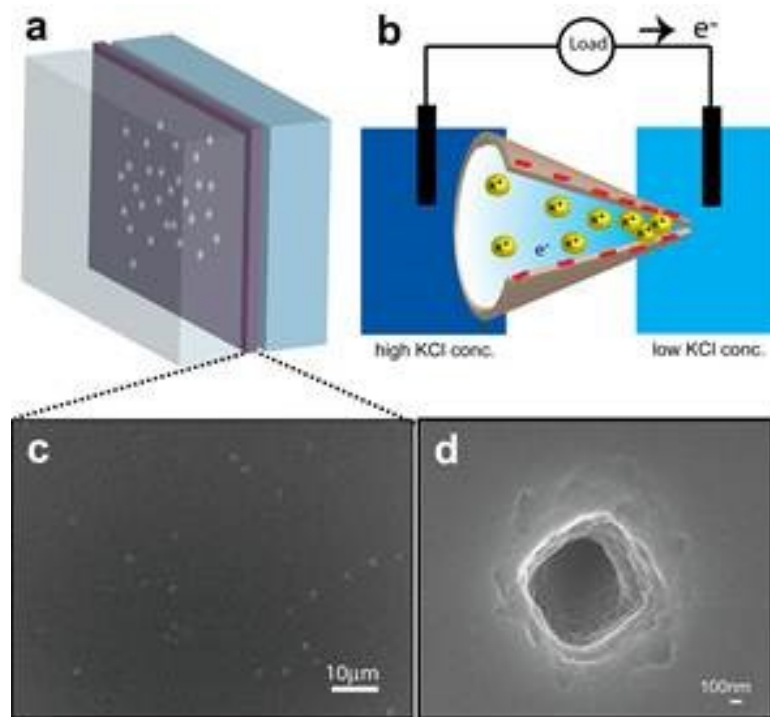


Figure 6.3: Schematic illustration of the future outlook on the use of semiconducting conical nanopores fabricated using MaPE process for energy harvesting.

As a result of their unusual transport properties, nanopore membranes have great potential for applications such as water desalination devices, hydrogen fuel cells and even in capacitors and sensors where the length dependent variation of dielectric constant of nanoconfined water molecules can be used¹²⁶⁻¹²⁹. It is known that strong attraction

between water molecules due to hydrogen bonding makes their interaction with nonpolar substances unfavorable and polar substance favorable and it has been theoretically predicted that water confined in a hydrophobic pore spontaneously evaporates when the pore dimension is sufficiently small¹³⁰. Nanofluidic energy harvesting systems using ion-separation^{131,132} allows us to integrate this phenomenon into semiconductive membranes. Although the chemical concentration gradient that provides Gibbs free energy to work¹³³ has been used to recover free energy from mixing, a thorough understanding of the power generation mechanism and ion-transport is lacking especially in ion-exchange membranes^{134,135}. Apart from the free energy of mixing, energy recovery has also been proposed through electrokinetic effects in ultrafine capillaries¹³⁶. According to the energy conversion using electrokinetic behavior, when an axial pressure gradient is impressed on fluid electrolyte in an ultrafine capillary tube and the electrical current is restricted, an electrical potential difference can be obtained. Using this phenomenon, we can investigate the use of silicon conical nanoporous membrane in energy generation by using reverse conversion of pumping into electrical power. In these silicon conical nanopores, the surface of the pore is negatively charged as a result of the fluorine plasma etching process. Hence, cations are preferentially transported with respect to anions making the membranes ion-selective. Using this ion-selective property of silicon nanopore, we explore the use of these membranes for energy generation (Fig. 6.3). Here, the concentration gradient imposed on either side of the silicon membrane leads to the spontaneous diffusion of ions across the gradient. Utilizing the ion selective membrane, part of the Gibbs free energy of mixing can be converted to usable energy through the net diffusion current as shown in Figure 6.3. The resulting current can be applied to an

external load such as resistor as shown. The power density depends on the number density of nanopores on the silicon membrane. By increasing the pore density, the power can be raised higher in magnitude than typical ion-exchange membranes. Previous theoretical studies have shown that the power generation and efficiency can be optimized by varying the surface charge density and pore geometries. Therefore this work also can be the utilization of silicon conical nanoporous membrane to generate electrical power through ion diffusion. There are two main advantages to such a nanoporous membrane system. Primarily, the substrate material, Si holds great importance as it is well compatible with the semiconductor processing techniques. Secondly, the process of making conical nanopores in silicon is a simple and one step etching process, which only requires the coating of the surface with Au NPs. The electrolyte gradient across the Si nanoporous membrane can provide the nanofluidic power source.

In summary, the advances in the development of multifunctional 3D nanostructured devices described in this thesis are indicative of the fascinating and revolutionary potential of our approaches. Regardless of the directions future work may take, the results presented in this thesis provide a strong motivation for continued and expanded efforts in the design and development multifunctional nanoscale 3D devices and structures.

References

- 1 Feynman, R. P. There's plenty of room at the bottom. *Journal of Microelectromechanical Systems* **1**, 60-66 (1992).
- 2 Hu, S., Cho, J-Hyun, Gracias, D. H. *Building 3D Nanostructured Devices by Self-Assembly*. (Springer New York, 2009).
- 3 Rolland, J. P. *et al.* Direct fabrication and harvesting of monodisperse, shape-specific nanobiomaterials. *Journal of the American Chemical Society* **127**, 10096-10100 (2005).
- 4 Aizenberg, J. & Hendler, G. Designing efficient microlens arrays: lessons from Nature. *Journal of Materials Chemistry* **14**, 2066-2072 (2004).
- 5 Ensikat, H. J., Ditsche-Kuru, P., Neinhuis, C. & Barthlott, W. Superhydrophobicity in perfection: The outstanding properties of the lotus leaf. *Beilstein Journal of Nanotechnology* **2**, 152-161 (2011).
- 6 Meyers, M. A., Chen, P. Y., Lin, A. Y. M. & Seki, Y. Biological materials: Structure and mechanical properties. *Progress in Materials Science* **53**, 1-206 (2008).
- 7 Meyers, M. A., Chen, P.-Y., Lin, A. Y.-M. & Seki, Y. Biological materials: Structure and mechanical properties. *Progress in Materials Science* **53**, 1-206 (2008).
- 8 Cölfen, H. & Mann, S. Higher-order organization by mesoscale self-assembly and transformation of hybrid nanostructures. *Angewandte Chemie - International Edition* **42**, 2350-2365 (2003).

- 9 Niece, K. L., Hartgerink, J. D., Donners, J. J. J. M. & Stupp, S. I. Self-assembly combining two bioactive peptide-amphiphile molecules into nanofibers by electrostatic attraction. *Journal of the American Chemical Society* **125**, 7146-7147 (2003).
- 10 Padilla, J. E., Colovos, C. & Yeates, T. O. Nanohedra: Using symmetry to design self assembling protein cages, layers, crystals, and filaments. *Proceedings of the National Academy of Sciences of the United States of America* **98**, 2217-2221 (2001).
- 11 McMillan, R. A. *et al.* Ordered nanoparticle arrays formed on engineered chaperonin protein templates. *Nature Materials* **1**, 247-252 (2002).
- 12 Ayyagari, M. S. *et al.* Molecular assembly of proteins and conjugated polymers: Toward development of biosensors. *Biotechnology and Bioengineering* **45**, 116-121 (1995).
- 13 Caswell, K. K., Wilson, J. N., Bunz, U. H. F. & Murphy, C. J. Preferential End-to-End Assembly of Gold Nanorods by Biotin–Streptavidin Connectors. *Journal of the American Chemical Society* **125**, 13914-13915 (2003).
- 14 Mirkin, C. A. Invited contribution from recipient of ACS award in pure chemistry: Programming the assembly of two- and three-dimensional architectures with DNA and nanoscale inorganic building blocks. *Inorganic Chemistry* **39**, 2258-2272 (2000).
- 15 Chen, J. & Seeman, N. C. Synthesis from DNA of a molecule with the connectivity of a cube. *Nature* **350**, 631-633 (1991).

- 16 Goodman, R. P. *et al.* Chemistry: Rapid chiral assembly of rigid DNA building blocks for molecular nanofabrication. *Science* **310**, 1661-1665 (2005).
- 17 Erben, C. M., Goodman, R. P. & Turberfield, A. J. Single-molecule protein encapsulation in a rigid DNA cage. *Angewandte Chemie - International Edition* **45**, 7414-7417 (2006).
- 18 Goodman, R. P. *et al.* Reconfigurable, braced, three-dimensional DNA nanostructures. *Nature Nanotechnology* **3**, 93-96 (2008).
- 19 Rothemund, P. W. K. Folding DNA to create nanoscale shapes and patterns. *Nature* **440**, 297-302 (2006).
- 20 Andersen, E. S. *et al.* Self-assembly of a nanoscale DNA box with a controllable lid. *Nature* **459**, 73-76 (2009).
- 21 He, Y. *et al.* Hierarchical self-assembly of DNA into symmetric supramolecular polyhedra. *Nature* **452**, 198-201 (2008).
- 22 Mucic, R. C., Storhoff, J. J., Mirkin, C. A. & Letsinger, R. L. DNA-directed synthesis of binary nanoparticle network materials [5]. *Journal of the American Chemical Society* **120**, 12674-12675 (1998).
- 23 Chowdhury, D. Combination of self-assembly and nanolithography as an effective nanofabrication methodology for device realization. *Current Science* **96**, 923-932 (2009).
- 24 Whitesides, G. M. & Grzybowski, B. Self-Assembly at All Scales. *Science* **295**, 2418-2421 (2002).
- 25 Wu, Y. *et al.* Composite mesostructures by nano-confinement. *Nature Materials* **3**, 816-822 (2004).

- 26 Rycenga, M., McLellan, J. M. & Xia, Y. Controlling the Assembly of Silver Nanocubes through Selective Functionalization of Their Faces. *Advanced Materials* **20**, 2416-2420 (2008).
- 27 Gu, Z., Ye, H., Smirnova, D., Small, D. & Gracias, D. H. Reflow and electrical characteristics of nanoscale solder. *Small* **2**, 225-229 (2006).
- 28 Gu, Z., Chen, Y. & Gracias, D. H. Surface tension driven self-assembly of bundles and networks of 200 nm diameter rods using a polymerizable adhesive. *Langmuir* **20**, 11308-11311 (2004).
- 29 Leong, T. G., Zarafshar, A. M. & Gracias, D. H. Three-dimensional fabrication at small size scales. *Small* **6**, 792-806 (2010).
- 30 Schmidt, O. G. & Eberl, K. Thin solid films roll up into nanotubes. *Nature* **410**, 168 (2001).
- 31 Prinz, V. Y. Precise, molecularly thin semiconductor shells: From nanotubes to nanocorrugated quantum systems. *Physica Status Solidi (B) Basic Research* **243**, 3333-3339 (2006).
- 32 Prinz, V. Y. Precise semiconductor nanotubes and nanocorrugated quantum systems. *Physica E: Low-Dimensional Systems and Nanostructures* **24**, 54-62 (2004).
- 33 Deneke, C., Müller, C., Jin-Phillipp, N. Y. & Schmidt, O. G. Diameter scalability of rolled-up In(Ga)As/GaAs nanotubes. *Semiconductor Science and Technology* **17**, 1278-1281 (2002).
- 34 Vaccaro, P. O., Kubota, K. & Aida, T. Strain-driven self-positioning of micromachined structures. *Applied Physics Letters* **78**, 2852-2854 (2001).

- 35 Tsui, Y. C. & Clyne, T. W. An analytical model for predicting residual stresses in progressively deposited coatings: Part 1: Planar geometry. *Thin Solid Films* **306**, 23-33 (1997).
- 36 Cho, J.-H., Azam, A. & Gracias, D. H. Three Dimensional Nanofabrication Using Surface Forces†. *Langmuir* **26**, 16534-16539 (2010).
- 37 Charles, R. M. Template synthesis of polymeric and metal microtubules. *Adv. Mater.* **3**, 457-459 (1991).
- 38 Srinivas, G. & Pitera, J. W. Soft patchy nanoparticles from solution-phase self-assembly of binary diblock copolymers. *Nano Lett.* **8**, 611-618 (2008).
- 39 Zhang, Z. & Glotzer, S. C. Self-assembly of patchy particles. *Nano Lett.* **4**, 1407-1413 (2004).
- 40 Bowden, N., Choi, I. S., Grzybowski, B. A. & Whitesides, G. M. Mesoscale Self-Assembly of Hexagonal Plates Using Lateral Capillary Forces: Synthesis Using the “Capillary Bond”. *Journal of the American Chemical Society* **121**, 5373-5391 (1999).
- 41 Syms, R. R. A., Yeatman, E. M., Bright, V. M. & Whitesides, G. M. Surface tension-powered self-assembly of microstructures - The state-of-the-art. *Journal of Microelectromechanical Systems* **12**, 387-417 (2003).
- 42 Py, C. *et al.* Capillary Origami: Spontaneous Wrapping of a Droplet with an Elastic Sheet. *Physical Review Letters* **98**, 156103 (2007).
- 43 Honschoten, J. W. v. *et al.* Elastocapillary fabrication of three-dimensional microstructures. *Applied Physics Letters* **97**, 014103 (2010).

- 44 Cho, J. H., James, T. & Gracias, D. H. Curving nanostructures using extrinsic stress. *Advanced Materials* **22**, 2320-2324 (2010).
- 45 Cho, J. H. & Gracias, D. H. Self-Assembly of lithographically patterned nanoparticles. *Nano Letters* **9**, 4049-4052 (2009).
- 46 Cho, J.-H., Azam, A. & Gracias, D. H. Three Dimensional Nanofabrication Using Surface Forces *Langmuir* (2010).
- 47 Stoney, G. G. The tension of metallic films deposited by electrolysis. *Proc. R. Soc. London, Ser. A* **82**, 172-175 (1909).
- 48 Nix, W. D. Mechanical properties of thin films. *Metall. Trans. A* **20**, 2217-2245 (1989).
- 49 Freund, L. B. & Suresh, S. *Thin Film Materials: Stress, Defect Formation and Surface Evolution* (Cambridge University Press, 2003).
- 50 Timothy, G. L., Aasiyeh, M. Z. & David, H. G. Three-Dimensional Fabrication at Small Size Scales. *Small* **6**, 792-806 (2008).
- 51 Gimi, B. *et al.* Self-Assembled Three Dimensional Radio Frequency (RF) Shielded Containers for Cell Encapsulation. *Biomed. Microdevices* **7**, 341-345 (2005).
- 52 Leong, T. G., Lester, P. A., Koh, T. L., Call, E. K. & Gracias, D. H. Surface tension-driven self-folding polyhedra. *Langmuir* **23**, 8747-8751 (2007).
- 53 Timothy, G. L., Aasiyeh, M. Z. & David, H. G. Three-Dimensional Fabrication at Small Size Scales. *Small* **6**, 792-806 (2010).

- 54 Hildreth, O. J., Lin, W. & Wong, C. P. Effect of catalyst shape and etchant composition on etching direction in metal-assisted chemical etching of silicon to fabricate 3D nanostructures. *ACS Nano* **3**, 4033-4042 (2009).
- 55 Lee, C. L., Tsujino, K., Kanda, Y., Ikeda, S. & Matsumura, M. Pore formation in silicon by wet etching using micrometre-sized metal particles as catalysts. *Journal of Materials Chemistry* **18**, 1015-1020 (2008).
- 56 Tsujino, K. & Matsumura, M. Boring deep cylindrical nanoholes in silicon using silver nanoparticles as a catalyst. *Advanced Materials* **17**, 1045-1047 (2005).
- 57 Coburn, J. W. & Winters, H. F. PLASMA ETCHING - A DISCUSSION OF MECHANISMS. *J Vac Sci Technol* **16**, 391-403 (1979).
- 58 Fedynyshyn, T. H., Grynkewich, G. W., Chen, B. A. & Ma, T. P. Effect of metal masks on the plasma etch rate of silicon. *J. Electrochem. Soc.* **136**, 1799-1804 (1989).
- 59 Kataoka, Y., Shinmura, T. & Kanoh, M. Improvement in downflow etching rate using Au as a catalyst. *Journal of Vacuum Science and Technology A: Vacuum, Surfaces and Films* **18**, 388-392 (2000).
- 60 Fedynyshyn, T. H., Grynkewich, G. W. & Dumas, R. H. MASK DEPENDENT ETCH RATES III: THE EFFECT OF A SILVER ETCH MASK ON THE PLASMA ETCH RATE OF SILICON. *J. Electrochem. Soc.* **135**, 268-269 (1988).
- 61 Fridman, A. *Plasma Chemistry* (2008).
- 62 Fridman, A. & Kennedy, L. A. *Plasma Physics and Engineering* (2004).

- 63 Kelly, J. J., Xia, X. H., Ashruf, C. M. A. & French, P. J. Galvanic cell formation: a review of approaches to silicon etching for sensor fabrication. *IEEE Sensors Journal* **1**, 127-142 (2001).
- 64 Chartier, C., Bastide, S. & L vy-Ci ment, C. Metal-assisted chemical etching of silicon in HF-H₂O₂. *Electrochimica Acta* **53**, 5509-5516 (2008).
- 65 Andersson, H. & Van Den Berg, A. Microfabrication and microfluidics for tissue engineering: State of the art and future opportunities. *Lab on a Chip - Miniaturisation for Chemistry and Biology* **4**, 98-103 (2004).
- 66 Reyes, D. R., Iossifidis, D., Auroux, P. A. & Manz, A. Micro total analysis systems. 1. Introduction, theory, and technology. *Anal. Chem.* **74**, 2623-2636 (2002).
- 67 Zhu, H. & Snyder, M. Protein arrays and microarrays. *Curr. Opin. Chem. Biol.* **5**, 40-45 (2001).
- 68 Charnley, M., Textor, M., Khademhosseini, A. & Lutolf, M. P. Integration column: microwell arrays for mammalian cell culture. *Integrative Biology* **1**, 625-634 (2009).
- 69 Senaratne, W., Andruzzi, L. & Ober, C. K. Self-Assembled Monolayers and Polymer Brushes in Biotechnology: Current Applications and Future Perspectives. *Biomacromolecules* **6**, 2427-2448 (2005).
- 70 Mrksich, M. & Whitesides, G. M. Using Self-Assembled Monolayers to Understand the Interactions of Man-made Surfaces with Proteins and Cells. *Annu. Rev. Biophys. Biomol. Struct.* **25**, 55-78 (1996).

- 71 Eustis, S. & El-Sayed, M. A. Why gold nanoparticles are more precious than pretty gold: Noble metal surface plasmon resonance and its enhancement of the radiative and nonradiative properties of nanocrystals of different shapes. *Chem. Soc. Rev.* **35**, 209-217 (2006).
- 72 He, L. *et al.* Colloidal Au-enhanced surface plasmon resonance for ultrasensitive detection of DNA hybridization. *J. Am. Chem. Soc.* **122**, 9071-9077 (2000).
- 73 Wang, L. *et al.* Au NPs-enhanced surface plasmon resonance for sensitive detection of mercury(II) ions. *Biosens. Bioelectron.* **25**, 2622-2626.
- 74 Yap, F. L. & Zhang, Y. Protein and cell micropatterning and its integration with micro/nanoparticles assembly. *Biosens. Bioelectron.* **22**, 775-788 (2007).
- 75 Luo, L.-B. *et al.* Surface-Enhanced Raman Scattering from Uniform Gold and Silver Nanoparticle-Coated Substrates. *The Journal of Physical Chemistry C* **113**, 9191-9196 (2009).
- 76 Ahmed, S. & Ryan, K. M. Close-packed gold-nanocrystal assemblies deposited with complete selectivity into lithographic trenches. *Adv. Mater.* **20**, 4745-4750 (2008).
- 77 Randhawa, J. S., Bernfeld, A., Keung, M., Volinsky, A. A. & Gracias, D. H. Concentric ring pattern formation in heated chromium-gold thin films on silicon. *Appl. Phys. Lett.* **92** (2008).
- 78 Magunov, A. N. Determining the heat of a surface plasmochemical reaction by scanning calorimetry. *Instruments and Experimental Techniques* **43**, 706-712 (2000).

- 79 Bokhonov, B. & Korchagin, M. In situ investigation of stage of the formation of eutectic alloys in Si-Au and Si-Al systems. *Journal of Alloys and Compounds* **312**, 238-250 (2000).
- 80 Baumann, F. H. & Schr  ter, W. Precipitation of gold into metastable gold silicide in silicon. *Physical Review B* **43**, 6510-6519 (1991).
- 81 Lieber, C. M. Nanoscale science and technology: Building a big future from small things. *MRS Bulletin* **28**, 486-491 (2003).
- 82 Nelson, B. J., Kaliakatsos, I. K. & Abbott, J. J. Microrobots for minimally invasive medicine. *Annu Rev Biomed Eng* **12**, 55-85 (2010).
- 83 Cho, J. H., James, T. & Gracias, D. H.
- 84 Cho, J. H., Datta, D., Park, S. Y., Shenoy, V. B. & Gracias, D. H. Plastic deformation drives wrinkling, saddling, and wedging of annular bilayer nanostructures. *Nano Letters* **10**, 5098-5102 (2010).
- 85 Cho, J. H., Azam, A. & Gracias, D. H. Three dimensional nanofabrication using surface forces. *Langmuir* **26**, 16534-16539 (2010).
- 86 Magdanz, V., Sanchez, S. & Schmidt, O. G. Development of a Sperm-Flagella Driven Micro-Bio-Robot. *Advanced Materials* **25**, 6581-6588 (2013).
- 87 Ozin, G. A., Manners, I., Fournier-Bidoz, S. & Arsenault, A. Dream nanomachines. *Advanced Materials* **17**, 3011-3018 (2005).
- 88 Paxton, W. F., Sundararajan, S., Mallouk, T. E. & Sen, A. Chemical locomotion. *Angewandte Chemie - International Edition* **45**, 5420-5429 (2006).

- 89 Fernandes, R., Zuniga, M., Sassine, F. R., Karakoy, M. & Gracias, D. H. Enabling cargo-carrying bacteria via surface attachment and triggered release. *Small* **7**, 588-592 (2011).
- 90 Silverman, M. & Simon, M. Flagellar rotation and the mechanism of bacterial motility. *Nature* **249**, 73-74 (1974).
- 91 Blair, D. F. How bacteria sense and swim. *Annual Review of Microbiology* **49**, 489-522 (1995).
- 92 Berg, H. C. Motile behavior of bacteria. *Physics Today* **53**, 24-29 (2000).
- 93 Berg, H. C. Vol. 72 19-54 (2003).
- 94 Eisenbach, M. & Caplan, S. R. Bacterial chemotaxis: Unsolved mystery of the flagellar switch. *Current Biology* **8**, R444-R446 (1998).
- 95 Scharf, B. E., Fahrner, K. A., Turner, L. & Berg, H. C. Control of direction of flagellar rotation in bacterial chemotaxis. *Proceedings of the National Academy of Sciences of the United States of America* **95**, 201-206 (1998).
- 96 Critchley, R. J. *et al.* Potential therapeutic applications of recombinant, invasive *E. coli*. *Gene Therapy* **11**, 1224-1233 (2004).
- 97 Kasinskas, R. W. & Forbes, N. S. *Salmonella typhimurium* specifically chemotax and proliferate in heterogeneous tumor tissue in vitro. *Biotechnology and Bioengineering* **94**, 710-721 (2006).
- 98 Vassaux, G., Nitcheu, J., Jezzard, S. & Lemoine, N. R. Bacterial gene therapy strategies. *Journal of Pathology* **208**, 290-298 (2006).
- 99 Akin, D. *et al.* Bacteria-mediated delivery of nanoparticles and cargo into cells. *Nat Nano* **2**, 441-449 (2007).

- 100 Sokolov, A., Apodaca, M. M., Grzybowski, B. A. & Aranson, I. S. Swimming bacteria power microscopic gears. *Proceedings of the National Academy of Sciences* **107**, 969-974.
- 101 Steager, E. *et al.* Control of microfabricated structures powered by flagellated bacteria using phototaxis. *Applied Physics Letters* **90** (2007).
- 102 Weibel, D. B. *et al.* Microoxen: Microorganisms to move microscale loads. *Proceedings of the National Academy of Sciences of the United States of America* **102**, 11963-11967 (2005).
- 103 Garnett, E. C. *et al.* Self-limited plasmonic welding of silver nanowire junctions. *Nature Materials* **11**, 241-249 (2012).
- 104 Govorov, A. O. & Richardson, H. H. Generating heat with metal nanoparticles. *Nano Today* **2**, 30-38 (2007).
- 105 Zheng, Y. B., Kiraly, B., Weiss, P. S. & Huang, T. J. Molecular plasmonics for biology and nanomedicine. *Nanomedicine* **7**, 751-770 (2012).
- 106 Biagioni, P., Huang, J. S. & Hecht, B. Nanoantennas for visible and infrared radiation. *Reports on Progress in Physics* **75** (2012).
- 107 Govorov, A. O. *et al.* Gold nanoparticle ensembles as heaters and actuators: Melting and collective plasmon resonances. *Nanoscale Research Letters* **1**, 84-90 (2006).
- 108 Rodríguez-Oliveros, R. & Sánchez-Gil, J. A. Gold nanostars as thermoplasmonic nanoparticles for optical heating. *Optics Express* **20**, 621-626 (2012).

- 109 Von Maltzahn, G. *et al.* Computationally guided photothermal tumor therapy using long-circulating gold nanorod antennas. *Cancer Research* **69**, 3892-3900 (2009).
- 110 Block, S. M., Segall, J. E. & Berg, H. C. Impulse responses in bacterial chemotaxis. *Cell* **31**, 215-226 (1982).
- 111 Tisa, L. S., Olivera, B. M. & Adler, J. Inhibition of *Escherichia coli* chemotaxis by ω -conotoxin, a calcium ion channel blocker. *Journal of Bacteriology* **175**, 1235-1238 (1993).
- 112 Tisa, L. S. & Adler, J. Calcium ions are involved in *Escherichia coli* chemotaxis. *Proceedings of the National Academy of Sciences of the United States of America* **89**, 11804-11808 (1992).
- 113 Shi, W., Lentz, M. J. & Adler, J. Behavioral responses of *Escherichia coli* to changes in temperature caused by electric shock. *Journal of Bacteriology* **175**, 5785-5790 (1993).
- 114 Macnab, R. & Koshland Jr, D. E. Bacterial motility and chemotaxis: light induced tumbling response and visualization of individual flagella. *Journal of Molecular Biology* **84**, 399-406 (1974).
- 115 Yang, H., Inokuchi, H. & Adler, J. Phototaxis away from blue light by an *Escherichia coli* mutant accumulating protoporphyrin IX. *Proceedings of the National Academy of Sciences of the United States of America* **92**, 7332-7336 (1995).
- 116 Adler, J. & Templeton, B. The effect of environmental conditions on the motility of *Escherichia coli*. *Journal of General Microbiology* **46**, 175-184 (1967).

- 117 Turner, L., Caplan, S. R. & Berg, H. C. Temperature-induced switching of the bacterial flagellar motor. *Biophysical Journal* **71**, 2227-2233 (1996).
- 118 Maeda, K., Imae, Y., Shioi, J. I. & Oosawa, F. Effect of temperature on motility and chemotaxis of *Escherichia coli*. *Journal of Bacteriology* **127**, 1039-1046 (1976).
- 119 Alon, U. *et al.* Response regulator output in bacterial chemotaxis. *EMBO Journal* **17**, 4238-4248 (1998).
- 120 Paster, E. & Ryu, W. S. The thermal impulse response of *Escherichia coli*. *Proceedings of the National Academy of Sciences of the United States of America* **105**, 5373-5377 (2008).
- 121 Sager, B. M., Sekelsky, J. J., Matsumura, P. & Adler, J. Use of a computer to assay motility in bacteria. *Analytical Biochemistry* **173**, 271-277 (1988).
- 122 Larsen, S. H., Reader, R. W., Kort, E. N., Tso, W. W. & Adler, J. Change in direction of flagellar rotation is the basis of the chemotactic response in *Escherichia coli*. *Nature* **249**, 74-77 (1974).
- 123 Nam, S. W., Rooks, M. J., Kim, K. B. & Rossnagel, S. M. Ionic field effect transistors with sub-10 nm multiple nanopores. *Nano Letters* **9**, 2044-2048 (2009).
- 124 Holt, J. K. *et al.* Fast mass transport through sub-2-nanometer carbon nanotubes. *Science* **312**, 1034-1037 (2006).
- 125 Hummer, G., Rasaiah, J. C. & Noworyta, J. P. Water conduction through the hydrophobic channel of a carbon nanotube. *Nature* **414**, 188-190 (2001).

- 126 Corry, B. Designing carbon nanotube membranes for efficient water desalination. *Journal of Physical Chemistry B* **112**, 1427-1434 (2008).
- 127 Kalra, A., Garde, S. & Hummer, G. Osmotic water transport through carbon nanotube membranes. *Proceedings of the National Academy of Sciences of the United States of America* **100**, 10175-10180 (2003).
- 128 Kreuer, K. D., Paddison, S. J., Spohr, E. & Schuster, M. Transport in proton conductors for fuel-cell applications: Simulations, elementary reactions, and phenomenology. *Chemical Reviews* **104**, 4637-4678 (2004).
- 129 Saha, S. K. & Chakravorty, D. *Appl. Phys. Lett.* **89**, 043117 (2006).
- 130 Luzar, A. Activation barrier scaling for the spontaneous evaporation of confined water. *Journal of Physical Chemistry B* **108**, 19859-19866 (2004).
- 131 Cao, L. *et al.* Towards understanding the nanofluidic reverse electrodialysis system: Well matched charge selectivity and ionic composition. *Energy and Environmental Science* **4**, 2259-2266 (2011).
- 132 Guo, W. *et al.* Energy harvesting with single-ion-selective nanopores: A concentration-gradient-driven nanofluidic power source. *Advanced Functional Materials* **20**, 1339-1344 (2010).
- 133 Bard, A. J. & Faulkner, L. R. *Electrochemical Methods: Fundamentals and Applications* (1980).
- 134 Post, J. W. *et al.* Salinity-gradient power: Evaluation of pressure-retarded osmosis and reverse electrodialysis. *Journal of Membrane Science* **288**, 218-230 (2007).
- 135 Xu, J., Sigworth, F. J. & Lavan, D. A. Synthetic protocells to mimic and test cell function. *Advanced Materials* **22**, 120-127 (2010).

136 Moerison Jr, F. A. & Osterle, J. F. Electrokinetic energy conversion in ultrafine capillaries. *The Journal of Chemical Physics* **43**, 2111-2115 (1965).

TEENA JAMES

Born January 03, 1982 in Kerala, India

EDUCATION

Johns Hopkins University
PhD Candidate, Chemical & Biomolecular Engineering
Advisor: Dr. David Gracias
Baltimore, MD
(Jan 2009- Present)

New Jersey Institute of Technology (NJIT)
Master of Science (MS), Biomedical Engineering
GPA: 3.875/4.0
Thesis: Nano-scale dielectric sensors for monitoring aptamer-protein interactions
Advisor: Dr. Dentcho V. Ivanov, Director, Microelectronics Research Center, NJIT.
Newark, NJ
(Jan 2009)

University of Calicut (GEC Thrissur)
Bachelor of Technology (B-Tech), Chemical Engineering
First Class with Honors
Kerala, India
(June 2005)

PUBLICATIONS

Journal papers

1. James T., Mannoor M.S., Stone H. A., McAlpine M.C. and Gracias D. H., "Remote Control of a Bacterium using Plasmonic Nanoantenna" (In preparation)
2. Mannoor M.S., Z. Jiang, T. James, Y. L. Kong, K. A. Malatesta, W. O. Soboyejo, N. Verma, D. H. Gracias, M. C. McAlpine, "3D Printed Bionic Ears." *Nano Letters* (2013).
3. James T., Kalinin Y., Chen C. C., Randhawa J. S., Gaevski M., Gracias D. H., Voltage-gated ion transport through semiconducting conical nanopores formed by metal nanoparticle assisted plasma etching *Nano Letters* 2012 12 (7), 3437-3442 (2012)
4. James, T., Cho, J. H., Fernandes, R., Randhawa, J. S., Gracias, D. H. A one-step etching method to produce gold nanoparticle coated silicon microwells and microchannels. *Anal. Bioanal. Chem.* 398, 2949-2954 (2010).
5. Cho, J. H., James, T., Gracias, D. H. Curving nanostructures using extrinsic stress. *Adv. Mater.* 22, 2320-2324 (2010).
6. James, T., Mannoor, M. S., Ivanov, D. V., Beadling, L., Braunlin, W. Nanogap dielectric spectroscopy for aptamer-based protein detection. *Biophysical Journal* 98, 724-732 (2010).
7. James, T., Mannoor, M. S., Ivanov, D. V. BioMEMS - Advancing the frontiers of medicine. *Sensors* 8, 6077-6107 (2008).

Invited Talks

1. 10th Annual Conference on Foundations of NanoScience (FNANO12), Utah, April 2012
Self-Assembled Architectures and Devices
2. NanoTX'08 - International Nanotechnology Conference and Trade Expo, October, 2008, Dallas, Texas. Session: Electronics & Materials.

Conference Presentations

1. T. James, J. Cho, C. Yoon, D.H Gracias (2012) Origami Inspired Self-assembly of 3D Nanostructures, ACS 86th Colloid and Surface Science Symposium, Johns Hopkins University, Baltimore, Maryland, June 2012.
2. T. James, J. Cho, Y. Kalinin, C. Chan, J. Randhawa, D. H Gracias,(2012) 86th Colloid and Surface Science Symposium, Johns Hopkins University, Baltimore, Maryland, June 2012.
3. T. James, S. Y. Park ,D. H Gracias,(2012) Nanoscale Origami, Foundations of Nanoscience (FNANO 2012), Utah, April 2012.
4. T.James, M. Karakoy, C. C. Chan, D. H. Gracias,(2012) Bacterial Backpacking, Foundations of Nanoscience (FNANO 2012), Utah, April 2012.
5. T. James, Y.V Kalinin, C. Chan, J. S Randhawa, M. Gaevski, D. H Gracias (2012) Active control of ionic and molecular transport through semiconducting conical nanopores, 243rd ACS National Meeting San Diego, California, March 2012.
6. T. James, C. Yoon, D. H Gracias (2012), Nanoscale origami using surface forces, 243rd ACS National Meeting San Diego, California, March 2012.
7. T. James and D. H. Gracias (2011) Metal Assisted Plasma Etching (MAPE). Materials Research Society (MRS) Fall meeting, Boston, MA, Dec. 2011.
8. T. James J. H Cho and D. H. Gracias (2011) Enabling Lithographic Patterning on Curved Nanostructures by Self-Assembly. Materials Research Society (MRS) Fall meeting, Boston, MA, Dec.
9. Cho, J. H., T. James, D. H. Gracias (2010). Fabrication of 3D nanostructures with lithographically patterned surfaces by self-folding SPIE, Vol 7767, 776704 (2010).
10. T. James, S. Pandey, C-C Chan, H. Schwartz and D. H. Gracias(2010) Metal Assisted Plasma Etching of Silicon- A one step etching method for fabrication of microfluidic devices, membranes and sensors MRS Fall meeting, Boston, MA, Dec. 2010
11. J-H Cho, S-Y. Park, T. James, David H. Gracias (2010) Self folding and curving lithographically patterned structures MRS Fall meeting, Boston, MA, Dec. 2010
12. T. James, M. S. Mannoor, D. V Ivanov (2008).Active MOS Capacitive Sensor Array for Lab-On-a-Chip Applications” 35th annual conference of Federation of Analytical Chemistry & Spectroscopy Societies (FACSS)
13. T. James, M. S. Mannoor, D. V Ivanov, L. Beadling and B. Braunlin (2008) NEMS Capacitive Sensors for Highly Sensitive Label -Free Nucleic-acid Analysis (Nano-Networks)
14. T. James, M. S. Mannoor, D. V Ivanov, L. Beadling and B.Braunlin (2009) Label-free affinity based geno-sensors for point-of-care diagnostic applications SPIE symposium on MOEMS-MEMS, Sanjose, CA.

15. T. James, M. S. Mannoer, D.V Ivanov, L. Beadling and B.Braunlin (2008) Ultra Sensitive Debye Capacitive Sensors with Nono-scale Electrode spacing for Label-free Nucleic Acid Analysis ” 5th International Congress of Nano-Bio Clean Tech, San Francisco, CA
16. T. James, M. S. Mannoer, D.V Ivanov, L. Beadling and B.Braunlin (2008) “Debye Capacitive sensor for biomolecular detection” NSTI Nanotech, Boston, MA.
17. T. James, M. S. Mannoer, D.V Ivanov, L. Beadling and B.Braunlin (2008) Active Field Effect Capacitive Sensor Array for High-Throughput Biomolecular Screening.” Materials Research Society (MRS) Fall meeting, Boston, MA, Dec.
18. T. James, M. S. Mannoer, D. V Ivanov, L. Beadling and B.Braunlin (2008)Nano-scale Debye Capacitive Sensors for Highly Sensitive, Label-free, Nucleic Acid Analysis Materials Research Society (MRS) Fall meeting, Boston, MA, Dec.
19. T. James, M. S. Mannoer, D.V Ivanov, L. Beadling and B.Braunlin(2008)Tunable Affinity Ligands for the Separation of Proteins and Biomacromolecular Complexes Biophys. J.94.
20. T. James, M. S. Mannoer, D. V Ivanov, L. Beadling and B.Braunlin “Molecular Scale Dielectric Sensors for Highly Sensitive Biomolecular Detection” Biophysical Journal, Volume 96, Issue 3, Pages 51a-51a

Invention Disclosures and Patents

1. Vertical Nano-cavity Dielectric Sensors for Biomolecular Detection (NJIT), US Provisional Patent application pending.

Book Chapter

1. Teena James, Manu Sebastian Mannoer and Dentcho V. Ivanov "BioMEMS - Integrating Micro/Nano fabrication with Biomolecular Technologies” in Biomedical Engineering and Design Handbook, Volume 1: Volume I: Biomedical Engineering Fundamentals / Edition 2, Myer Kutz (Editor), McGraw-Hill

AWARDS & AFFILIATIONS

- MRS Best Poster Award 2011
- Raith Micrography Award 2011
- F11FF NSF Scholarship Award 2011
- Member, American Institute of Chemical Engineers (AIChE)
- Student member, IEEE, Engineering in Medicine and Biology Society and Women in Engineering.
- Member, Biomedical Engineering Society (BMES).
- Member, Society of Women Engineers.
- Member, Tau Beta Pi, national engineering honor society
- Provost Fellowship, New Jersey Institute of Technology (2006-2007)
- Scientific Advisory Boards: Lifeboat Foundation (2010-Present)

TEACHING EXPERIENCE

- APC II – Applied Physical Chemistry II Spring 2011,
- APC I – Applied Physical Chemistry I Fall 2010
- Undergraduate student mentees- C.C. Chen, Harrison Schwartz, John Coia, Aditya Murali, Mert Karakoy.

PROFESSIONAL EXPERIENCE

- Graduate Research Assistant, Microelectronics Research Center, NJIT
08/06-05/08
- Graduate Assistant, BioMEMS Summer Institute, Micro Fabrication Center, NJIT
05/08-08/08
- Research Intern, Rational Affinity Devices LLC, Newark, NJ
05/07-08/07